

# From Pixels to Polygons: A Survey of Deep Learning Approaches for Medical Image-to-Mesh Reconstruction

Fengming Lin<sup>1,2</sup>, Arezoo Zakeri<sup>1,3</sup>, Yidan Xue<sup>1,3</sup>, Michael MacRaid<sup>1,2</sup>, Haoran Dou<sup>1,2</sup>, Zherui Zhou<sup>1,2</sup>, Ziwei Zou<sup>1</sup>, Ali Sarrami-Foroushani<sup>1,3</sup>, Jinming Duan<sup>1,3</sup>, Alejandro F. Frangi<sup>1,2,3,4,5,6\* 1</sup>

<sup>1</sup>Centre for Computational Imaging and Modelling in Medicine (CIMIM), The Christabel Pankhurst Institute, The University of Manchester, Manchester, UK

<sup>2</sup>Department of Computer Science, School of Engineering, University of Manchester, Manchester, UK

<sup>3</sup>Division of Informatics, Imaging and Data Sciences, University of Manchester, Manchester, UK

<sup>4</sup>NIHR Manchester Biomedical Research Centre, Manchester Academic Health Sciences Centre, University of Manchester, Manchester, UK

<sup>5</sup>Department of Cardiovascular Sciences, KU Leuven, Leuven, Belgium

<sup>6</sup>Department of Electrical Engineering (ESAT), KU Leuven, Leuven, Belgium

## Abstract

Deep learning-based medical image-to-mesh reconstruction has rapidly evolved, enabling the transformation of medical imaging data into three-dimensional mesh models that are critical in computational medicine and in silico trials for advancing our understanding of disease mechanisms, and diagnostic and therapeutic techniques in modern medicine. This survey systematically categorizes existing approaches into four main categories: template models, statistical models, generative models, and implicit models. Each category is analysed in detail, examining their methodological foundations, strengths, limitations, and applicability to different anatomical structures and imaging modalities. We provide an extensive evaluation of these methods across various anatomical applications, from cardiac imaging to neurological studies, supported by quantitative comparisons using standard metrics. Additionally, we compile and analyze major public datasets available for medical mesh reconstruction tasks and discuss commonly used evaluation metrics and loss functions. The survey identifies current challenges in the field, including requirements for topological correctness, geometric accuracy, and multi-modality integration. Finally, we present promising future research directions in this domain. This systematic review aims to serve as a comprehensive reference for

searchers and practitioners in medical image analysis and computational medicine.

## 1 Introduction

### 1.1 Background

In the fields of computational medicine and in silico trials, image-to-mesh reconstruction is critical for advancing our understanding of disease mechanisms, and diagnostic and therapeutic techniques in modern medicine. For advancing diagnostic and therapeutic techniques. From anatomical visualization to computational simulations [Sarrami-Foroushani et al. \[2021\]](#), the ability to accurately reconstruct three-dimensional (3D) representations of organs and tissues has transformed modern medicine. A mesh ([Lorensen and Cline \[1987\]](#)) is a collection of vertices, edges, and faces that define the shape of a 3D object, commonly used to represent anatomical structures in computational modelling. With the advent of deep learning, traditional methods relying on manual segmentation are increasingly complemented or replaced by data-driven approaches. Deep learning ([Shen et al. \[2017\]](#)) has enabled the direct mapping of medical images to anatomical representations like meshes, bypassing intermediate steps and offering enhanced precision.

\*Corresponding author: [alejandro.frangi@manchester.ac.uk](mailto:alejandro.frangi@manchester.ac.uk)

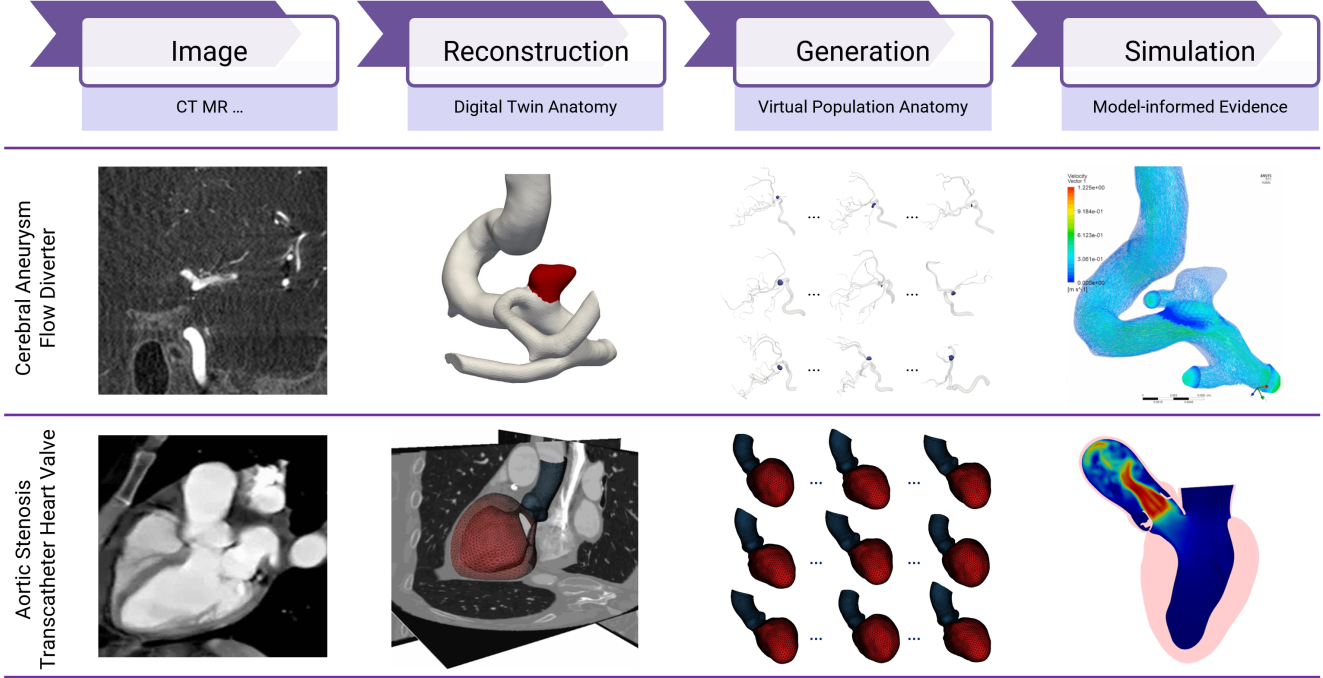


**Figure 1. Pipeline of in-silico trials, consisting of four key stages: image acquisition, reconstruction, generation, and simulation. Medical imaging modalities such as CT and MR scans provide anatomical data, which are then converted into digital twin anatomy in the reconstruction stage. The generation phase creates virtual population anatomy to account for variability, while the simulation stage performs computational analyses to derive model-informed evidence. Two examples are shown: (1) Cerebral aneurysm with flow diverter (Sarrami-Foroushani et al. [2021], MacRaid et al. [2024], Lin et al. [2023]), where vascular imaging is used to reconstruct the aneurysm, generate a virtual population, and simulate blood flow changes after device implantation; and (2) Aortic Stenosis with transcatheter heart valve (Pak et al. [2024], Ozturk et al. [2025]), where CT images are used to reconstruct the heart, generate a virtual cohort, and simulate hemodynamic effects of THV implantation.**

## 1.2 Motivation

The concept of in-silico trials, shown in Fig. 1, has emerged as a groundbreaking paradigm in computational medicine. In-silico trials use computer simulations to model the behaviour and response of biological systems under various conditions, providing a safe, ethical, and cost-effective alternative to traditional in-vivo or in-vitro experiments (Frangi et al. [2001], Walcott et al. [2016]). Central to this approach is the accurate generation of 3D anatomical meshes from medical images, which serve as the foundation for simulations such as hemodynamic studies, structural analysis, and virtual device testing.

Image-to-mesh reconstruction is pivotal for in-silico trials as it bridges the gap between imaging modalities and computational analysis. Through the reconstruction of patient-specific meshes, this technology helps overcome

challenges related to variability in anatomy, complex geometries, and the need for simulation-ready models. Consequently, advancements in image-to-mesh techniques play a key role in enabling personalized medicine and precision healthcare.

Traditional image-to-mesh reconstruction methods typically follow a two-step approach: segmentation first, followed by post-processing or registration. However, these segmentation-based methods heavily depend on the accuracy of segmentation, which is inherently limited by image resolution and segmentation performance. Errors in segmentation can significantly impact downstream tasks, such as simulations, leading to reduced accuracy and reliability. To overcome these limitations, the new generation of image-to-mesh reconstruction methods adopts an end-to-end approach, directly generating meshes from images without relying on an intermediate segmentation step.

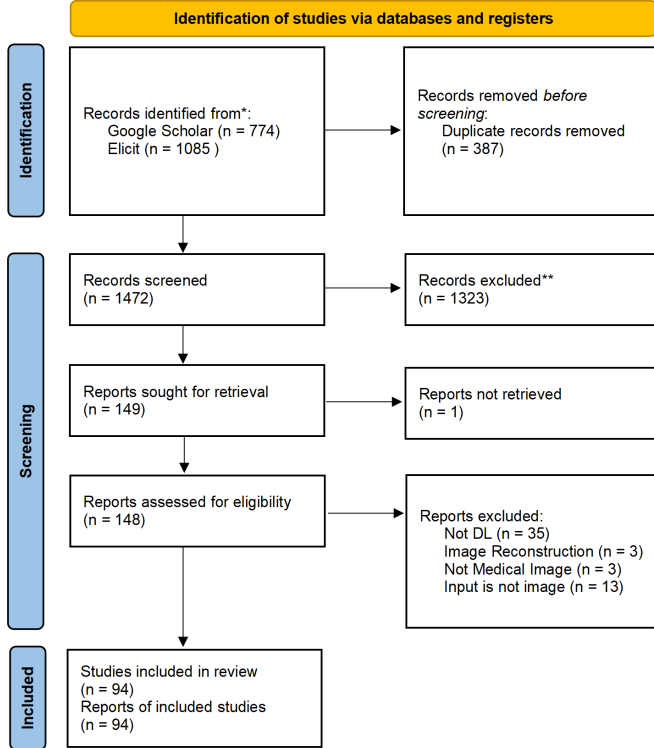


**Figure 2. PRISMA flowchart summarizing the systematic review process. (PRISMA registration number: CRD420250655291)**

### 1.3 Scope

This paper focuses on deep learning-based methods for end-to-end image-to-mesh reconstruction, offering a structured taxonomy and in-depth analysis of methodologies, loss functions, evaluation metrics, and their applications in different anatomies.

We categorize existing methods into four primary groups: template models, statistical shape models, generative models, and implicit models. These methodologies further branch into twelve subcategories, capturing variations in processing pipelines and feature representations (see Fig. 3). These approaches take various medical imaging modalities as input, including computed tomography (CT), magnetic resonance (MR), and ultrasound (US), to generate anatomical meshes tailored for advancing diagnostic and therapeutic techniques.

In addition to methodological classification, we systematically analyze loss functions and evaluation metrics from two perspectives. First, we group them based on their design principles into shape similarity, regularization, and function-driven constraints. Shape similarity measures include distance-based metrics and consistency checks, while

regularization encompasses smoothness, topological constraints, and curvature preservation. Function-driven evaluation further considers clinical and simulation-specific constraints. Second, we examine these metrics concerning their computational representations, such as vertex-based, voxel-based, normal vector-based, and implicit function-based formulations.

Furthermore, we conduct a meta-analysis, applying these evaluation metrics to different anatomical structures and comparing the performance of various methodologies. This comparative assessment provides insights into the effectiveness of different techniques across diverse anatomical regions.

Lastly, we discuss the strengths and limitations of each approach, offering guidance for selecting the most suitable methodology for specific medical applications. By identifying current challenges and opportunities, we aim to assist researchers in refining and advancing image-to-mesh reconstruction frameworks.

### 1.4 Contributions

This work makes the following contributions:

- We present a systematic review of end-to-end medical image-to-mesh reconstruction, offering a detailed analysis of its methodologies and performance. We establish a systematic taxonomy, categorizing these methods into four main types: statistical shape models, template models, generative models, and implicit models. Additionally, we further divide these four categories into twelve subcategories based on their processing pipelines and feature representations.
- A summary and classification of loss functions and evaluation metrics used in these methods, along with a meta-analysis of experimental results on different anatomies to assess the performance of different method categories.
- We systematically review and curate publicly available datasets in this field, covering multiple anatomical structures and imaging modalities. This dataset collection provides a structured resource for researchers working on image-to-mesh reconstruction and in-silico trial simulation.
- Identification of open challenges and future research directions, emphasizing the need for higher-fidelity training methods, topology constraints and multi-model fusion.

### 1.5 PRISMA Framework

The systematic review conducted in this paper adheres to the PRISMA (Preferred Reporting Items for Systematic Re-

views and Meta-Analyses) guidelines [Page et al. \[2021\]](#). A detailed flowchart summarizing the literature selection process is provided in Fig. 2, ensuring transparency and reproducibility in the research methodology.

## 2 Methods Taxonomy

Medical image-to-mesh reconstruction methods, shown in Fig. 3, can be broadly categorized into four primary types: statistical shape models, template models, generative models, and implicit models. Each of these methodologies addresses the challenge of reconstructing mesh structures from imaging data through distinct approaches, reflecting differences in theoretical foundations and application scopes. This classification not only highlights the diversity of techniques but also underscores the evolving landscape of mesh reconstruction driven by advancements in deep learning and computational geometry.

Template models represent a class of approaches that focus on transforming an initial template mesh to fit the anatomy shape derived from input medical images. These models rely heavily on iterative adjustment of vertex positions, allowing for gradual refinement that results in anatomically consistent meshes.

Statistical shape models offer a data-driven perspective, leveraging a large repository of anatomical meshes to construct probabilistic shape representations. By capturing the principal modes of variation within the dataset, these models enable accurate predictions of new mesh structures that conform to the general anatomical shape while preserving individual variations.

Generative models aim to synthesize mesh structures directly from input data without relying on pre-existing templates. By learning the underlying distribution of anatomical shapes, these models can generate complex surfaces, providing a flexible solution for mesh reconstruction tasks across various imaging modalities.

Implicit models diverge from the other categories by representing surfaces as continuous functions, allowing for smooth and high-resolution mesh extraction. These methods bypass the need for explicit mesh representations during training, instead learning implicit functions that define surface boundaries indirectly.

The output representations across these methodologies can take different forms, ranging from discrete point clouds to implicit functions and meshes. Ultimately, all these representations can be converted into meshes. Furthermore, assessing these models depends on similarity metrics that measure the degree of alignment between the reconstructed meshes and the ground truth in terms of point, voxel grid, latent feature, and implicit function. Regularization techniques are also frequently used to ensure smoothness, topology, and curvature in case of unrealistic deformations, con-

tributing to robustness and generalizability.

This taxonomy serves as a framework for understanding the broad spectrum of approaches in medical image-to-mesh reconstruction. By organizing methods according to their processing pipelines and feature representations, this taxonomy provides a structured overview that facilitates a deeper exploration of each technique in subsequent sections.

## 3 Template Model

A template model is a type of image-to-mesh reconstruction method that operates by deforming a template mesh. The core idea is to start with an initial template mesh and iteratively deform it to match the input medical image. This approach is particularly suitable for medical images with relatively simple topology, such as the heart or abdominal organs (not vessels), as it leverages prior anatomical knowledge to produce physically plausible meshes. Deformation models can be divided into two main categories: conditioned deformation models and registration models. A conditional deformation model extracts deformation information through a segmentation pipeline to guide the deformation of a template. In contrast, a registration model computes a deformation field to direct the template’s transformation. Although these categories differ in how the template deformation is achieved, their shared goal is to generate accurate structure meshes through learned deformations.

### 3.1 Conditioned Deformation Methods

As shown in Fig. 5, conditional deformation models employ graph convolution networks to iteratively deform the template mesh. Typically, a CNN extracts features from the input medical image, which are then passed to the GNN to guide the vertex-wise deformation of the template. Since GNNs are well-suited for handling non-Euclidean data such as meshes and point clouds, they are highly effective for template-based deformation tasks. The advantage of this method lies in its ability to preserve the topological structure of the original template while producing meshes that conform to the medical image.

[Kong et al. \[2021\]](#), [Kong and Shadden \[2021\]](#) introduced an additional free-form deformation (FFD) module in the GNN to enhance smoothness. Specifically, the method [Kong and Shadden \[2021\]](#) employs a deep learning model and template deformation technique to generate whole heart meshes matching input image data by predicting displacements of multi-resolution control point grids. The method first processes input images through an image encoding module then samples image features via a feature sampling module, uses a deep FFD module to predict control point displacements for template mesh deformation, and employs

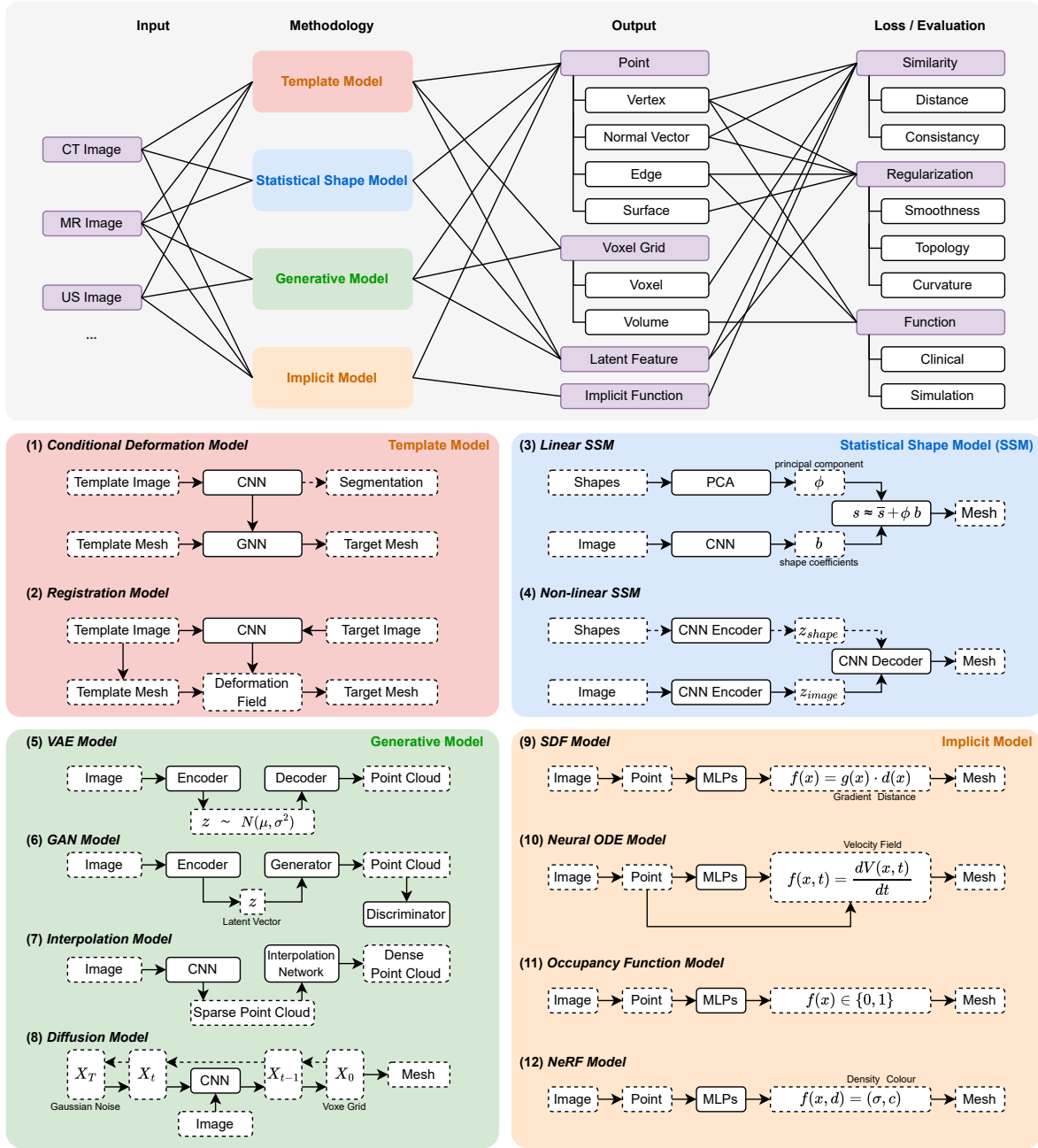
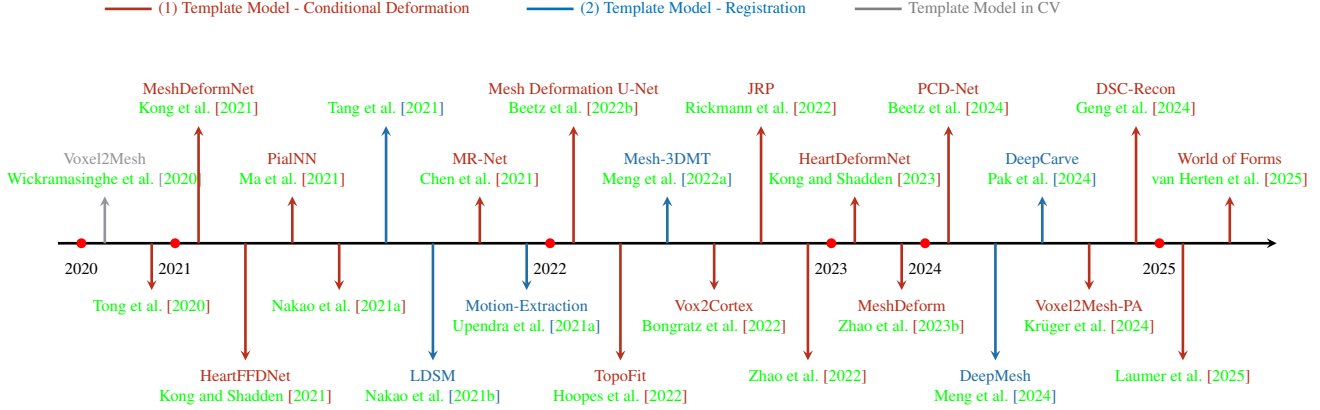
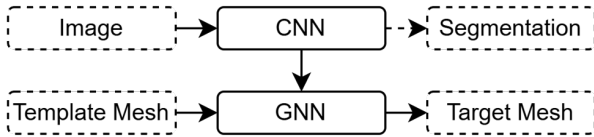


Figure 3. Survey structure, categorizing deep learning-based medical surface reconstruction into four paradigms: template models, statistical shape models (SSM), generative models, and implicit models. Dashed boxes represent variables, while solid boxes represent modules that process these variables using algorithms such as convolutional neural networks (CNN) and graph neural networks (GNN). Solid arrows indicate essential processes, whereas dashed arrows denote optional processes.





**Figure 4. Chronological overview of representative template models for medical image-to-mesh reconstruction.**



**Figure 5. Schematic of conditioned deformation methods. The framework consists of two pipelines: one leveraging a CNN for deformation feature extraction and the other employing a GNN for direct template mesh deformation. During feature propagation, the CNN pipeline transfers learned features from the image to the GNN pipeline. Dashed boxes represent variables, while solid boxes denote operations. Solid arrows indicate mandatory connections, and dashed arrows represent optional connections.**

a segmentation module for additional supervision. The method Kong et al. [2021] uses a graph convolutional neural network to directly predict whole heart surface meshes from volumetric CT and MR image data, reconstructing multiple anatomical structures by deforming a predefined mesh template, and can reconstruct whole heart dynamics from 4D imaging data.

Based on Kong et al. [2021] and Kong and Shadden [2021], Kong and Shadden [2023] used biharmonic coordinates to further improve the topological quality of the reconstructed mesh, enabling the reconstruction of simulation-suitable meshes. Specifically, the method uses deep learning techniques to construct simulation-suitable heart models from 3D patient image data (CT and MRI) by deforming a

whole heart template, generating anatomically and temporally consistent geometries.

Nakao et al. [2021a, 2022] trained an additional deformation map with the CNN, which directly acts on the template. This method proposes an Image-to-Graph Convolutional Network (IGCN+) framework that integrates an image generative network and graph convolutional network to reconstruct 3D organ shapes from a single two-dimensional (2D) projection image, which is particularly effective for low-contrast organs. The method first uses an image generative network to create displacement maps from 2D projection images, then employs a graph convolutional network to learn vertex features and generate the final 3D deformed mesh.

Same with the structure in Fig. 5, the input used by Chen et al. [2021] is not an image but a sparse and incomplete point cloud. Therefore, format transfer is performed both before and after feeding it into the CNN. Features are extracted from both the point cloud and the converted voxel, and these features are then combined. Specifically, this method presents MR-Net, a deep learning architecture for 3D shape reconstruction from sparse and incomplete point clouds. The method consists of a feature extraction module and a deformation module. The feature extraction module extracts features from input contours through point cloud feature extraction and 3D CNN, while the deformation module uses three GNN blocks to gradually deform a template mesh under the guidance of extracted features. The method innovatively designs a point-to-point mapping mechanism to address the challenge of feature mapping between unstructured data.

Hoopes et al. [2022] introduced TopoFit, a fast cortical reconstruction method that deforms a topologically correct template mesh to fit the target anatomy. To ensure local structural accuracy and maintain topological consistency

**Table 1. Template Models for Medical Image-to-Mesh Reconstruction**

Name	Method	Input	Output	Anatomy	Modality	Dataset
MeshDeformNet Kong et al. [2021]	Conditional Deformation	3D Image	Mesh	Heart	CT/MR	MMWHS, OrCaScore, SLAWT, LASC, Private Data
HeartDeformNet Kong and Shadden [2023]	Conditional Deformation	3D Image	Simulation-ready Mesh	Heart	CT/MR	MMWHS, OrCaScore, LASC
3DAngioNet Bransby et al. [2023]	Conditional Deformation	2D Image	Mesh	Coronary Arteries	X-ray Angiographic	Private Data (Barts Health NHS Trust)
Mesh-3DMT Meng et al. [2022a]	Registration	2D CMR images (SAX+LAX)	Dynamic Mesh	Heart	CMR	UK Biobank
DeepMesh Meng et al. [2024]	Registration	2D CMR Images (SAX, 2CH, 4CH)	Dynamic Mesh	Heart	CMR	UK Biobank
PCD-Net Beetz et al. [2024]	Conditional Deformation	Point cloud at ED/ES phase	Point Cloud at ES/ED	Heart (LV/RV)	CMR	UK Biobank
Vox2Cortex Bongratz et al. [2022]	Conditional Deformation	3D Image	Surface Mesh	Brain Cortex	MRI-T1	ADNI, OASIS-1, TRT
MeshDeform Zhao et al. [2023b]	Conditional Deformation	MRI-T1 w/T2w	Surface Mesh	Brain Cortex	MR	HCP
LDSM Nakao et al. [2021b]	Registration	4D Contours	Tumor position and deformation	Abdominal Tumor	CT	Private Data (25)
Mesh Deformation U-Net Beetz et al. [2022b]	Conditional Deformation	2D Image	Mesh	Heart (LV/RV)	MR	UK Biobank, Private Data (250)
HeartFFDNet Kong and Shadden [2021]	Conditional Deformation	3D Image	Surface Mesh	Heart	CT	MMWHS, orCalScore, SLAWT
TopoFit Hoopes et al. [2022]	Conditional Deformation	3D Image	Surface Mesh	Brain Cortex	MR	OASIS, IXI, MCIC, Buckner40
PialNN Ma et al. [2021]	Conditional Deformation	3D Image	Surface Mesh	Brain Cortex	MR	HCP (300)
JRP Rickmann et al. [2022]	Conditional Deformation	3D Image	Multi-class Surface Mesh	Brain Cortex	MR	OASIS-1
- Zhao et al. [2022]	Conditional Deformation	3D Image	Surface Mesh	Aortic Dissection	CTA	WAD (35)
- Tong et al. [2020]	Conditional Deformation	Single 2D Image	Surface mesh	Liver	CT	Private Data
- Nakao et al. [2021a]	Conditional Deformation	2D Projection Image	Surface Mesh	Abdominal Organs	CT	Private Data (474)
- Tang et al. [2021]	Registration	2D Image	3D Surface Mesh	Spine	US	Private Data (10)
Voxel2Mesh-PA Krüger et al. [2024]	Conditional Deformation	3D Image	Surface mesh	Pulmonary	CT	Private Data (58)
MR-Net Chen et al. [2021]	Conditional Deformation	2D Contour	Surface Mesh	Bi-ventricular heart	MR	UK Biobank
DSC-Recon Geng et al. [2024]	Conditional Deformation	3D Image	Dynamic Mesh	Liver, Lung	CT/X-ray	4D Preoperative CT (20 lung, 45 liver) + 13 Intraoperative CT/X-ray pairs
Motion-Extraction Upendra et al. [2021a]	Registration	4D Image	Dynamic Mesh	Right Ventricle	CMR	ACDC
- Laumer et al. [2025]	Conditional Deformation	2D Image	Surface Mesh	Heart (LV)	Echocardiographic	4D SSM (458), SPUM-ACS (458)
GHD-DVS Luo et al. [2024]	Registration	3D Image	Mesh	Heart (LV)	CT/MR	MMWHS, CCT48, ACDC, UK Biobank, MITEA

across different scales, the approach incorporates manifold distance loss and manifold regularization loss as additional constraints. This allows for the direct reconstruction of a topologically correct surface without requiring post-processing to fix topology errors. The model integrates image and graph convolutions with an efficient symmetric distance loss to learn deformation fields. It first extracts features from input images using a convolutional network, then progressively deforms the template mesh through multiple graph convolution blocks. Each block samples image features and predicts local deformations, ultimately producing an anatomically accurate mesh.

Ma et al. [2021] proposed PialNN, this model did not use GNN as is used in a typical template model in Fig. 5, but instead directly employed multilayer perception (MLP) layers in the PialNN model to fuse image features and point

features. Experiments demonstrated that the performance of GNN and MLP in brain pial surface reconstruction is similar in terms of accuracy, but MLP significantly reduces computational demand compared to GCN. Specifically, PialNN is a deep learning framework that deforms an initial white matter surface to a pial surface through a sequence of learned deformation blocks. Each block incorporates vertex features and local MR features using local convolutional operations to capture multi-scale information. The method employs three deformation blocks, each extracting point features and local MR features to predict vertex displacements for surface deformation, followed by Laplacian smoothing for optimization.

Rickmann et al. [2022] and Bongratz et al. [2022] improve the template to a multi-class template and calculated reconstruction loss separately for each class. Specifically,

Rickmann et al. [2022] propose CSR, a graph classification branch and a novel 3D reconstruction loss approach to enhance template-deformation algorithms, achieving joint reconstruction and atlas-based parcellation of cortical surfaces. The method first deforms template meshes using CSR networks, then achieves parcellation either through a graph classification network or class-based reconstruction loss, with end-to-end training. Bongratz et al. [2022] propose Vox2Cortex, this algorithm employs geometric deep neural networks, combining convolutional and graph convolutional networks, to directly reconstruct high-resolution 3D meshes of cortical surfaces from MR scans by deforming an initial template mesh. The method introduces a curvature-weighted Chamfer loss function for better accuracy in highly folded regions.

Similarly, Zhao et al. [2022] tackle mesh quality issues by incorporating a homogeneity-optimized stepwise mesh regression module, which refines the output mesh to suppress folding and uneven distribution problems. Their morphology-constrained stepwise deep mesh regression (MSMR) method segments the true lumen of aortic dissection by first generating an initial mesh based on centerlines, then estimating offsets using deep feature encoders and graph convolutional decoders, and finally deforming the mesh to the target surface through multiple regression steps. Both approaches leverage deep learning for template-based mesh deformation, with Vox2Cortex prioritizing cortical surface reconstruction and MSMR refining anatomical meshes to improve structural integrity. Their shared emphasis on regularization strategies, curvature-aware loss in Vox2Cortex and homogeneity optimization in MSMR, highlights the growing role of geometric deep learning in accurate, topology-preserving anatomical mesh reconstruction.

3D shape reconstruction from 2D projections using a template-based approach is performed by Tong et al. [2020] in the X-ray2Shape model. X-ray2Shape is a deep learning framework combining GNN and CNN that reconstructs a 3D liver mesh from a single 2D X-ray projection image. The method learns mesh deformation from a mean template using deep features computed from individual projection images. The method first extracts features from digitally reconstructed radiograph (DRR) images using CNN, then concatenates these features with 3D vertex coordinates and feeds them into a GNN network for mesh deformation, optimizing the reconstruction using MSE loss and Laplacian loss. Similarly to the method in Tong et al. [2020], Wang et al. [2020b] proposed DeepOrganNet, which uses 2D projection images as input and incorporates the FFD method. Specifically, DeepOrganNet employs a deep neural network to reconstruct 3D/4D lung models from single-view 2D medical images, learning smooth deformation fields from multiple templates and extracting latent descriptors to gen-

erate high-fidelity lung model meshes. The method first encodes the input image using MobileNets Howard et al. [2017] to obtain feature descriptors, then reconstructs left and right lungs through two independent branches, each learning optimal template selection and smooth deformation based on FFD, finally combining them through a spatial arrangement module to generate the final two-lung model.

Bransby et al. [2023] added an additional CNN branch to the typical structure for template-based models in Fig. 5 to extract the centerline, which is then used to reconstruct the template surface mesh of coronary vessels. Bransby et al. [2023] propose 3DAngioNet, this method combines an EfficientB3-UNet Tan and Le [2019] segmentation network with graph convolutional networks for deformation to reconstruct 3D coronary vessels from bi-plane angiography images, capable of handling bifurcated vessels.

Based on Fig. 5, Zhao et al. [2023b] sampled the output of the feature by the encoder part of the CNN into the GNN for reconstruction. On the contrary, Krüger et al. [2024] sampled the features from the decoder part of the CNN into the GCN. Moreover, the output of the CNN does not include a segmentation task as a constraint in Krüger et al. [2024]. Specifically, MeshDeform Zhao et al. [2023b] is an end-to-end deep learning network for reconstructing subcortical structure surfaces from brain MR images. The method employs a 3D U-Net encoder to extract multi-scale features and combines them with a graph convolutional network to predict subcortical surfaces by deforming spherical mesh templates. The network contains three mesh deformation blocks, each utilizing graph convolutions to predict vertex displacements. This approach can efficiently and accurately reconstruct subcortical surfaces while preserving spherical topology. Meanwhile, Krüger et al. [2024] present a deep learning approach for automatic pulmonary artery surface mesh generation from CT images. Based on the Voxel2Mesh proposed by Wickramasinghe et al. [2020] algorithm, it combines voxel encoder-decoder and mesh decoder to deform a prototype mesh (sphere) into the target mesh. The key innovations include a centerline coverage loss to facilitate branching structure formation and vertex classification for defining inlets and outlets. The method can automatically generate high-quality meshes suitable for hemodynamic simulation while significantly reducing manual interaction time.

Geng et al. [2024] enriched the framework structure of Fig. 5 by reconstructing 4D dynamic meshes from different modalities. The method is divided into three steps. In the first step, CT images are segmented to obtain meshes at two time points, and interpolation is performed to estimate meshes at intermediate time points, which are used as templates. In the second step, enhanced projection images are obtained from the CT volume as input and, together with the mesh templates, fed into the framework in Fig. 5 to obtain



the reconstructed meshes. In the third step, during inference, a domain adaptation network trained for X-ray to CT style conversion is applied, and the converted images are used as input for reconstruction.

Instead of directly inputting a template mesh into the GNN, [Beetz et al. \[2022b,a, 2024\]](#) first obtained a point cloud contour through image segmentation. They then combined the contour with the template mesh to create a misaligned mesh, which was subsequently aligned using the GNN to generate a high-quality mesh.

GNN-based registration methods like [Hansen and Heinrich \[2021\]](#) are an alternative variant of template methods designed to address the issue of misaligned meshes during reconstruction. In this approach, a rough, misaligned mesh is first generated before being fed into the GNN. The GNN then learns to refine and correct the misalignment, gradually deforming the input mesh to align it with the target shape. By introducing this initial misalignment, the network is encouraged to develop a stronger understanding of local and global surface features, enhancing its ability to handle complex deformations. Alignment-based methods are particularly effective in scenarios where the input data is incomplete or noisy, as the GNN can iteratively improve mesh quality and ensure accurate surface reconstruction. This process ultimately reduces errors in the final mesh, yielding smoother and more topologically consistent results.

[Beetz et al. \[2022b\]](#) propose a Mesh Deformation U-Net deep learning method that combines spectral graph convolutions and mesh sampling operations to reconstruct 3D cardiac surface meshes directly on mesh data through multi-scale feature learning, using a template mesh as a prior to correct misalignment in multi-view MR slices. The method follows a 4-step pipeline where each MR slice is first segmented using CNNs, the segmentation contours are then placed in 3D space as point clouds, a template mesh is approximately fitted to the sparse contours, and finally the Mesh Deformation U-Net corrects any slice misalignment to output the reconstructed 3D cardiac shape. Based on [Beetz et al. \[2022b\]](#), [Beetz et al. \[2022a\]](#) applied GNN not for correcting misaligned meshes but to model deformations between different phases of the cardiac cycle. The method utilizes two separate networks to predict cardiac contraction and relaxation: one network predicts the end-systolic (ES) shape from end-diastolic (ED) input, while the other predicts the ED shape from ES input. Both networks leverage spectral graph convolutions for feature extraction and employ a multi-scale encoder-decoder architecture to process mesh data, enabling accurate and efficient reconstruction of cardiac dynamics.

[Beetz et al. \[2024\]](#) builds upon their previous work [Beetz et al. \[2022b,a\]](#), enabling the transformation between end-diastole (ED) and end-systole (ES) after reconstruction. Additionally, the method can perform tasks such as disease

classification based on latent features. This point cloud deformation network (PCD-Net) is a deep learning approach for modelling 3D cardiac deformation during contraction and relaxation. The method employs an encoder-decoder architecture that enables efficient multi-scale feature learning directly on multi-class 3D point cloud representations of cardiac anatomy. The network takes a point cloud representation of the heart at one phase (end-systolic or end-diastolic) as input and predicts the shape at the other phase.

[van Herten et al. \[2025\]](#) does not extract deformation features from a CNN-based segmentation branch. Instead, it directly samples image intensities along rays cast from a central point to each vertex of a template mesh. These 1D ray signals are then encoded using a 1D CNN or a masked autoencoder to obtain per-vertex features, which are subsequently processed by a GNN to predict mesh deformations. By leveraging geometric priors such as spherical or tubular templates, the method reformulates mesh prediction as a radial regression task along fixed ray directions, enabling topologically consistent surface meshing with strong performance even in low-data regimes.

[Laumer et al. \[2025\]](#) also adopt a template-based deformation approach; however, unlike typical methods, the template mesh is not directly used as an input during forward propagation. Instead, the template (mean mesh from a statistical shape model) is utilized to construct the structure of the GNN decoder by generating multi-resolution mesh representations and computing the corresponding upsampling and adjacency matrices. This design fixes the decoder’s topology and enables the network to progressively decode a full-resolution left ventricular mesh from CNN-extracted features.

### 3.2 Template-based Registration Methods

Registration-based methods directly learn the mapping from medical images to deformation fields. Typically, a CNN extracts features from two different medical images, predicting a deformation field that deforms the initial template into the target mesh. The key to this method is the accuracy and smoothness of the deformation field, which can capture both local and global deformation information. This makes it particularly suitable for tasks involving multi-time point data or registration-based mesh generation. Deformation Field methods are flexible and efficient, making them ideal for large-scale medical image processing and deformation tasks.

[Meng et al. \[2022b\]](#) proposed MulViMotion, a shape-aware 3D myocardial motion tracking framework that estimates 3D heart motion from multi-view 2D cine CMR. The method integrates SAX and LAX views using a hybrid 2D/3D deep learning network. FeatureNet extracts motion and shape features, while MotionNet predicts dense 3D mo-

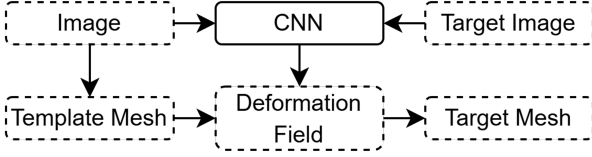


**Figure 6. Schematic of template-based registration methods.** The process begins by generating a template mesh from the input image using segmentation or registration techniques. The image and template image are then passed into a CNN to compute the deformation field, which is subsequently applied to the template mesh to generate the target mesh.

tion fields. A shape regularization module enforces consistency between predicted 3D myocardial edge maps and ground-truth 2D contours. Trained in a weakly supervised manner.

Based on Fig. 6, Meng et al. [2022a] used a differentiable mesh-to-image rasterizer to directly supervise the mesh with voxel data. This method uses a deep learning model and differentiable mesh-to-image rasterizer to estimate 3D heart mesh motion from 2D short- and long-axis cardiac MR images, enabling quantitative assessment of cardiac function by tracking the motion of each vertex in the 3D mesh. In a subsequent study, Meng et al. [2024] used a deep learning framework with a differentiable mesh-to-image rasterizer to reconstruct 3D heart meshes and estimate their motion from 2D cardiac MR images, leveraging 2D shape information from multiple views for 3D reconstruction and motion estimation. Notably, this paper performs bi-directional representation transformations between discrete and continuous domains: converting from continuous mesh representations to discrete voxel-based probability maps through differentiable rasterization, and sampling from discrete voxel-based motion fields to obtain continuous vertex-wise displacements via a grid sampling mechanism.

Pak et al. [2024] employs a registration-based strategy, DeepCarve, where a 3D CNN is used to predict a space-deforming field that is applied to a structured template volumetric mesh. The deformation field is sampled via trilinear interpolation to generate displacement vectors for each template point, enabling smooth and accurate transformation. To achieve label-efficient training, the model relies only on minimal surface mesh labels and jointly optimizes for spatial accuracy and volumetric mesh quality using a combination of isotropic and anisotropic energy terms. The resulting patient-specific heart meshes—including the ventricles,

aorta, and valve leaflets—achieve high spatial fidelity and element quality. It can be directly used for downstream finite element biomechanical simulations.

Aligned with the structure in Fig. 6, Upendra et al. [2021a] used a CNN to learn the deformation field between multi-phase images, which is then applied to deform the mesh. This is a deep learning-based deformable registration framework for extracting right ventricle motion from 4D cardiac cine MRI. It first uses CondenseUNet Hasan and Linte [2020] for segmentation, then employs VoxelMorph Balakrishnan et al. [2019] for image registration, and finally generates geometric models for all cardiac cycle frames by propagating the end-diastole isosurface mesh.

Tang et al. [2021] used a traditional registration method Chui and Rangarajan [2003] to learn the deformation field between local images (ultrasound, US) and global images (CT). The learned series of deformation fields (DF) is then applied to mesh deformation. This is a CNN-based method for reconstructing 3D spine surfaces from untracked free-hand ultrasound images. The method combines a U-net deep learning network for spine surface detection with registration-based scan path estimation to achieve reconstruction from 2D ultrasound images to 3D surfaces. The paper converts detected surface points to volumetric images, then applies Gaussian filtering and thresholding to generate the final surface reconstruction.

## 4 Statistical Shape Model

Statistical shape models (SSMs) Cootes et al. [1995] are widely used in medical image analysis and computer vision to describe and analyze the variability of anatomical structures. By representing shapes in a low-dimensional space, SSMs enable accurate shape reconstruction and efficient analysis. Traditional SSMs rely on techniques such as principal component analysis (PCA) or singular value decomposition (SVD) to extract the primary modes of variation. In contrast, deep learning-based SSMs harness neural networks to model more complex, non-linear shape deformations directly from images or point clouds.

Traditional SSMs Heimann and Meinzer [2009] encompass various approaches, including active shape models (ASM), point distribution models (PDM), point set models (PSM), and template models. Among these, PDM is widely applied in medical image-to-mesh reconstruction tasks Ruiz et al. [2018], Khalafvand et al. [2018].

PDM Cootes et al. [1995] is a classical method for statistical shape modelling that represents a shape using a set of landmarks. By applying statistical techniques such as PCA, PDM analyzes the distribution and variability of these landmarks across different samples. The core concept of PDM is to model and compress the primary modes of shape variation, allowing complex shapes to be represented by a small

number of parameters. This not only simplifies shape generation and matching but also facilitates efficient shape analysis and reconstruction.

Although traditional SSMs are effective in capturing shape variability, they are inherently limited to modelling linear shape variations. This constraint makes it challenging to accurately represent highly complex or non-linear deformations that are often encountered in real-world anatomical structures. To overcome these limitations, deep learning-based SSMs have emerged as a powerful alternative. By leveraging neural networks, these methods can model intricate, non-linear shape variations directly from image data, significantly enhancing the flexibility and accuracy of shape reconstruction.

#### 4.1 Deep Learning-based Linear SSM

Deep learning-based linear SSMs extend the traditional approach by automating the prediction of shape coefficients from input images with a deep learning encoder. As shown in Fig. 8, shape data undergoes PCA or SVD decomposition, resulting in the mean shape  $\bar{s}$  and the principal component matrix  $\phi$ . A CNN predicts the shape coefficients  $b$  from an image. The final shape  $s$  is reconstructed by:

$$s \approx \bar{s} + \phi b.$$

This method automates the process of mapping from image to shape but is constrained by the linear nature of PCA.

Attar et al. [2019a], Xia et al. [2022], and Romaszko et al. [2021] all integrated deep learning with statistical shape modelling techniques to achieve 3D cardiac shape reconstruction. Attar et al. [2019a] utilized a deep neural network combining statistical shape modelling and convolutional neural networks, incorporating both cardiovascular magnetic resonance images and patient metadata as input for 3D cardiac shape prediction. Building upon this, Xia et al. [2022] proposed MCSI-Net. Except for input multi-view images, this method also incorporates metadata, which aids in predicting shape bias. It integrates their deep learning encoder with an SSM to reconstruct the four heart chambers from cardiac MR images. Likewise, Romaszko et al. [2021] employ a deep learning pipeline that integrates image segmentation and PCA to generate a low-dimensional representation for reconstructing the 3D left ventricular geometry from cardiac MR images.

#### 4.2 Deep Learning-based Non-linear SSM

Deep learning-based non-linear SSM bypasses PCA by using neural networks to directly encode shapes into a non-linear latent space. As illustrated in Fig. 9, shape and image data are processed by two separate CNN encoders, producing shape encoding  $z_{shape}$  and image encoding  $z_{image}$ .

These encodings are combined and decoded by a CNN decoder to reconstruct the final shape  $s$ . This method captures more complex, non-linear deformations and provides greater flexibility in modelling anatomical variability.

Bhalodia et al. [2024] proposed DeepSSM, a deep learning framework that directly maps 3D images to low-dimensional shape descriptors, bypassing traditional manual preprocessing, and employs model-based data augmentation to address limited training data in shape modelling applications.

Aziz et al. [2023] presented Progressive DeepSSM, a training methodology for image-to-shape deep learning models. It employs a multi-scale progressive learning strategy that first learns coarse shape features and gradually progresses to more detailed features. The method incorporates segmentation-guided multi-task learning and deep supervision loss to ensure learning at each scale. The paper adopted a correspondence-based SSM approach by predicting correspondence points at different densities (starting from 256 points, progressively increasing to 512 and 1024 points) to represent shapes.

The primary difference between linear and non-linear deep learning-based SSMs lies in their capacity to model shape variations. Linear models rely on PCA, limiting them to linear deformations, while non-linear models use neural networks to capture complex, non-linear shape deformations. Non-linear SSMs are more expressive and adaptable, making them suitable for advanced medical image analysis tasks that require highly flexible shape modelling.

#### 4.3 Hybrid SSM

Some methods utilize deep learning in the reconstruction subprocess but do not directly apply it to the SSM itself. Instead, deep learning is employed to enhance other stages, such as segmentation, registration, or classification, which subsequently provides input to the SSM, rather than predicting the shape coefficients directly.

For example, Banerjee et al. [2022] proposed a method for 3D whole-heart mesh reconstruction from limited 2D cardiac MR slices using an SSM. In their approach, deep learning is used to extract heart contours from the 2D slices. The SSM is then optimally fitted to these sparse heart contours in 3D space, generating an initial mesh representation. This initial mesh is further deformed to minimize the distance between the mesh and the heart contours, resulting in the final reconstructed shape.

Yuan et al. [2023] used decoupled motion and shape models for 4D myocardium reconstruction, including a neural motion model for registration and an end-diastolic shape model for predicting sign distance function, pre-training the shape model with ED-space representation to guide motion model training, addressing data scarcity issues.

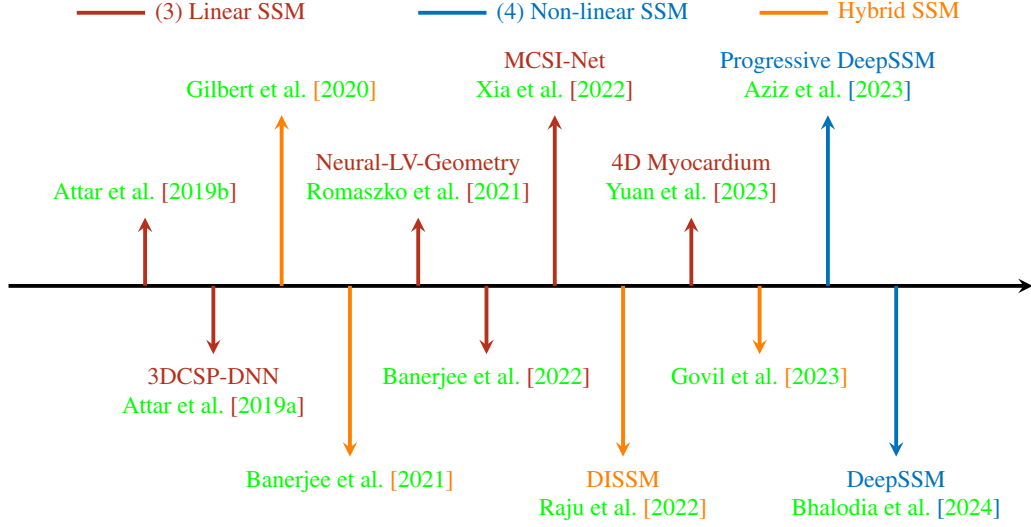


**Figure 7. Chronological overview of representative deep learning-based statistical shape models for medical image-to-mesh reconstruction.**

**Table 2. Statistical Shape Models for Medical Image-to-Mesh Reconstruction**

Name	Method	Input	Output	Anatomy	Modality	Dataset
3DCSP-DNN Attar et al. [2019a]	Linear SSM	Multi-view image, metadata	Mesh	Heart	CMR	UK Biobank
MCSI-Net Xia et al. [2022]	Linear SSM	Multi-view image, metadata	Mesh	Heart	CMR	UK Biobank
DeepSSM Bhalodia et al. [2024]	Non-linear SSM	3D Image	Point Cloud	Craniosynostosis, LA, Femur,	CT, MR	Metopic (120 CT), LA (206 MRI), Femur (49 CT)
4D Myocardium Yuan et al. [2023]	Hybrid SSM	Sparse point cloud of CMR slices	Dynamic Mesh	Heart Myocardium	CMR	Private data (55), ACDC (100)
Neural-LV-Geometry Romaszko et al. [2021]	Linear SSM	2D cine images (6 SA + 3 LA)	Dynamic Mesh	Heart LV	CMR	Private dataset (64 HV + 118 MI patients)
Banerjee et al. [2022]	Hybrid SSM	2D CMR Slices	Whole-Heart Mesh	Heart (4 Chamber)	CMR	UK Biobank (30) + Private CT (134)
Progressive DeepSSM Aziz et al. [2023]	Non-linear SSM	3D Image	Mesh	Femur, Left Atrium	CT, MR	Femur (59), Left Atrium (206)
WR-SSM Ruiz et al. [2018]	Linear SSM	2D photo / 3D point clouds	Mesh	Breast	Photo/Point Cloud	310 Point Clouds, 510 Photos
Gilbert et al. [2020]	Hybrid SSM	Cardiac MR	Surface/Volume Mesh	Heart (4 Chamber)	MR	MESA, UK Biobank
Govil et al. [2023]	Hybrid SSM	3D Image	Mesh	Heart (LV, RV)	CMR	Private Data (111)
Banerjee et al. [2021]	Hybrid SSM	2D Image	Mesh	Heart (LV)	CMR, ECGI	Private Data (20)
DISSM Raju et al. [2022]	Hybrid SSM	3D Image	SDF	Liver	CT	MSDLiver

Govil et al. [2023] used deep learning techniques for automated view classification, slice selection, phase selection, anatomical landmark location, and myocardial image segmentation to generate 3D biventricular cardiac shape models consistent with clinical workflows. In this method, the SSM comprised of three integrated components: template modelling using a biventricular subdivision surface mesh, hybrid registration (affine transformation + diffeomorphic non-rigid registration + landmark registration) for shape fitting, and statistical analysis through PCA-based shape atlas

construction and Z-score evaluation, with the first 20 PCA modes explaining  $\sim 87\%$  of shape variations.

Gilbert et al. [2020] reviewed methods of combining statistical cardiac atlases with deep learning in three main approaches: direct use of shape parameters for machine learning, incorporation of shape priors into deep networks, and direct prediction of statistical shape parameters from images. The methods mentioned in this review are to build statistical atlases of cardiac anatomy and combine them with deep learning networks in three ways: direct use of shape



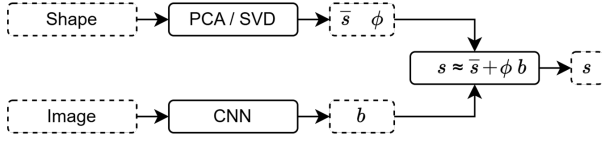


**Figure 8. Schematic of Deep Learning-based Linear SSM. Dotted boxes represent variables. Solid boxes represent functions.**

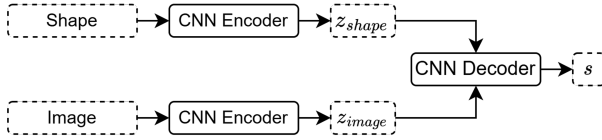


**Figure 9. Schematic of Deep Learning-based Non-linear SSM.**

parameters, adding shape constraints, or direct prediction of shape parameters.

Banerjee et al. [2021] used an SSM in the correction of misalignment during the reconstruction of the heart contour. This method corrects the misalignment of the cut through a three-step approach based on intensity, contours, and statistical shape models and finally generates 3D biventricular surface and volumetric meshes from the aligned contours. This method highlights the integration of deep learning in other steps for reconstruction, leveraging segmentation or reconstruction to refine SSM inputs, rather than directly incorporating deep learning into the core SSM modelling process.

Combined with sign distance function representation, Xu and Elhabian [2023] introduced Image2SSM, a deep learning-based statistical shape modelling approach that learns shape representations directly from medical image-segmentation pairs using radial basis functions (RBF). The method adaptively captures surface details and generates compact yet comprehensive shape representations without requiring the manual segmentation and correspondence optimization steps from traditional SSM workflows. The method first uses 3D medical images and their corresponding segmentations as training data, learning control points and their surface normals through a deep neural network. It then employs RBF interpolation to construct a continuous surface representation, while optimizing the network through multiple loss functions (surface loss, normal loss, correspondence loss, and sampling loss). Finally, it can directly predict PDMs from unsegmented images.

## 5 Model Generative

Generative models employ deep learning techniques to directly generate new shapes from data, particularly useful for synthesizing complex and diverse shapes. These methods are well-suited for unsupervised or semi-supervised learning, especially when data is scarce or shapes are intricate.

### 5.1 VAE-based Generative Models

Variational-based models have emerged as a powerful framework in generative modelling. Unlike deterministic approaches that directly map inputs to outputs, these models capture the underlying probability distributions of the data. By introducing a probabilistic perspective, variational-based models learn to parameterize distributions, typically using parameters like mean ( $\mu$ ) and variance ( $\sigma$ ), rather than predicting fixed values. This probabilistic nature allows them to model uncertainty and generate diverse outputs by sampling from the learned distributions. The optimization of these models often involves minimizing the Kullback-Leibler divergence between the learned and target distributions, along with task-specific reconstruction losses. This approach has proven particularly effective for complex generative tasks where capturing the full range of possible outputs is essential.

Gaggion et al. [2024] developed a novel deep learning architecture called HybridVNet, combining convolutional neural networks and graph convolutions, using a multi-view approach to process cardiac MR images and directly extract 3D meshes from medical images.

Hu et al. [2022] proposed a variational-based transformer framework for shape reconstruction (SRT) that reconstructs 3D point cloud representations from a single 2D brain MR image. The model adopts an encoder-decoder architecture, where the encoder uses a Multi-headed Attention Module (MAM) to encode the input image into a feature vector that follows a normal distribution, and the decoder employs a unique “up-down-up” generation system to reconstruct point clouds with 2048 points. The main innovation lies in completely avoiding CNNs and GANs, relying solely on transformer architecture and fully-connected networks, which ensures reconstruction accuracy and addresses issues like training instability and poor real-time performance that exist in GAN-based methods.

Cerrolaza et al. [2018] presented a novel approach for 3D fetal skull reconstruction from 2D ultrasound scans. It takes multiple standard 2D ultrasound planes (axial, sagittal, and coronal views) as input and produces a 3D reconstruction of the fetal skull as output. The process involves two proposed deep conditional generative networks: REC-CVAE, which uses a conditional variational autoencoder framework, and



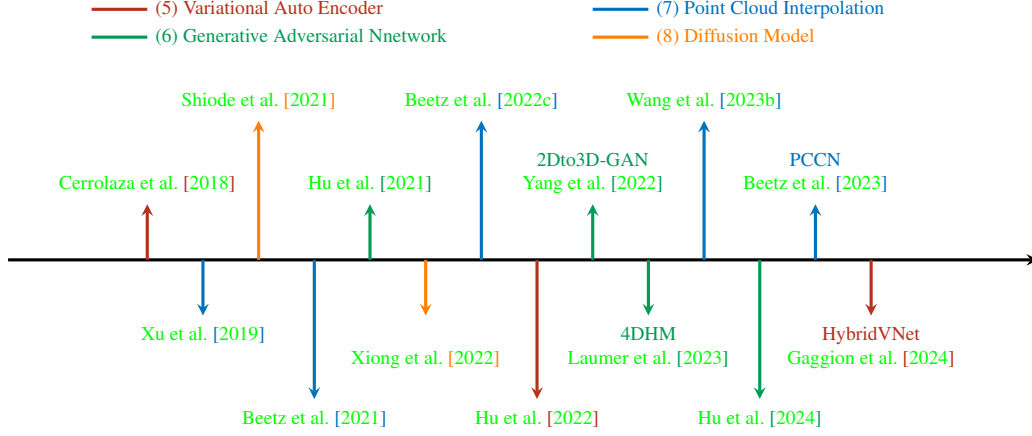


**Figure 10. Chronological overview of representative deep learning-based generative models for medical image-to-mesh reconstruction.**

**Table 3. Generative Models for Medical Image-to-Mesh Reconstruction.**

Name	Method	Input	Output	Anatomy	Modality	Dataset
HybridVNet Gaggion et al. [2024]	VAE	Multi-view image	Volume Mesh	Heart	CMR	UK Biobank
4DHM Laumer et al. [2023]	GAN	2D videos	Dynamic Surface Mesh	Heart	US ECGI	EchoNet-Dynamic
Hu et al. [2021]	GAN	2D Image	Point Cloud	Brain	MR	Private Data (317 AD and 723 Healthy)
Hu et al. [2024]	GAN	Incomplete 2D Image	Point Cloud	Brain	MR	Private Data (317 AD and 723 Healthy)
SRT Hu et al. [2022]	VAE	2D Image	Point Cloud	Brain	MR	Private Data (317 AD and 723 Healthy)
REC-CVAE Cerrolaza et al. [2018]	VAE	2D Image	Surface Mesh	Brain Skull	US	Private Data (72)
Xu et al. [2019]	Point Interpolation	2D Image	Surface mesh	Heart	MR	Cardiac SSM (1093)
GCN-Shape Wang et al. [2023b]	Point Interpolation	Partial mesh	Complete Mesh	Liver, Stomach	CT	Private Data (124 pancreatic tumor)
Beetz et al. [2021]	Point Interpolation	2D Contours	Surface Mesh	Heart (LV, RV)	MR	UK Biobank, Cardiac SSM
Beetz et al. [2022c]	Point Interpolation	3D Image	Surface Mesh	Heart (LV)	CMR	UK Biobank
PCCN Beetz et al. [2023]	Point Interpolation	3D Image	Surface Mesh	Heart (LV, RV)	CMR	Cardiac SSM, UK Biobank
Wang et al. [2023b]	Point Interpolation	2D Image	Surface Mesh	Spine	CT	Private Data (1012)
2Dto3D-GAN Yang et al. [2022]	GAN	3D Image	Surface Mesh	Liver	CT	Private Data (124)
Xiong et al. [2022]	GAN	3D Image	Surface Mesh	Skull Midface	CT	Private Data (518)
Shiode et al. [2021]	GAN	2D Image	Surface Mesh	Distal Forearm Bone	X-ray	Private Data (33)
Wodzinski et al. [2024]	Diffusion	Defective Mask	Reconstructed Mask	Skull	CT	SkullFix, SkullBreak, MUG500+
DMCVR He et al. [2023]	Diffusion	Sparse 2D Images	Dense 2D Images then Mesh	Heart	MR	UK Biobank
DISPR Waibel et al. [2023]	Diffusion	Single 2D Image	3D Voxel Grid then Mesh	Cell	Microscopy	SHAPR

HiREC-CVAE, which implements a hierarchical structure based on the clinical relevance of each view. The main innovation lies in its hierarchical approach that can operate effectively even with missing views.

Both Gaggion et al. [2024] and Cerrolaza et al. [2018] addressed multi-input VAE problems but employed different strategies: the former adopted a parallel approach, di-

rectly combining all  $\mu$  and  $\sigma$  generated from separate inputs to produce the latent variable  $z$ ; the latter used a cascading approach, progressively connecting two sets of  $\mu$  and  $\sigma$  to generate  $z$ , then deriving new  $\mu$  and  $\sigma$  from  $z$  to connect with the next input’s  $\mu$  and  $\sigma$ , thereby constructing a hierarchical information structure step by step.

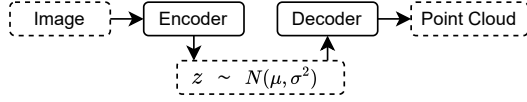


**Figure 11. Schematic representation of a variational autoencoder (VAE)-based model for mesh generation.** The input image is processed by the encoder to compute the mean and variance, which are used to sample a latent vector  $z \sim \mathcal{N}(\mu, \sigma^2)$ . The latent vector is then passed through the decoder to generate a point cloud, which is subsequently converted into a mesh.

## 5.2 GAN-based Generative Models

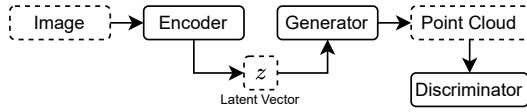


**Figure 12. Schematic representation of a generative adversarial network (GAN)-based model for mesh generation.** The input image is processed by the encoder to produce a latent vector. The latent vector is then passed to the generator, which outputs a point cloud. The generated point cloud is subsequently evaluated by a discriminator and converted into a mesh.

Laumer et al. [2023] developed an automated framework using a self-supervised learning approach to infer personalized 3D+time heart meshes from 2D echocardiography videos, generating 4D heart meshes closely corresponding to input videos without requiring paired data.

Instead of using CNN to get an incomplete point contour in Fig. 13, Hu et al. [2024, 2021] used a GAN predictor to generate initial incomplete point clouds, then used a hierarchical encoder-decoder architecture and attention mechanisms as a completion network to refine and reconstruct the point clouds. It specifically designs a branching GNN generator and attention gate blocks to improve reconstruction quality.

Hu et al. [2021] proposed a GAN-based 3D brain shape reconstruction model that takes a single 2D brain MR image as input and outputs a 3D point cloud representation consisting of 2048 points. The main innovation lies in proposing a tree-structured graph convolutional generative network,

which encodes the 2D image into a latent vector through an encoder, and then utilizes alternating branching block and graph convolution block to construct a tree-structured feature transmission mechanism, achieving the generation from a single vector to complex 3D point clouds. This method was the first to apply point cloud generation to brain shape reconstruction, outperforming the existing method PointOutNet Fan et al. [2017] in both qualitative and quantitative evaluations. The method is particularly suitable for 3D shape visualization needs in minimally invasive surgery and robot-assisted surgery.

## 5.3 Interpolation-based Methods

In generative models, point cloud interpolation (upsampling/completion) models Yu et al. [2018], Charles et al. [2017] achieve mesh reconstruction by completing missing parts of the structure. In this process, the input image is passed through a CNN to extract features and generate the target contour or sparse point cloud. An interpolation network then densifies the sparse point cloud, ultimately producing the final mesh. This approach is beneficial for handling occluded or incomplete medical images, effectively reconstructing missing structural information. Interpolation-based methods emphasize data-driven completion capabilities, allowing them to generate complete and detailed meshes even in challenging imaging environments.

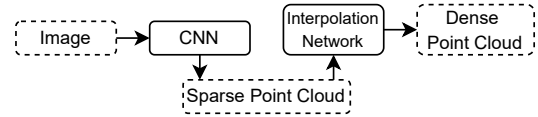


**Figure 13. Schematic representation of an interpolation-based method for mesh generation.** The input image is processed by a CNN to generate a sparse point cloud. This sparse point cloud is then refined by a completion network to produce a dense point cloud, which is subsequently converted into a mesh.

Based on Fig. 13, Beetz et al. [2022c] proposed Point2Mesh-Net, an innovative geometric deep learning approach that transforms 2D MR slices directly into 3D cardiac surface meshes. Its key innovations have two parts. First, they used dual architecture combining a point cloud-based encoder and mesh-based decoder, which enables the network to directly process sparse MR contour point clouds from image segmentation while outputting 3D triangular surface meshes suitable for downstream tasks. Second, they used a hierarchical design with multi-scale downsampling

and upsampling that enables effective feature learning and successfully addresses the two main challenges in cardiac surface reconstruction - data sparsity and slice misalignment.

Based on their previous work [Beetz et al. \[2022c\]](#), [Beetz et al. \[2023\]](#) further developed a novel multi-class Point Cloud Completion Network (PCCN) for reconstructing 3D cardiac anatomy from cardiac magnetic resonance images. Unlike previous completion methods, this approach uniquely addresses both sparsity and misalignment challenges within a single unified model. Furthermore, the network maintains both multi-class anatomical information (left ventricular cavity, left ventricular myocardium, right ventricular cavity) and bi-temporal cardiac phase data (end-diastolic and end-systolic) throughout the reconstruction process. This integrated design represents a significant advancement in cardiac anatomy reconstruction from medical imaging data.

[Beetz et al. \[2021\]](#) also proposed a deep learning method based on point completion networks to reconstruct dense 3D biventricular heart models from misaligned 2D cardiac MR contours. The method addresses both data sparsity and slice misalignment problems simultaneously. The method first segments 2D MR images to obtain contours, converts them to 3D point clouds, then reconstructs through a point completion network consisting of two PointNet [Charles et al. \[2017\]](#) encoder layers and a decoder with a FoldingNet [Yang et al. \[2018\]](#) block, finally generating meshes using the ball pivoting algorithm [Bernardini et al. \[1999\]](#).

[Xu et al. \[2019\]](#) also developed a completion network, but it performs completion at the voxel level rather than at the point cloud level. This method uses deep learning algorithms with a volumetric mapping approach to reconstruct 3D ventricular surfaces from 2D cardiac MR data and is capable of processing contours from multiple orientations and correcting motion artifacts. This approach transforms the mesh fitting problem into a volumetric mapping problem, using 3D U-Net to generate dense volumetric predictions from sparse input, followed by isosurfacing to obtain the final 3D surface. The method consists of three main steps: 1) generating sparse volumetric input data from contours; 2) generating dense 3D volumetric predictions of LV myocardium and LV/RV cavities using 3D U-Net; 3) generating 3D meshes from predictions using an isosurfacing algorithm.

Based on Fig. 13, [Wang et al. \[2023b\]](#) used a GNN for the completion network. Additionally, the input for this method was not a contour but two surface meshes, one from the template mesh and the other from the mesh of undetectable regions in the medical image. These two meshes are augmented with internal vertices based on the surface before being fed into the completion network. Specifically, this is a GCN-based approach for reconstructing un-

detectable regions of organs in medical images. The method transforms an initial template into patient-specific organ shapes using prior information obtained from detectable organs across different patients. To address inaccurate estimation results of GNN with triangular surface meshes, the authors introduced a method of adding internal vertices and edges, improving calculation accuracy by enhancing the mesh topology.

## 5.4 Diffusion-based Generative Model

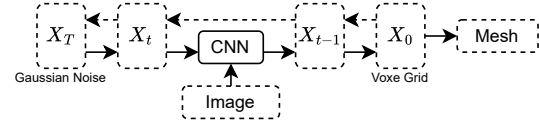


**Figure 14. Schematic representation of a diffusion model for medical surface reconstruction.**

Diffusion models [Ho et al. \[2020\]](#), [Kazerouni et al. \[2023\]](#) are a class of generative models that learn to generate data through a two-step process: a forward process and a backward process. In the forward process, structured data is gradually transformed into noise by iteratively adding small amounts of Gaussian noise over multiple timesteps. The backward process, also known as denoising, aims to recover the original data by learning to iteratively remove the noise in a controlled manner. This is typically achieved using deep neural networks such as U-Net [Ronneberger et al. \[2015\]](#), which predict and remove noise at each timestep to reconstruct the desired output.

One of the key advantages of diffusion models is their ability to handle reconstructions with missing information. They are particularly effective in tasks such as reconstructing 3D shapes from a single 2D image or recovering complete 3D structures from sparse 3D volumes, where information is inherently incomplete. However, diffusion models introduce diversity in the generated outputs, which can sometimes conflict with the fidelity required for high-precision reconstruction. When input information is sufficiently complete, such as in the case of converting a full 3D volume into a 3D mesh, diffusion models are rarely used. In this scenario, deterministic methods provide more accurate and reliable results.

Even for incomplete input to complete output reconstruction, there is currently no diffusion model designed for direct representation transfer in an end-to-end image-to-mesh pipeline. Instead, existing approaches leverage diffusion models to enhance image quality before applying segmentation or the marching cubes algorithm to generate the

final mesh.

Waibel et al. [2023] introduced DISPR, a diffusion-based model for reconstructing 3D cell shapes from 2D microscopy images. Instead of directly transferring representations from images to meshes, the model leverages diffusion processes to generate high-quality 3D volume reconstructions. DISPR is conditioned on the input 2D microscopy image and progressively refines noisy 3D volumes through multiple denoising steps, ensuring realistic shape predictions. The generated 3D structures are then evaluated using morphological features such as volume, surface area, and curvature, demonstrating superior performance over deterministic shape reconstruction methods. The model also serves as a data augmentation tool by generating additional synthetic training samples, improving the classification accuracy of single-cell morphological analysis.

He et al. [2023] proposed DMCVR, a framework that utilizes a morphology-guided diffusion model for 3D cardiac volume reconstruction from sparse 2D cine MRI slices. Instead of directly generating meshes, the method enhances the axial resolution of 2D MR images by employing a diffusion-based generative process conditioned on both global semantic and regional morphology latent codes. The global semantic encoder captures high-level anatomical features, while the regional morphology encoder focuses on specific cardiac structures (left ventricle cavity, left ventricle myocardium, and right ventricle cavity) to improve anatomical accuracy. Song et al. [2020] used denoising diffusion implicit models to iteratively refine reconstructed slices, which are then stacked to form a complete 3D volume. By incorporating latent-space interpolation techniques, DMCVR ensures smooth and high-resolution 3D reconstructions, outperforming traditional interpolation and GAN-based method Chang et al. [2022] in cardiac volume generation.

Wodzinski et al. [2024] applied latent diffusion models (LDMs) proposed by Rombach et al. [2022] to cranial defect surface reconstruction by using them as a data augmentation technique to improve deep learning-based reconstruction models. Instead of directly using diffusion models for end-to-end surface reconstruction, the approach leverages LDMs in the latent space to generate synthetic defective skulls, which are then used to enhance the training dataset for cranial defect reconstruction networks. The latent diffusion model refines the variational autoencoder (VAE) Kingma and Welling [2014] or vector quantized VAE van den Oord et al. [2017] representations by incrementally adding and denoising noise in the latent space, thereby producing more diverse and realistic cranial defect samples. This augmentation significantly improves the generalizability of the reconstruction network, enabling it to reconstruct real clinical cranial defects despite being trained solely on synthetic datasets.

## 6 Implicit Models

Implicit models are a class of methods that use neural networks to learn continuous functions for representing 3D shapes. Unlike traditional explicit methods such as voxel grids or point clouds, implicit models do not directly store geometric information but instead leverage multilayer perceptrons (MLPs) Pinkus [1999] to learn an implicit function value for each spatial point, thereby defining the 3D structure indirectly. Common types of implicit models summarized in Table 15 include signed distance functions (SDF), neural ordinary differential equations (Neural ODE), occupancy functions, and neural radiance fields (NeRF). SDF models represent shapes by learning the signed distance from a point to the surface, Neural ODEs model dynamic structures by learning the temporal evolution of shapes, occupancy function models predict whether a point belongs to an object’s interior using binary classification, and NeRF incorporates density and colour information to enable both geometric reconstruction and rendering.

The advantage of implicit models lies in their high-resolution and continuous representation capabilities, making them independent of fixed-resolution constraints and highly efficient for handling complex geometries. This makes them particularly valuable in fields such as medical image reconstruction, computer vision, and computer graphics, especially for tasks requiring precise surface reconstruction, such as mesh generation from medical scans, scene reconstruction, and shape optimization based on physical simulations.

### 6.1 Neural ODE

Neural ordinary differential equation (Neural ODE) methods are a variant of GCN-based approaches that model the deformation process as a continuous dynamic system. In this framework, features are first extracted from the input image using CNN or MLP, and a neural ODE governs the deformation of a template mesh. The neural ODE evolves the template over time to fit the target shape, described by:

$$\frac{dV(x, t)}{dt} = f(x, t),$$

where  $V(x, t)$  represents the state of a vertex  $x$  at time  $t$ , and  $f(x, t)$  is the velocity field driving the deformation. This method produces smooth deformation trajectories, ensuring mesh stability and physical plausibility. Additionally, it provides not only the deformed mesh but also the velocity field or dynamic deformation information, making it particularly suitable for tasks requiring continuous and nonlinear deformations.

In contrast, the Deformation Field method applies instantaneous displacement directly to the mesh vertices, de-

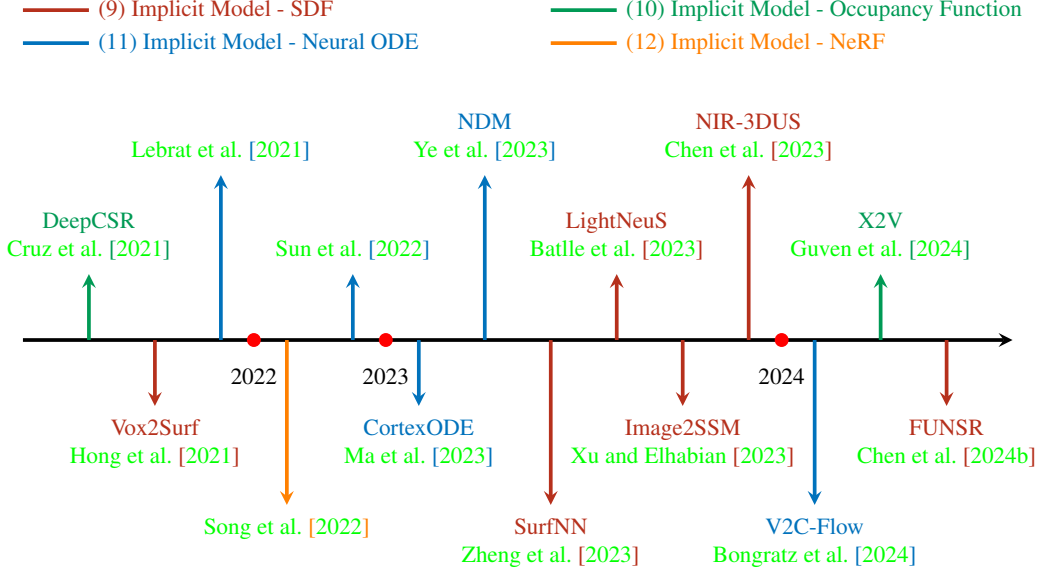


Figure 15. Chronological overview of representative deep learning-based implicit models for medical image-to-mesh reconstruction.

Table 4. Implicit Models for Medical Image-to-Mesh Reconstruction

Name	Method	Input	Output	Anatomy	Modality	Dataset
CortexODE Ma et al. [2023]	Neural ODE	3D Image	Surface Meshes	Brain Cortex	MR-T1w/T2w	dHCP (874), HCP (600), ADNI (524)
FUNSR Chen et al. [2024b]	SDF	Segmentation masks	Surface mesh (SDFs)	Hip, carotid artery, Prostate	3D Freehand Ultrasound	Hip phantom (2), CCA (10), CAB (77), Prostate (73)
Vox2Surf Hong et al. [2021]	SDF	T1w and T2w MR	Surface meshes	Brain	MR	HCP (22)
LightNeuS Batlle et al. [2023]	SDF	Monocular endoscopic video frames	Watertight Surface Mesh	Colon	Endoscopy	C3VD dataset (22)
NIR-3DUS Chen et al. [2023]	UDF	3D images	Surface mesh (MAB, plaque, LIB)	Carotid artery	3D Ultrasound	simulated volumes (6), Private data (5)
SurfNN Zheng et al. [2023]	SDF	3D MR + mesh)	WM + pial + Midthickness surface	Brain cortical surfaces	T1 MR	ADNI (747/70/113 train/val/test)
DeepCSR Cruz et al. [2021]	Occupancy Function	T1w MR	Inner and outer cortical surfaces	Brain cortex	MR	ADNI (3876 MRIs), Test-Retest (120 MRIs), MALC (30 MRIs)
X2V Guven et al. [2024]	Occupancy Function	Single X-ray DRR	3D Mesh	Lung	X-ray	NLST (6,392 CT scans from 2,560 subjects)
Image2SSM Xu and Elhabian [2023]	SDF	Image-Segmentation pairs	PDMs/Surface mesh	Femur/Left atrium	CT/MR	50 proximal femur CT scans
NDM Ye et al. [2023]	Neural ODE	Sparse point cloud (2D CMR slices)	Dense mesh with deformations	Bi-ventricular heart	CMR	Cardiac SSM
V2C-Flow Bongratz et al. [2024]	Neural ODE	3D Image	Surfaces Mesh	Brain Cortex	MRI-T1w	ADNI, J-ADNI, OASIS, Mindboggle, TRT, JHU
CorticalFlow Lebrat et al. [2021]	Neural ODE	3D Image	Surface Mesh	Brain Cortex	MR	ADNI

scribed as:

$$x' = x + D(x),$$

where  $D(x)$  is the displacement vector at point  $x$ . While simpler and more efficient, this approach is better suited for small or localized deformations due to its discrete nature.

The primary distinction between the two methods lies in their treatment of deformation: neural ODEs model deformation as a time-dependent, continuous process, whereas

the Deformation Field represents deformation as an instantaneous, discrete operation. This makes neural ODEs particularly advantageous for scenarios requiring smooth, large-scale deformations, while deformation fields excel in cases where efficiency and simplicity are priorities.



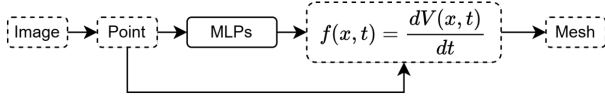


**Figure 16. Schematic of Neural ODE-based methods.** In Neural ODEs,  $x$  represents a point in 3D space,  $t$  is the time parameter that controls the dynamic evolution,  $V(x, t)$  denotes the state of the point  $x$  at time  $t$  (such as its deformation during surface reconstruction), and  $f(x, t)$  describes the dynamic system governing how the state evolves over time.

## 6.2 Diffeomorphic flow-based deformations

Based on Fig. 16, Lebrat et al. [2021] used a differential mesh deformation module to replace the deformation GCN. This method introduces a novel geometric deep-learning model that utilizes a flow ordinary differential equation framework to learn a series of diffeomorphic transformations, deforming a reference template mesh towards a target object, thereby achieving efficient cortical surface reconstruction

NODE Sun et al. [2022] proposed a new model called Neural Diffeomorphic Flow (NDF), using a generative model to represent 3D shapes as deformations of implicit shape templates, preserving the topological structure of shapes, and employing an autoencoder with Neural Ordinary Differential Equation (NODE) blocks to realize diffeomorphic deformation.

Based on Fig. 16, Ye et al. [2023] used a multi-level structure to achieve coarse-to-fine mesh reconstruction. This method proposes a neural deformable model (NDM) to reconstruct complete 3D bi-ventricular heart shapes from sparse cardiac magnetic resonance images. NDM combines traditional deformable superquadrics with modern deep learning techniques, adopting a two-stage strategy: first using parameterized functions for global deformation to capture coarse shape, then employing neural diffeomorphic flows for local deformation to recover details.

Based on Fig. 16, Bongratz et al. [2024] upgraded the algorithm from Bongratz et al. [2022], using NODE to achieve cortical surface reconstruction, and further introduced separate templates for different regions. This method (V2C-Flow) is an end-to-end deep learning method based on neural ODEs for cortical surface reconstruction from MRI. The method generates white matter and pial surfaces by deforming template meshes while maintaining vertex correspondences. V2C-Flow reconstructs all four cortical

surfaces simultaneously, runs fast (1.6 seconds), and ensures geometric accuracy through a curvature-weighted Chamfer loss.

Ma et al. [2023] introduced CortexODE, a deep learning framework for cortical surface reconstruction. The method leverages neural ordinary differential equations (Neural ODEs) to learn a diffeomorphic flow that deforms an input surface into a target shape. The implementation first uses a 3D U-Net to predict white matter segmentation from brain MR scans, then generates a signed distance function and performs fast topology correction to ensure homeomorphism to a sphere. Following surface extraction, two CortexODE models are trained to deform the initial surface to white matter and pial surfaces respectively. The entire pipeline completes cortical surface reconstruction in less than 5 seconds while ensuring high geometric accuracy and minimal self-intersections.

## 6.3 Signed Distance Function (SDF)

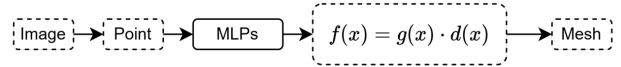


**Figure 17. Schematic of SDF methods.** In the signed distance function,  $x$  represents a point in 3D space,  $d(x)$  is the distance from  $x$  to the target surface, and  $g(x)$  indicates whether  $x$  is inside (negative sign) or outside (positive sign) the surface. The  $g(x)$  is often determined based on the gradient of the distance function. Together, these elements describe the signed distance value of the point  $x$  with respect to the surface.

a

Signed distance function (SDF) is a fundamental implicit surface representation that defines a continuous field where each point in space is assigned a value representing the signed distance to the closest point on the surface. The sign indicates whether the point is inside (negative) or outside (positive) the surface, while the surface itself is represented by the zero-level set. Formally, for a point  $x \in \mathbb{R}^3$ , the SDF is defined as:

$$f(x) = \text{sign}(x) \cdot d(x), \quad (1)$$

where  $d(x)$  is the Euclidean distance from  $x$  to the closest point on the surface. The sign of  $f(x)$  can be determined based on the gradient of the distance function:

$$\text{sign}(x) = \begin{cases} -1, & \text{if } \nabla d(x) \cdot \mathbf{n}(x) < 0, \\ 1, & \text{if } \nabla d(x) \cdot \mathbf{n}(x) > 0, \end{cases} \quad (2)$$

where  $\nabla d(x)$  is the gradient of the distance function at  $x$ , and  $\mathbf{n}(x)$  is the unit normal vector pointing outward from the surface at the closest point. The zero-level set of the SDF, where  $f(x) = 0$ , defines the exact location of the surface. SDFs not only provide a compact and differentiable representation of geometry but also encode rich geometric information such as the distance to the surface, which can be utilized in various applications like surface reconstruction, simulation, and optimization tasks.

SDF provides several advantageous properties for mesh reconstruction. It offers a continuous and differentiable representation of the surface, enabling smooth optimization and gradient-based learning. The representation naturally handles topological changes and complex geometries without explicit mesh manipulation. Additionally, the gradient of the SDF directly gives the surface normal direction, facilitating the computation of geometric properties like surface curvature. In medical image-to-mesh reconstruction, SDFs are particularly useful as they can represent complex anatomical structures while maintaining smoothness and allowing for topology changes. The implicit nature of SDFs makes them well-suited for deep learning frameworks, where networks can be trained to predict the signed distance field from medical images.

Chen et al. [2024b] presented FUNSR, a self-supervised neural implicit surface reconstruction method for freehand 3D ultrasound data. The method directly transforms segmentation masks into volumetric point clouds as input and learns signed distance functions through neural networks to represent anatomical surfaces. Two geometric constraints are introduced: sign consistency constraint and surface constraint with adversarial learning, to improve reconstruction quality. The entire network is trained end-to-end in a self-supervised manner without requiring additional ground truth data or post-processing.

Chen et al. [2023] presented a neural implicit representation approach for 3D ultrasound carotid surface reconstruction. The method first employs a U-Net for multi-class segmentation of ultrasound images to obtain vessel boundary point clouds, then uses a multi-layer perceptron network to learn unsigned distance functions (UDF) for reconstructing smooth and continuous vessel surfaces. Compared to the traditional iso-surface method Remelli et al. [2020], this approach generates smoother and more continuous geometric surfaces.

Hong et al. [2021] presented Vox2Surf, a method for direct surface reconstruction of cortical and subcortical structures from volumetric MR data. The method learns a continuous-valued signed distance function (SDF) as implicit surface representation using deep learning, combining global and local features for surface reconstruction. The network can handle multiple brain structures simultaneously.

Battle et al. [2023] presented LightNeuS, a neural network approach for endoscopic 3D reconstruction. The method is based on two key insights: first, endoluminal cavities are watertight, naturally enforced through signed distance function (SDF) representation; second, scene illumination varies and decays with inverse square distance from the endoscope light source to the surface. By explicitly incorporating illumination decline in the NeuS architecture and introducing a calibrated photometric model, the method achieves watertight reconstruction of complete colon sections with high accuracy on phantom data.

Zheng et al. [2023] introduced SurfNN for cortical surface reconstruction from MR images. Its novelty lies in simultaneously reconstructing both inner (white-gray matter boundary) and outer (pial) surfaces by training a single network to predict a midthickness surface that lies at the centre of both surfaces. The method takes as input a 3D MR and an initialization of the midthickness surface represented both as a distance map and triangular mesh, outputting the inner, outer, and midthickness surfaces.

## 6.4 NeRF

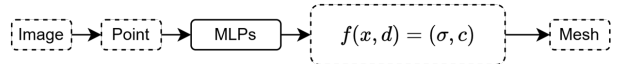


**Figure 18. Schematic of NeRF methods.** In neural radiance fields,  $x$  is a point in 3D space, and  $d$  is the viewing direction. The density  $\sigma$  represents the likelihood of the point  $x$  being part of the object’s surface, and the colour  $c$  (in RGB) provides information about the appearance of the surface at  $x$ . For surface reconstruction, the surface geometry can be extracted as the iso-surface where the density  $\sigma$  exceeds a threshold.

Neural Radiance Field (NeRF) Mildenhall et al. [2021], Velikova et al. [2024], Barron et al. [2021] represents 3D scenes by learning a continuous volumetric function using a neural network. While originally designed for novel view synthesis, NeRF has been adapted for medical image-to-mesh reconstruction tasks. The core idea of NeRF is to model a scene as a continuous function that maps every 3D spatial location  $x = (x, y, z)$  and viewing direction  $d = (\theta, \phi)$  to a volume density  $\sigma$  and RGB colour  $c$ :

$$F : (x, d) \rightarrow (\sigma, c). \quad (3)$$

In medical applications, this formulation is typically modified to focus on surface reconstruction rather than radiance modelling. The viewing direction  $d$  is omitted, and

the output is adapted to represent volumetric density for anatomical surface extraction:

$$F : x \rightarrow \sigma. \quad (4)$$

Here,  $x$  represents a point in 3D space, and  $\sigma$  represents the likelihood of  $x$  being part of the object’s surface. For surface reconstruction tasks, the geometry of the surface can be extracted from the volumetric density representation using techniques like marching cubes or isosurface extraction.

The key advantage of NeRF-based approaches in medical imaging is their ability to handle multi-view consistency and incorporate 3D spatial context naturally. The continuous nature of the representation allows for high-resolution reconstruction and smooth interpolation between views. Additionally, the volumetric formulation is particularly well-suited for medical imaging modalities that inherently capture volumetric data, such as CT or MR scans.

Song et al. [2022] presented a deep learning-based 3D ultrasound reconstruction algorithm to improve the quality of carotid artery volume reconstruction. The method uses a multi-layer perceptron (MLP) network to implicitly infer and represent both intensity and semantic probability of voxels in the image volume. By combining semantic segmentation information with volume intensity, the method produces smoother and more continuous vessel wall reconstructions compared to traditional VNN methods.

## 6.5 Occupancy Function

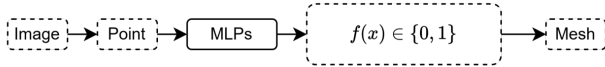


**Figure 19. Schematic of occupancy function methods. In the occupancy function,  $x$  is a point in 3D space, and  $f(x)$  outputs a binary value indicating whether  $x$  is inside or outside a target object. If  $f(x) = 1$ , the point is inside the object; if  $f(x) = 0$ , the point is outside.**

The occupancy function provides another form of implicit surface representation where each point in space is assigned a binary value indicating whether it lies inside or outside the shape. Formally, for a surface  $\mathcal{S}$  that bounds a volume  $\mathcal{V}$ , the occupancy function  $f(x)$  for a point  $x$  is defined as:

$$f(x) \in \{0, 1\}, \quad (5)$$

where  $f(x) = 1$  if the point  $x$  lies inside the volume  $\mathcal{V}$ , and  $f(x) = 0$  otherwise.

In practice, deep learning approaches often approximate this binary occupancy function with a continuous field that

outputs values in the range  $[0, 1]$ , representing the probability of a point being inside the shape. The final surface is then extracted as the isosurface where  $f(x) = 0.5$ . Compared to Signed Distance Functions (SDFs), occupancy functions are simpler to represent but provide less geometric information since they do not encode distance to the surface. However, they are particularly effective for binary segmentation tasks and can be more efficient to train as they focus on inside/outside classification rather than on precise distance values.

Cruz et al. [2021] introduced DeepCSR for cortical surface reconstruction. The method first aligns input MR images with a brain template, then uses a neural network with hypercolumn features to predict occupancy representations for points in a continuous coordinate system. The cortical surface at a desired level of detail is obtained by evaluating surface representations at specific coordinates, followed by topology correction and isosurface extraction. Through its continuous nature and effective hypercolumn feature scheme, the method efficiently reconstructs high-resolution cortical surfaces capturing fine details in cortical folding.

Guven et al. [2024] presented X2V, an innovative approach for 3D organ volume reconstruction from a single planar X-ray image. The method employs a Vision Transformer as an encoder for X-ray image feature processing, combined with neural implicit representation for 3D shape reconstruction. Unlike traditional methods that rely on statistical 3D organ templates, X2V learns an occupancy probability function to represent 3D surfaces, effectively handling organ shape variations across different subjects.

In medical image-to-mesh reconstruction, occupancy functions are often used when the primary goal is to determine anatomical boundaries or segment specific structures. They have been successfully applied to various anatomical reconstruction tasks, particularly when combined with deep learning architectures that can learn complex shape priors from training data.

## 7 Loss Functions for Image to Mesh Reconstruction

This section provides an overview of the loss functions used in image-to-mesh reconstruction tasks, focusing on two main categories: shape similarity and shape regularization. Each category includes detailed explanations of specific loss functions and their underlying principles, organized by the representation they rely on, such as points/vertices, normal vectors, edges, etc.

**Table 5. Loss Functions for Image-to-Mesh Reconstruction.**

Loss Function	Representation	References
Distance and Consistency Losses		
Chamfer Distance	Point	Kong et al. [2021] Meng et al. [2024] Ye et al. [2023] Zhao et al. [2023b] Krüger et al. [2024] Kong and Shadden [2021] Lebrat et al. [2021] Wang et al. [2020b] Chen et al. [2021] Ma et al. [2023] Zheng et al. [2023] Beetz et al. [2021] Beetz et al. [2024] Bongratz et al. [2022] Bongratz et al. [2024]
Hausdorff Distance	Point	Meng et al. [2022a] Meng et al. [2024]
Average Symmetric Surface Distance	Point	Hoopes et al. [2022]
Mean Squared Error	Point/Latent/Implicit	Gaggion et al. [2024] Bransby et al. [2023] Aziz et al. [2023] Govil et al. [2023] Beetz et al. [2022b] Ma et al. [2021] Tong et al. [2020] Upendra et al. [2021a] Ma et al. [2023] Xia et al. [2022] Romaszko et al. [2021] Geng et al. [2024] Hong et al. [2021] Kong and Shadden [2023] Wang et al. [2023b] Geng et al. [2024] Chen et al. [2024b] Chen et al. [2023] Meng et al. [2024] Song et al. [2022] Ruiz et al. [2018] Yuan et al. [2023] Battle et al. [2023] Xu and Elhabian [2023] Nakao et al. [2021b] Gilbert et al. [2020] Meng et al. [2022a] Zhao et al. [2022] Bransby et al. [2023]
Mean Absolute Error	Point/Latent/Implicit	Attar et al. [2019a] Zhao et al. [2021] Beetz et al. [2022a] Chen et al. [2021] Kong and Shadden [2023] Cruz et al. [2021]
Mean Squared Error Frobenius norm	Point	Bhalodia et al. [2024]
Mahalanobis Distance	Point	Ruiz et al. [2018]
Dice Similarity Coefficient	Voxel	Bransby et al. [2023] Kong et al. [2021] Govil et al. [2023] Kong and Shadden [2021] Tang et al. [2021] Xu et al. [2019]
Binary Cross-Entropy	Distribution/Implicit	Aziz et al. [2023] Bongratz et al. [2022] Zhao et al. [2023b] Tang et al. [2021] Cruz et al. [2021] Guven et al. [2024] Laumer et al. [2023] Chen et al. [2024b]
Cross-Entropy	Distribution	Bransby et al. [2023] Kong et al. [2021] Laumer et al. [2023] Romaszko et al. [2021] Govil et al. [2023] Bongratz et al. [2024] Zhao et al. [2021] Krüger et al. [2024] Kong and Shadden [2021] Rickmann et al. [2022] Ma et al. [2023] Song et al. [2022]
Sparse Categorical Cross Entropy	Distribution	Govil et al. [2023]
Centerline Coverage Loss	Point	Krüger et al. [2024]
Sign Consistency Constraint	Implicit	Chen et al. [2024b]
Shape Consistency Loss	Point	Gilbert et al. [2020] Nakao et al. [2021b] Bhalodia et al. [2024]
Structural Similarity Loss	Voxel	Yeung et al. [2024]
Correspondences Loss	Point	Bhalodia et al. [2024] Xu and Elhabian [2023]
Fixed Loss	Point	Aziz et al. [2023]
Sampling Loss	Point / Normal Vector	Xu and Elhabian [2023]
Photometric Loss	Voxel	Battle et al. [2023], Yeung et al. [2024]
Vertex Classification Loss	Point	Krüger et al. [2024]
Regularization and Smoothness Losses		
Laplacian Smoothness	Point	Bransby et al. [2023] Kong et al. [2021] Meng et al. [2022a] Meng et al. [2024] Bongratz et al. [2022] Zhao et al. [2023b] Nakao et al. [2021b] Krüger et al. [2024] Wang et al. [2023b] Geng et al. [2024] Upendra et al. [2021a] Chen et al. [2021] Nakao et al. [2021a]
Normal Consistency (subtraction / dot product / cosine similarity)	Normal Vector	Kong et al. [2021] Bongratz et al. [2024] Krüger et al. [2024] Zheng et al. [2023] Bransby et al. [2023] Xu and Elhabian [2023] Zhao et al. [2023b] Lebrat et al. [2021] Bongratz et al. [2022] Kong and Shadden [2023]
Tetrahedral Element Regularization Loss	Volume	Gaggion et al. [2024]
Edge Length Regularization Loss	Edge	Kong et al. [2021] Bongratz et al. [2022] Bongratz et al. [2024] Zhao et al. [2023b] Krüger et al. [2024] Zheng et al. [2023]
Point-pair Regularization Loss	Point	Yuan et al. [2023]
Mesh Regularization Loss for Co-planarity	Normal Vector	Kong and Shadden [2023]
Discrete Laplacian Loss	Point	Tong et al. [2020]
Local Deformation Smoothness	Point	Ye et al. [2023]
Grid Elasticity Loss	Point	Kong and Shadden [2021]
Local Deformation Amount	Point	Ye et al. [2023]
Intra-mesh Normal Consistency	Normal Vector	Bongratz et al. [2022]
Geometric Regularization (hinge-spring)	Normal Vector	Hoopes et al. [2022]
Distribution-based and Energy-Based Losses		
Kullback–Leibler Divergence	Distribution	Gaggion et al. [2024]
Statistical Parameter Loss	Latent Feature	Gilbert et al. [2020]
Deep/Shallow Supervision Loss: Point	Point	Aziz et al. [2023]
Huber Loss	Point	Meng et al. [2024] Yuan et al. [2023]
Focal Loss	Latent Feature	Bhalodia et al. [2024]
Multiple Manifold Learning Loss	Latent Feature	Maxime et al. [2022]
Network Weight Regularization Loss	Latent Feature	Bhalodia et al. [2024]
Energy Function	Point	Ruiz et al. [2018] Xu and Elhabian [2023]
TPS Deformation Energy	Point	Banerjee et al. [2022]

## 7.1 Shape Similarity Losses

Shape similarity losses measure how well the reconstructed mesh matches the ground truth shape in terms of geometry and structure.

### 7.1.1 Point/Vertex-Based Losses

Chamfer Distance computes the average closest point distance between two point sets  $P$  (predicted) and  $Q$  (ground

truth):

$$CD(P, Q) = \frac{1}{|P|} \sum_{p \in P} \min_{q \in Q} \|p - q\|_2^2 + \frac{1}{|Q|} \sum_{q \in Q} \min_{p \in P} \|q - p\|_2^2. \quad (6)$$

Hausdorff Distance measures the maximum distance from a point in one set to the closest point in the other set:

$$HD(P, Q) = \max \left\{ \max_{p \in P} \min_{q \in Q} \|p - q\|, \max_{q \in Q} \min_{p \in P} \|q - p\| \right\}. \quad (7)$$

This loss emphasizes the worst-case scenario by penalizing

the largest deviation between the two point sets.

Average Symmetric Surface Distance (ASSD) calculates the average bidirectional surface distance:

$$\text{ASSD}(P, Q) = \frac{1}{|P| + |Q|} \left( \sum_{p \in P} \min_{q \in Q} \|p - q\| + \sum_{q \in Q} \min_{p \in P} \|q - p\| \right). \quad (8)$$

Unlike Chamfer Distance, ASSD considers both directions with equal weight and focuses on surface-to-surface comparison.

Mean Surface Distance (MSD) measures the average distance between corresponding points on two surfaces:

$$\text{MSD}(P, Q) = \frac{1}{|P|} \sum_{p \in P} \|p - q_p\|_2, \quad (9)$$

where  $q_p$  is the closest point to  $p$  on the other surface.

Mean Squared Error (MSE) computes the average squared distance between the predicted and ground truth points:

$$\text{MSE}(P, Q) = \frac{1}{|P|} \sum_{p \in P} \|p - q_p\|_2^2. \quad (10)$$

MSE penalizes large errors more significantly than small errors due to the squared term.

Root Mean Squared Error (RMSE) is the square root of MSE, which retains the same unit as the input:

$$\text{RMSE}(P, Q) = \sqrt{\frac{1}{|P|} \sum_{p \in P} \|p - q_p\|_2^2}. \quad (11)$$

This metric provides a direct interpretation of the average error magnitude.

$L_2$  Consistency measures the Euclidean distance between the predicted and ground truth points:

$$L_2(P, Q) = \frac{1}{|P|} \sum_{p \in P} \|p - q_p\|_2. \quad (12)$$

This loss is essentially the same as MSD, but without explicitly focusing on corresponding points on surfaces.

In summary, point/vertex-based losses differ in how they handle the distances between the predicted and ground truth sets. Chamfer Distance considers bidirectional distances but is averaged, making it more robust to outliers compared to Hausdorff Distance. Hausdorff Distance penalizes the largest deviation, making it sensitive to outliers but useful for ensuring no extreme mismatches exist. ASSD and MSD are similar but differ in their weighting schemes. ASSD averages distances bidirectionally, while MSD focuses on one direction (e.g., from predicted to ground truth). MSE and RMSE both penalize large deviations, but RMSE retains the original unit of the measurements for interoperability.

$L_2$  Consistency is equivalent to MSD in form but is often applied in different contexts to measure alignment or similarity. These losses complement each other, and the choice depends on the specific application requirements, such as sensitivity to outliers or robustness to noise.

### 7.1.2 Normal Vector-Based Losses

Normal Consistency Loss measures the angular alignment between the predicted normals  $\mathbf{n}_f$  and ground truth normals  $\mathbf{n}_f^{\text{GT}}$ :

$$L_{\text{normal}} = \frac{1}{|F|} \sum_{f \in F} (1 - \mathbf{n}_f \cdot \mathbf{n}_f^{\text{GT}}). \quad (13)$$

Inter-Mesh Normal Consistency penalizes discrepancies in normals of shared edges between adjacent faces:

$$L_{\text{inter}} = \frac{1}{|E|} \sum_{e \in E} (1 - \cos(\theta_e)), \quad (14)$$

where  $\theta_e$  is the angle between adjacent face normals. This loss function controls the smoothness and geometric continuity of a mesh by minimizing sharp changes in normals between adjacent faces. This ensures smoother surface reconstruction, preserves natural curvature and anatomical features, and reduces noise and artifacts.

Normal Difference Loss minimizes the Euclidean distance between corresponding predicted and ground truth normals on the mesh:

$$L_{\text{normal-diff}} = \frac{1}{|F|} \sum_{f \in F} \|\mathbf{n}_f - \mathbf{n}_f^{\text{GT}}\|_2^2. \quad (15)$$

### 7.1.3 Latent Feature-Based Losses

Focal Loss is used for class-imbalanced tasks to focus on hard-to-classify samples:

$$\text{FL}(p_t) = -\alpha(1 - p_t)^\gamma \log(p_t), \quad (16)$$

where  $p_t$  is the predicted probability for the true class.

Mean Squared Error (Latent) measures the squared error between predicted and ground truth latent feature vectors:

$$\text{MSE}(\mathbf{z}_{\text{pred}}, \mathbf{z}_{\text{true}}) = \frac{1}{N} \sum_{i=1}^N (\mathbf{z}_{\text{pred},i} - \mathbf{z}_{\text{true},i})^2. \quad (17)$$

Adversarial Loss is used in GANs to ensure the predicted latent space resembles the real latent space:

$$L_{\text{adv}} = \mathbb{E}[\log(D(\mathbf{z}_{\text{true}}))] + \mathbb{E}[\log(1 - D(\mathbf{z}_{\text{pred}}))], \quad (18)$$

where  $D$  is the discriminator.



### 7.1.4 Implicit Representations

SDF Regression Loss measures the squared error between predicted and ground truth signed distance values:

$$L_{\text{SDF}} = \frac{1}{N} \sum_{i=1}^N \|f(\mathbf{x}_i) - \text{SDF}(\mathbf{x}_i)\|_2^2. \quad (19)$$

Sign Consistency Constraint ensures that the predicted SDF values maintain the same sign as the ground truth:

$$L_{\text{sign}} = \frac{1}{N} \sum_{i=1}^N \text{ReLU}(-f(\mathbf{x}_i) \cdot \text{SDF}(\mathbf{x}_i)). \quad (20)$$

Volume Rendering Loss penalizes differences in density or colour values for implicit surface representations:

$$L_{\text{vol}} = \int \|c_{\text{pred}}(\mathbf{r}) - c_{\text{true}}(\mathbf{r})\|_2^2 d\mathbf{r}, \quad (21)$$

where  $c_{\text{pred}}$  and  $c_{\text{true}}$  are predicted and true colors.

### 7.1.5 Voxel-Based Losses

Structural Similarity Index (SSIM) [Sampat et al. \[2009\]](#) measures structural similarity between two voxel images:

$$\text{SSIM}(x, y) = \frac{(2\mu_x\mu_y + C_1)(2\sigma_{xy} + C_2)}{(\mu_x^2 + \mu_y^2 + C_1)(\sigma_x^2 + \sigma_y^2 + C_2)}. \quad (22)$$

SSIM consists of three components: luminance, contrast, and structure, which together assess different aspects of similarity between two images. Luminance comparison measures the similarity of brightness between two images:

$$l(x, y) = \frac{2\mu_x\mu_y + C_1}{\mu_x^2 + \mu_y^2 + C_1}, \quad (23)$$

where  $\mu_x$  and  $\mu_y$  are the mean intensities of images  $x$  and  $y$ , and  $C_1$  is a constant to stabilize the denominator. Contrast comparison evaluates the similarity of contrast between two images:

$$c(x, y) = \frac{2\sigma_x\sigma_y + C_2}{\sigma_x^2 + \sigma_y^2 + C_2}, \quad (24)$$

where  $\sigma_x$  and  $\sigma_y$  are the standard deviations of images  $x$  and  $y$ , and  $C_2$  is another stability constant. Structure comparison measures the structural alignment between two images:

$$s(x, y) = \frac{\sigma_{xy} + C_3}{\sigma_x\sigma_y + C_3}, \quad (25)$$

where  $\sigma_{xy}$  is the covariance between  $x$  and  $y$ , and  $C_3$  is typically set as  $C_3 = C_2/2$ . These three components—luminance, contrast, and structure—are combined multiplicatively to form the SSIM index, providing a comprehensive similarity metric for image quality assessment.

## 7.2 Shape Regularization Losses

Shape regularization losses improve the geometric properties of the reconstructed mesh, ensuring it is smooth, realistic, and well-formed.

### 7.2.1 Point/Vertex-Based Losses

Huber Loss combines the benefits of MSE and MAE for robustness to outliers:

$$L_\delta(a) = \begin{cases} \frac{1}{2}a^2 & \text{if } |a| \leq \delta, \\ \delta(|a| - \frac{\delta}{2}) & \text{if } |a| > \delta, \end{cases} \quad (26)$$

where  $a = y_{\text{pred}} - y_{\text{true}}$ .

Laplacian Smoothness Loss ensures surface smoothness by minimizing the Laplacian operator applied to vertices:

$$L_{\text{lap}} = \sum_{i=1}^N \|\mathbf{v}_i - \frac{1}{|\mathcal{N}_i|} \sum_{j \in \mathcal{N}_i} \mathbf{v}_j\|_2^2, \quad (27)$$

where  $\mathcal{N}_i$  is the neighborhood of vertex  $i$ .

### 7.2.2 Normal Vector-Based Losses

Orthogonal Loss enforces perpendicularity of surface normals at specific regions (e.g., vessel caps):

$$L_{\text{orthogonal}} = \sum_{v \in V_{\text{cap}}} |\mathbf{n}_v \cdot \mathbf{n}_{\text{cap}}|, \quad (28)$$

where  $\mathbf{n}_v$  is the normal at vertex  $v$ , and  $\mathbf{n}_{\text{cap}}$  is the target cap normal.

Intra-Mesh Normal Consistency ensures adjacent faces in the same mesh have consistent normals:

$$L_{\text{intra}} = \frac{1}{|E|} \sum_{e \in E} (1 - \mathbf{n}_{f_1} \cdot \mathbf{n}_{f_2}), \quad (29)$$

where  $\mathbf{n}_{f_1}$  and  $\mathbf{n}_{f_2}$  are the normals of the two faces sharing edge  $e$ .

### 7.2.3 Edge-Based Losses

Edge Length Regularization enforces uniform edge lengths across the mesh:

$$L_{\text{edge}} = \frac{1}{|E|} \sum_{(i,j) \in E} \|\mathbf{v}_i - \mathbf{v}_j\|_2^2. \quad (30)$$

### 7.2.4 Volume-Based Losses

Tetrahedral Element Regularization Loss ensures uniformity in tetrahedral mesh volumes:

$$L_{\text{tetra}} = \sum_{i=1}^N \left( \frac{V_i}{V_{\text{ref}}} - 1 \right)^2, \quad (31)$$

where  $V_i$  is the volume of the  $i$ -th tetrahedral element.

## 8 Evaluation Metrics

To evaluate the accuracy of the predicted shapes, several evaluation metrics were used to compare the predicted shapes with the reference shapes. Table 6 provides a summary of these evaluation metrics.

### 8.1 Shape Similarity

Shape similarity evaluation measures the geometric accuracy and structural consistency of a reconstructed mesh by comparing it to a reference ground-truth mesh. These evaluations are essential for assessing the reliability of medical image-to-mesh reconstruction methods, ensuring that the generated meshes faithfully represent anatomical structures.

#### 8.1.1 Distance

Distance evaluation metrics assess the geometric accuracy of the reconstructed mesh by quantifying the spatial discrepancy between the predicted and ground-truth surfaces. These metrics include point-based distance measures, such as Chamfer distance, earth mover distance, and Hausdorff distance, which evaluate deviations at specific sampled points. Additionally, surface-based distance metrics, such as average symmetric surface distance, mean surface distance, and median surface distance, provide a global assessment of surface deviation. Error-based metrics, including mean squared error, mean absolute error, and root mean squared error, quantify the overall distribution of reconstruction errors, offering a comprehensive evaluation of mesh reconstruction accuracy.

#### 8.1.2 Consistency

Consistency evaluation metrics assess the structural and geometric stability of the reconstructed mesh, ensuring that the reconstructed shape not only matches the target but also maintains consistency in local features, volume, and surface area. These metrics include normal consistency measures, such as normal vector consistency, which is computed using cosine similarity or dot product, and regional similarity metrics like Dice similarity coefficient, which evaluates the overlap between the reconstructed and ground-truth meshes. Additionally, classification-based evaluation metrics, including F-score, intersection over union, and confusion matrix, assess the accuracy of segmented regions. Structural similarity evaluation, such as structural similarity index measure, quantifies the local structural resemblance between the meshes. Geometric consistency evaluation involves volume consistency and surface area consistency, ensuring that the reconstructed mesh adheres to anatomical

standards in global size. Shape consistency is measured through length, diameter, angle, and thickness consistency. Moreover, latent feature consistency and deformation percentage of vertex further evaluate the stability of the mesh in latent feature space and local vertex deformations.

### 8.2 Regularization

Regularization evaluation metrics assess the geometric quality and stability of the reconstructed mesh by analyzing properties such as smoothness, curvature, and topological integrity. These metrics ensure that the generated mesh is not only geometrically accurate but also free from irregularities that could affect its usability in clinical or computational applications.

#### 8.2.1 Smoothness

Smoothness evaluation focuses on detecting surface irregularities and self-intersections within the reconstructed mesh. Self-intersecting faces ratio and intersecting faces quantify the presence of overlapping or conflicting surface elements, which may indicate reconstruction errors. Additionally, the easy non-manifold face ratio identifies faces that violate manifold properties, highlighting issues related to mesh connectivity and structural integrity.

#### 8.2.2 Curvature

Curvature evaluation measures the local surface variations to ensure the smooth transition of the reconstructed mesh. Mean curvature and Gaussian curvature of the surface provide a mathematical representation of surface bending. Curvature of edge and distortion of edge assess the extent of local deviations, where distortion is typically measured by counting points where curvature exceeds a predefined threshold. Additionally, the tortuosity of vessel centerlines is used in vascular models to assess the complexity of vessel curvature and its potential implications on blood flow.

#### 8.2.3 Topology

Topology evaluation ensures that the mesh retains a correct and meaningful structural representation. Euler characteristic and genus index quantify the global topological properties of the mesh, determining whether it has the expected number of holes and connected components. Connected component analysis verifies that the reconstructed mesh remains a single coherent structure without unwanted disconnections. Furthermore, cap-wall orthogonality of face normals and cap coplanarity of face normals measure alignment consistency in structured regions. Additional assessments, such as discontinuity of edge and kernel density estimation of surface, help to identify abrupt structural changes

**Table 6. Evaluation Metrics of Medical Image-to-Mesh Reconstruction.**

Category	Evaluation Metrics	References
(1) Shape Similarity		
Distance	Chamfer Distance	Yuan et al. [2023] Chen et al. [2021] Lebrat et al. [2021] Ma et al. [2021] Wang et al. [2020b] Ye et al. [2023] Beetz et al. [2024] Beetz et al. [2021] Chen et al. [2024b] Chen et al. [2023] Zheng et al. [2023] Guven et al. [2024] Sun et al. [2022]
	Earth Mover Distance (EMD): Points	Yuan et al. [2023] Chen et al. [2021] Wang et al. [2020b] Ye et al. [2023] Cruz et al. [2021]
	Hausdorff Distance	Yuan et al. [2023] Govil et al. [2023] Chen et al. [2021] Nakao et al. [2021a] Tang et al. [2021] Beetz et al. [2022b] Beetz et al. [2022a] Kong and Shadden [2021] Lebrat et al. [2021] Hoopes et al. [2022] Ma et al. [2021] Rickmann et al. [2022] Zhao et al. [2022] Wang et al. [2020b] Kong and Shadden [2023] Bongratz et al. [2022] Bongratz et al. [2024] Zhao et al. [2023b] Nakao et al. [2021b] Geng et al. [2024] Xu et al. [2019] Ma et al. [2023] Chen et al. [2024b] Hong et al. [2021] Chen et al. [2023] Zheng et al. [2023] Cruz et al. [2021] Yeung et al. [2024] Meng et al. [2022a] Meng et al. [2024]
	Average Symmetric Surface Distance	Kong and Shadden [2021] Rickmann et al. [2022] Zhao et al. [2022] Bongratz et al. [2022] Bongratz et al. [2024] Zhao et al. [2023b] Ma et al. [2023]
	Mean Surface Distance	Xu and Elhabian [2023] Bhalodia et al. [2024] Aziz et al. [2023] Gilbert et al. [2020] Ruiz et al. [2018] Upendra et al. [2021a] Chen et al. [2021] Nakao et al. [2021a] Beetz et al. [2022b] Beetz et al. [2022a] Hoopes et al. [2022] Zhao et al. [2022] Tong et al. [2020] Maxime et al. [2022] Meng et al. [2022a] Meng et al. [2024] Ye et al. [2023] Bongratz et al. [2024] Nakao et al. [2021b] Krüger et al. [2024] Geng et al. [2024] Chen et al. [2024b] Banerjee et al. [2022] Geng et al. [2024] Zhao et al. [2022]
	Median Surface Distance	Beetz et al. [2022b] Batlle et al. [2023]
	Mean Squared Error	Romaszko et al. [2021] Tong et al. [2020] Wang et al. [2023b] Ruiz et al. [2018] Yeung et al. [2024]
	Mean Absolute Error	Govil et al. [2023] Upendra et al. [2021a] Nakao et al. [2021a] Tang et al. [2021] Ma et al. [2021] Batlle et al. [2023] Chen et al. [2023] Zheng et al. [2023] Cruz et al. [2021]
	Root Mean Squared Error	Bhalodia et al. [2024] Aziz et al. [2023] Batlle et al. [2023] Bongratz et al. [2024] Fernandes et al. [2012]
Consistency	Normal Vector Consistency (Cosine similarity/-/Dot)	Ye et al. [2023] Wang et al. [2023b] Geng et al. [2024] Guven et al. [2024] Sun et al. [2022]
	Dice Similarity Coefficient	Romaszko et al. [2021] Yuan et al. [2023] Gilbert et al. [2020] Govil et al. [2023] Govil et al. [2023] Nakao et al. [2021a] Kong and Shadden [2021] Hoopes et al. [2022] Rickmann et al. [2022] Zhao et al. [2022] Kong and Shadden [2023] Zhao et al. [2023b] Zhao et al. [2021] Nakao et al. [2021b] Geng et al. [2024] Xu et al. [2019] Ma et al. [2023] Chen et al. [2024b] Cruz et al. [2021] Yeung et al. [2024] Wang et al. [2020b] Guven et al. [2024] Meng et al. [2022a] Meng et al. [2024] Wang et al. [2020b] Krüger et al. [2024] Ma et al. [2023] Chen et al. [2024b] Guven et al. [2024]
	F-score	
	Intersection over Union	
	Confusion Matrix	Zhao et al. [2022] Govil et al. [2023] Chen et al. [2024b] Cruz et al. [2021]
	Structural Similarity Index Measure	Yeung et al. [2024]
	Volume Consistency	Banerjee et al. [2022] Chen et al. [2021] Beetz et al. [2022a] Kong and Shadden [2023] Beetz et al. [2024] Beetz et al. [2021] Ma et al. [2023] Romaszko et al. [2021]
	Surface Area Consistency	Ma et al. [2023] Hong et al. [2021]
	Length / Diameter / Angel / Thickness Consistency	Krüger et al. [2024] Bongratz et al. [2022] Ma et al. [2023] Zhao et al. [2021]
	Latent Feature Consistency	Maxime et al. [2022] Gilbert et al. [2020]
	Deformation Percentage of Vertex	Maxime et al. [2022]
(2) Geometry Regularization		
Smoothness	Self-Intersecting Faces Ratio	Lebrat et al. [2021] Kong and Shadden [2023] Ye et al. [2023] Sun et al. [2022]
	Intersecting Faces	Hoopes et al. [2022] Bongratz et al. [2024] Ma et al. [2023]
	Easy Non-Manifold Face Ratio	Ye et al. [2023] Sun et al. [2022]
Curvature	Mean Curvature	Hong et al. [2021] Tang et al. [2021]
	Gaussian Curvature of Surface	Chen et al. [2024b]
	Curvature of Edge	Song et al. [2022]
	Distortion of Edge (Counts points where curvature > threshold)	Song et al. [2022]
	Tortuosity of Vessel Centerline	Krüger et al. [2024]
Topology	Euler Characteristic	Zhao et al. [2023b] Xu et al. [2019] Ma et al. [2023]
	Connected Components	Chen et al. [2024b]
	Genus Index	Chen et al. [2024b]
	Cap-Wall Orthogonality of face normals	Kong and Shadden [2023]
	Cap coplanarity of face normals	Kong and Shadden [2023]
	Discontinuity of Edge	Song et al. [2022]
	Kernel Density Estimation of Surface	Chen et al. [2024b]
(3) Functional Evaluation		
Clinical Function	Ejection Fraction	Beetz et al. [2022a] Beetz et al. [2024]
	Accuracy of Disease Prediction	Bhalodia et al. [2024] Romaszko et al. [2021] Beetz et al. [2024]
	Accuracy of Vertex Classification	Krüger et al. [2024] Tang et al. [2021] Beetz et al. [2024]
CFD Simulation	Velocity	Krüger et al. [2024] Kong and Shadden [2023]
	Average Kinetic Energy	Kong and Shadden [2023]
Efficiency	Inference Time	Bongratz et al. [2022] Beetz et al. [2021]

or anomalies that could affect downstream computational simulations.

### 8.3 Functional Evaluation

Functional evaluation metrics assess the practical utility and computational feasibility of the reconstructed mesh, ensuring that it is suitable for clinical applications and physics-based computational simulations. These metrics encompass clinical function analysis, computational simulation accuracy, and processing efficiency.

#### 8.3.1 Clinical Function

Clinical function metrics evaluate the ability of the reconstructed mesh to provide meaningful physiological and diagnostic insights. Ejection fraction is a key cardiac function metric that measures the heart’s pumping efficiency. Additionally, accuracy of disease prediction assesses the model’s capability to classify pathological conditions based on mesh-derived features. Accuracy of vertex classification is used to validate the correctness of anatomical structure identification within the mesh.

#### 8.3.2 CFD Simulation Metrics

Computational fluid dynamics (CFD) simulation metrics measure how well the reconstructed mesh supports hemodynamic analysis. Velocity quantifies the flow speed of blood within the modeled structure, while average kinetic energy represents the energy distribution across the fluid domain. These metrics are crucial for evaluating blood flow dynamics and assessing cardiovascular conditions.

#### 8.3.3 Efficiency

Efficiency metrics measure the computational cost and practicality of the reconstruction process. Inference time evaluates the speed at which the mesh is generated, ensuring that the model can provide real-time or near-real-time outputs suitable for clinical and research applications.

## 9 Datasets for Medical Image-to-Mesh Reconstruction

Medical image-to-mesh reconstruction plays a crucial role in various clinical and computational applications, including anatomical modelling, surgical planning, and biomechanical simulations. The availability of well-annotated datasets enables the development and evaluation of deep learning methods for accurate and efficient 3D mesh reconstruction. In this section, we summarize publicly available datasets that provide volumetric medical images

alongside segmentation masks or surface meshes, categorized by organ type and imaging modality. A comprehensive overview of these datasets is presented in Table 7.

### 9.1 Cardiac Datasets

Cardiac image-to-mesh reconstruction is critical for applications such as computational simulations, cardiac disease diagnosis, and biomechanical modelling. Several datasets offer segmentation masks and mesh representations derived from CMR, CT, and echocardiography imaging.

UK Biobank [Petersen et al. \[2016\]](#) provides a large-scale dataset with 50,000 CMR scans and corresponding segmentation masks, enabling statistical shape modelling and population-based analysis. ACDC [Bernard et al. \[2018\]](#) contains CMR sequences from 100 patients categorized into five pathological conditions, facilitating supervised segmentation and mesh reconstruction tasks. MMWHS [Zhuang and Shen \[2016\]](#) includes multimodal cardiac imaging (MR and CT) with segmentation and surface mesh annotations, supporting cross-modality learning. OrCaScore [Wolterink et al. \[2016\]](#) provides 3D CT volumes with coronary artery calcification (CAC) segmentation for automated assessment. 4D SSM [Unberath et al. \[2015\]](#) contains dynamic heart meshes extracted from CTA data, supporting motion analysis in cardiac studies. EchoNet-Dynamic [Ouyang et al. \[2020\]](#) offers echocardiographic imaging (ECGI) videos with segmentation and measurement annotations, facilitating deep learning-based cardiac function assessment. These datasets provide valuable resources for advancing automated cardiac mesh reconstruction, simulation, and motion tracking.

### 9.2 Brain Datasets

Brain surface reconstruction is essential for neuroimaging, particularly in cortical thickness estimation, structural analysis, and neurological disorder diagnosis. Several datasets provide volumetric MR images along with FreeSurfer-generated surface meshes.

ADNI [Jack Jr. et al. \[2008\]](#) and J-ADNI [Iwatsubo \[2010\]](#) provide large-scale T1-weighted MR brain scans with FreeSurfer meshes, enabling research on Alzheimer’s disease progression. OASIS [Marcus et al. \[2007\]](#) consists of 3D T1-MR brain volumes with segmentation and mesh annotations across healthy and pathological cases. Test-Retest (TRT) [Maclaren et al. \[2014\]](#) and Mindboggle [Klein and Tourville \[2012\]](#) contain repeated MR scans for evaluating the reproducibility of neuroimaging pipelines. NAMIC [Desikan et al. \[2006\]](#) provides brain surface meshes with gyrus-based regional labels, supporting brain morphology analysis. These datasets enable deep learning-based cortical surface modelling, anatomical segmentation, and brain

shape analysis.

### 9.3 Thoracic and Abdominal Datasets

Reconstruction of the lungs, liver, and other thoracic organs from medical images is crucial for applications such as respiratory motion modelling and tumor detection. Several datasets focus on these regions.

4D-Lung Dataset [Hugo et al. \[2017\]](#) and 4D-Liver Dataset (Kitware) [Kitware \[2024\]](#) provide 4D CT volumes with segmentation-based mesh annotations, enabling motion tracking and organ modelling. SegTHOR [Trullo et al. \[2019\]](#) contains thoracic organ segmentation data from 3D CT volumes, supporting automated mesh reconstruction for lung and heart structures. Pancreas-CT [Roth et al. \[2016\]](#) provides segmentation masks for pancreas segmentation and potential mesh extraction. These datasets facilitate the development of AI-driven solutions for 3D thoracic and abdominal organ reconstruction.

### 9.4 Skull and Musculoskeletal Datasets

Bone and skull reconstruction from medical imaging is essential for forensic analysis, orthopedic applications, and implant design. Several datasets focus on these aspects.

SkullFix/SkullBreak [Kodym et al. \[2021\]](#) provides defective skull masks and their corresponding reconstructed meshes, supporting research in cranial defect restoration. MUG500+ [Li et al. \[2021\]](#) offers CT-based skull images with mesh annotations for reconstructive surgery applications. These datasets support automated skull reconstruction, defect analysis, and clinical decision-making.

### 9.5 Endoscopic and Multimodal Datasets

Endoscopic imaging and multimodal datasets provide diverse anatomical structures, enabling generalized deep learning approaches for image-to-mesh reconstruction.

C3VD [Bobrow et al. \[2023\]](#) provides endoscopic video sequences with camera pose annotations and ground-truth 3D meshes for colon surface reconstruction. EndoMapper [Azagra et al. \[2023\]](#) offers calibration data for endoscopic imaging, including light source and vignetting calibration. NLST [Hofmanninger et al. \[2020\]](#) provides lung CT volumes and digitally reconstructed radiographs (DRRs) with 3D mesh annotations. INTERGROWTH-21st [Papageorghiou et al. \[2014\]](#) contains fetal brain ultrasound scans with atlas-based alignment annotations, supporting prenatal imaging studies. These datasets enhance AI-driven surface reconstruction by incorporating diverse imaging techniques and anatomical structures.

## 9.6 Summary

Medical image-to-mesh datasets provide essential resources for training and evaluating deep learning-based surface reconstruction methods. As highlighted in Table 7, these datasets span multiple organs, imaging modalities, and annotation types, offering challenges and opportunities for model generalization. By leveraging these datasets, researchers can advance medical image-to-mesh reconstruction techniques, leading to more accurate and efficient 3D anatomical modelling for clinical applications.

## 10 Meta Analysis

We conducted a meta-analysis to evaluate the performance of template models, statistical shape models, generative models, and implicit models on cardiac MR and cortical MR datasets. The analysis was carried out following clinical principles [Julian et al. \[2019\]](#), adhering to a study-based statistical approach. Specifically, only studies targeting the same medical objective and employing the same imaging modality were included in the analysis to ensure consistency and comparability.

The performance of template models, statistical shape models, and generative models on the cardiac dataset was analyzed based on Dice similarity coefficient and Hausdorff distance, as shown in Fig. 21. For Dice similarity (%), higher values indicate better shape reconstruction accuracy. The generative model achieved a higher median Dice score than the statistical shape model and the template model. For Hausdorff distance (mm), lower values indicate better geometric accuracy. The generative model demonstrated the lowest median Hausdorff distance, followed closely by the statistical shape model. The template model showed the highest Hausdorff distance. Overall, the generative model achieved the best performance among the three, outperforming both the statistical shape model and the template model in terms of shape accuracy and geometric consistency. The statistical shape model performed better than the template model but was still inferior to the generative model.

The performance of template models, generative models, and implicit models in the cortical dataset was analysed using four evaluation metrics: Average Distance, Chamfer Distance, Hausdorff Distance, and Average Symmetric Surface Distance, as shown in Fig. 20. Lower values across all metrics indicate better reconstruction accuracy. For average distance, the implicit model demonstrated the lowest values across both pial and white matter surfaces, indicating superior geometric accuracy. The generative model followed closely, achieving better results than the template model. For Chamfer distance, the implicit model outperformed the generative model and template model. The implicit model



**Table 7. Public Datasets of Medical Image-to-Mesh Reconstruction.**

Name Download Link	Reference	Modality	Organ	Data Type	Annotations	Sample Size
UK Biobank	Petersen et al. [2016]	MR	Heart	3D Volume	Segmentation	50000
ACDC	Bernard et al. [2018]	CMR	Heart	CMR sequences	Segmentation	100 patients in five categories
MMWHS	Zhuang and Shen [2016]	CT, MR	Heart	3D Volume	Segmentation, Surface Mesh	142 CT, 87 MR
OrCaScore	Wolterink et al. [2016]	CT	Heart	3D Volume	Coronary artery calcification (CAC) segmentation	72
SLAWT	Karim et al. [2018]	CT, MR	Left Atrium	Image	Wall Segmentation	10 CT, 10 MR
LASC	Tobon-Gomez et al. [2015]	CT, MR	Left Atrium	Image	Segmentations	30 CT, 30 MR
4D myocardial dataset	Romaszko et al. [2021]	CMR	Left myocardium	2D CMR slices (8-10 slices, 25 phases)	Manual delineation of left myocardium	55 healthy subjects
Cardiac SSM	Bai et al. [2015]	CMR	Bi-ventricle	2D SAX+LAX slices	HR/LR masks	1,331 (ED+ES)
CAP Database	Fonseca et al. [2011]	CMR	Heart	2D Images	Contours, Landmarks	153 (123+30)
MESA	Bild et al. [2002]	MR	Heart	3D volume	Segmentation, Mesh	1,991
M&Ms-2 Challenge	Campello et al. [2021]	MR	Heart	2D Images (SAX+LAX)	Segmentation	160 training + 40 validation
ADNI	Jack Jr. et al. [2008]	MR T1	Brain	3D Volume	FreeSurfer Mesh	1647
J-ADNI	Iwatsubo [2010]	MR T1	Brain	3D Volume	FreeSurfer Mesh	502 (145 HC, 218 MCI, 139 AD)
OASIS	Marcus et al. [2007]	MR T1	Brain	3D Volume	FreeSurfer Mesh	416 (292/44/80)
Yale TRT)	Maclaren et al. [2014]	MR T1	Brain	3D Volume	FreeSurfer Mesh	120 (3 subjects x 20 days x 2 scans)
MALC	Landman and Warfield [2012]	MR T1	Brain	3D Volume	FreeSurfer Mesh	30
Mindboggle	Klein and Tourville [2012]	MR T1	Brain	3D Volume	FreeSurfer Mesh	100
JHU Cortex	Shree et al. [2014]	MR T1	Brain	3D Volume	Manual Landmarks	10 (5 HC, 5 MS)
dHCP	Hughes et al. [2017]	MR T2w	Brain	3D Volume	Segmentation, Surface Meshes	874
HCP	Van Essen et al. [2013]	MR T1w	Brain	3D Volume	Segmentation, Surface Meshes	600
NAMIC	Desikan et al. [2006]	MR	Brain	Surface Mesh	Region Labels (35 gyrus-based regions)	39 subjects
Infant Brain	Li et al. [2015]	MR	Brain	Spherical Surface Mesh	Sulcal depth, Mean curvature, Thickness	90 (parcellation), 370 (thickness prediction)
4D-Lung	Hugo et al. [2017]	CT	Lung	4D CT volumes	Mesh (nnU-Net segmentation)	20 cases (200 3D scans)
4D-Liver (Kitware)	Kitware [2024]	CT	Liver	4D CT volumes	Mesh (nnU-Net segmentation)	5 cases (50 3D scans)
muRegPro	Baum et al. [2023]	TRUS	Prostate	3D volume	Anatomical landmarks, Prostate gland, Visible lesions	73 (65 training + 8 validation)
C3VD	Bobrow et al. [2023]	Endoscopy	Colon	Video sequences	Camera poses, Ground truth 3D mesh	22 sequences
EndoMapper	Azagra et al. [2023]	Endoscopy	Colon	Calibration data	Light source, Vignetting calibration	Not specified
NLST	Hofmanninger et al. [2020]	CT, DRR	Lung	CT Volume + X-ray	3D Mesh	6,392 CT scans (2,560 subjects)
INTERGROWTH-21st	Papageorgiou et al. [2014]	Ultrasound	Fetal Brain	3D volumes	Atlas alignment	15
IXI	Dataset [2021]	MR	Brain	3D Volume	Surface Mesh	158
MCIC	Gollub et al. [2013]	MR	Brain	3D Volume	Surface Mesh	76
Buckner40	Fischl et al. [2002]	MR	Brain	3D Volume	Surface Mesh	40
SegTHOR	Trullo et al. [2019]	CT	Thoracic Organs	3D Volume	Segmentation	40
DIR-Lab	Castillo et al. [2009]	CT	Lungs	4D-CT	CT scans	10
JSRT	Shiraishi et al. [2000]	X-ray	Chest	2D images	X-ray images	247
Pancreas-CT	Roth et al. [2016]	CT	Pancreas	3D volume	Segmentation	Not specified
4D SSM	Unberath et al. [2015]	CTA	Heart	3D volume	Dynamic Mesh	20
SPUM-ACS	Klingenberg et al. [2015]	US-TTE	Heart	2D Video	Segmentation	314 (Acute Myocardial Infarction)
CCT48	Sunnesiaputra et al. [2018]	CT	Heart	3D volume	Segmentation	48
MITEA	Zhao et al. [2023a]	US	Heart	3D volume	Segmentation	536
MSD liver	Simpson et al. [2019]	CT	Liver	3D volume	Segmentation	131
EchoNet-Dynamic	Ouyang et al. [2020]	ECGI videos	Heart	3D Volume	Segmentation, Measurement	10030
SkullFix/SkullBreak	Kodym et al. [2021]	Binary Mask	Skull	Defective Mask	Reconstructed Mask	670
MUG500+	Li et al. [2021]	CT	Skull	3D Volume	Surface Mesh	529
SHAPR	Waibel et al. [2022]	Microscopy	Cell	Single 2D Image	Surface Mesh	825
Red Blood Cell	Simionato et al. [2021]	Microscopy	Cell	Single 2D Image	Surface Mesh	2000 cells

generally had the lowest values, indicating better alignment with ground truth surfaces. For Hausdorff distance, the implicit model achieved the lowest values across all anatomical regions, confirming its advantage in maintaining fine structural details. The template model performed moderately well. For average symmetric surface distance, the implicit model again exhibited lower values than the template model, reinforcing its superiority in shape reconstruction. Overall, the implicit model demonstrated the best reconstruction accuracy across all metrics, followed by the generative model and template model.

Overall, the results indicate that the implicit model consistently outperforms the other approaches across multiple datasets and evaluation metrics. On the cortical dataset, the implicit model demonstrated superior geometric accuracy, achieving the lowest error across all four evaluation metrics. The generative model followed, showing better performance than the template model. On the cardiac dataset, where statistical shape models were included and implicit models were excluded, the generative model achieved the highest accuracy, outperforming both statistical shape models and template models.

Considering the results from both the cardiac and cortical datasets, the ranking follows the order: implicit model > generative model > statistical shape model > template model. This ranking is relative rather than absolute, as different methods may still achieve the best performance on specific datasets or under certain conditions. The effectiveness of each approach can vary depending on factors such as anatomical structures, data quality, and task-specific requirements. This trend highlights the increasing effectiveness of data-driven approaches, with implicit and generative models consistently surpassing traditional statistical and template-based methods. The statistical shape model serves as an intermediate solution between generative and template models in certain medical applications, but its performance remains inferior to more advanced deep-learning-based approaches.

## 11 Discussion

Figure 22 systematically illustrates how different methods address key challenges in the process of medical image-to-mesh reconstruction, highlighting the suitability and strengths of various models for complex tasks. The entire framework is divided into three levels, linking challenges and requirements to core objectives and ultimately to specific method categories, creating a clear path that connects needs with solutions.

Medical image-to-mesh reconstruction faces multiple challenges, one of which is the strict topological requirements. This often involves generating meshes with fixed topology, ensuring stability and the absence of topological

errors during complex anatomical simulations. Additionally, achieving accurate simulations often necessitates high geometric accuracy, ensuring that meshes reflect anatomical details with precision, providing a solid foundation for calculations and simulations. Another critical challenge is multi-modality integration, which seeks to fuse data from different imaging modalities (such as CT, MRI, and ultrasound) to produce dynamic meshes that are more realistic and anatomically consistent.

To address these challenges, different methods are designed to achieve various core objectives. For instance, methods aimed at meeting topological requirements focus on ensuring fixed topology or handling complex topological variations to accommodate anatomical differences across individuals. Smoothness is essential for generating continuous mesh surfaces, preventing discontinuities or surface irregularities. In pursuit of high geometric accuracy, methods must be capable of capturing fine details to preserve subtle anatomical features, while also improving robustness to noisy data to mitigate the effects of imaging artifacts or missing data. Generating high-resolution meshes is another critical goal, especially for reconstructing complex anatomical regions. In the context of multi-modality imaging, models must not only reconstruct dynamic shapes but also possess the ability to fuse multi-modal data to ensure consistent mesh reconstruction under different imaging conditions.

Four primary methods play distinct roles in achieving these objectives, each offering unique strengths and applicability. Deformation models progressively adjust an initial template mesh to fit the target shape, making them particularly suitable for tasks with strict topological constraints, where fixed or predictable topology is essential. Statistical shape models rely on large anatomical datasets and employ statistical techniques to model shape variations, ensuring smooth surfaces and maintaining topological consistency. In contrast, generative models synthesize meshes directly from input images, capturing intricate details while maintaining robustness to noise and missing data. Implicit models, on the other hand, represent mesh surfaces through learned implicit functions, enabling the generation of high-resolution and complex topological meshes. These models excel at reconstructing dynamic shapes and integrating multi-modal data, making them ideal for highly intricate anatomical structures.

The complementary nature of different methods in addressing various challenges and objectives allows for the selection of the most suitable reconstruction techniques based on specific applications. Combining multiple approaches can further enhance the accuracy and stability of the final mesh, providing critical support for medical research and simulations.

Table 10 presents a comprehensive comparison of different models used in medical image-to-mesh reconstruction.

**Table 8. Performance comparison of methods on Cardiac datasets.**

Metric	Method	Taxonomy	Cardiac MR				
			Myo	LA	LV	RA	RV
Dice (%) $\uparrow$	MeshDeformNet Kong et al. [2021]	T - Deformation	79.71	88.13	92.23	89.24	89.24
	HeartFFDNet Kong and Shadden [2021]	T - Deformation	70.67	83.27	86.92	82.77	82.77
	HeartDeformNet Kong and Shadden [2023]	T - Deformation	78.62	86.27	89.38	87.79	87.20
	FFD-SEG Rueckert et al. [1999]	T - Registration					75.47
	Dem-SEG Yaniv et al. [2018]	T - Registration					79.49
	CNN-SEG Upendra et al. [2021b]	T - Registration					79.51
	Dem-CNN Upendra et al. [2021a]	T - Registration					84.91
	Attar et al. [2019b]	S - Linear SSM	92.00		91.00		88.00
	Attar et al. [2019a]	S - Linear SSM	93.00		90.00		90.00
	MCSI-Net Xia et al. [2022]	S - Linear SSM	78.00	88.00	88.00	88.00	85.00
	MV-HybridVNet Gaggion et al. [2024]	G - VAE	84.00		91.00		87.00
	Xu et al. [2019]	G - Interpolation	83.00		95.00		93.00
	MeshDeformNet Kong and Shadden [2021]	T - Deformation	18.21	12.43	12.57	16.36	16.36
	HeartFFDNet Kong and Shadden [2023]	T - Deformation	15.96	10.16	8.97	12.46	12.46
Hausdorff (mm) $\downarrow$	MeshDeformNet Kong et al. [2021]	T - Deformation	16.92	12.22	11.63	14.73	14.73
	Pixel2mesh Wang et al. [2020a]	T - Deformation		16.20			16.20
	Mesh Deformation U-Net Beetz et al. [2022b]	T - Deformation			4.69		4.77
	CPD Myronenko and Song [2010]	T - Registration		13.05			13.05
	GMMREG Jian and Vemuri [2010]	T - Registration		15.87			15.87
	FFD Rueckert et al. [1999]	T - Registration	10.31		10.31		
	dDemons Vercauteren et al. [2007]	T - Registration	9.71		9.71		
	MulViMotion Meng et al. [2022b]	T - Registration	9.86		9.86		
	MeshMotion Meng et al. [2022a]	T - Registration	9.73		9.73		
	DeepMesh Meng et al. [2024]	T - Registration	9.08		9.08		
	MR-Net Chen et al. [2021]	T - Registration		6.89			6.89
	Attar et al. [2019b]	S - Linear SSM	3.32		3.76		8.32
	Attar et al. [2019a]	S - Linear SSM	3.55		3.11		7.05
	MCSI-Net Xia et al. [2022]	S - Linear SSM	4.75	6.82	4.74	7.34	7.06
	Xu et al. [2019]	G - Interpolation	6.30		4.94		5.91
	MV-HybridVNet Gaggion et al. [2024]	G - VAE	3.96		3.89		6.13
Chamfer (mm) $\downarrow$	MR-Net Chen et al. [2021]	T - Deformation		4.39	2.73		4.39
	Ye et al. [2023]	T - Deformation			2.32		
	MCSI-Net Xia et al. [2022]	S - Linear SSM	1.86	2.65	1.86	2.79	2.27
	MV-HybridVNet Gaggion et al. [2024]	G - VAE	1.35		1.39		1.76
Mean Dist. (mm) $\downarrow$	Mesh Deformation U-Net Beetz et al. [2022b]	T - Deformation			0.98		1.25
	Ye et al. [2023]	T - Deformation			1.02		
	FFD Rueckert et al. [1999]	T - Registration	3.02		3.02		
	dDemons Vercauteren et al. [2007]	T - Registration	3.20		3.20		
	MulViMotion Meng et al. [2022b]	T - Registration	2.39		2.39		
	MeshMotion Meng et al. [2022a]	T - Registration	1.98		1.98		
	DeepMesh Meng et al. [2024]	T - Registration	1.66		1.66		
	FFD-SEG Rueckert et al. [1999]	T - Registration					4.37
	Dem-SEG Yaniv et al. [2018]	T - Registration					3.52
	CNN-SEG Upendra et al. [2021b]	T - Registration					3.34
	Dem-CNN Upendra et al. [2021a]	T - Registration					1.08
	MR-Net Chen et al. [2021]	T - Registration			1.35		
	Attar et al. [2019b]	S - Linear SSM	1.80		1.85		2.02
	Attar et al. [2019a]	S - Linear SSM	1.82		1.81		2.00

**Table 9. Performance comparison of image to mesh reconstruction methods on Brain MR dataset.**

Metric	Method	Taxonomy	Brain MR			
			Left Pial	Right Pial	Left WM	Right WM
Mean Dist. (mm) ↓	TopoFit <a href="#">Hoopes et al. [2022]</a>	T - Deformation			0.13	0.13
	Voxel2Mesh <a href="#">Wickramasinghe et al. [2020]</a>	T - Deformation	0.34	0.31		
	<a href="#">Rickmann et al. [2022]</a>	T - Deformation	0.35	0.35	0.32	0.32
	Vox2Cortex <a href="#">Bongratz et al. [2022]</a>	T - Deformation	0.34	0.34	0.28	0.28
	PialNN <a href="#">Ma et al. [2021]</a>	T - Deformation	0.52	0.49	0.19	0.19
	<a href="#">Hu et al. [2021]</a>	G - GAN	0.32	0.32		
	<a href="#">Hu et al. [2022]</a>	G - VAE	0.25	0.25		
	PointOutNet <a href="#">Zhou et al. [2019]</a>	G - VAE	0.41	0.41		
	SurfNN <a href="#">Zheng et al. [2023]</a>	I - SDF	0.23	0.23	0.14	0.14
	DeepCSR (SDF) <a href="#">Cruz et al. [2021]</a>	I - SDF	0.30	0.29	0.27	0.26
	CortexODE <a href="#">Ma et al. [2023]</a>	I - Neural ODE	0.20	0.20	0.19	0.19
	CorticalFlow <a href="#">Santa Cruz et al. [2022]</a>	I - Neural ODE	0.30	0.30	0.24	0.24
	DeepCSR (Occ.) <a href="#">Cruz et al. [2021]</a>	I - Occupancy	0.31	0.31	0.28	0.29
	Voxel2Mesh <a href="#">Wickramasinghe et al. [2020]</a>	T - Deformation	0.82	0.80	1.21	1.19
	Vox2Cortex <a href="#">Bongratz et al. [2022]</a>	T - Deformation	0.97	1.01	0.89	0.90
Hausdorff (mm) ↓	<a href="#">Rickmann et al. [2022]</a>	T - Deformation	0.85	0.85	0.78	0.78
	TopoFit <a href="#">Hoopes et al. [2022]</a>	T - Deformation	0.49	0.56	0.47	0.48
	PialNN <a href="#">Ma et al. [2021]</a>	T - Deformation	0.44	0.44	0.42	0.42
	V2C-Flow <a href="#">Bongratz et al. [2024]</a>	I - Neural ODE	0.40	0.39	0.39	0.39
	CorticalFlow <a href="#">Lebrat et al. [2021]</a>	I - Neural ODE	0.52	0.52	0.48	0.48
	CF++ <a href="#">Santa Cruz et al. [2022]</a>	I - Neural ODE	0.38	0.38	0.40	0.40
	CortexODE <a href="#">Ma et al. [2023]</a>	I - Neural ODE	0.43	0.42	0.41	0.42
	DeepCSR (SDF) <a href="#">Cruz et al. [2021]</a>	I - SDF	0.65	0.65	0.56	0.54
	Vox2surf <a href="#">Hong et al. [2021]</a>	I - SDF	0.82	0.82	0.64	0.64
	SurfNN <a href="#">Zheng et al. [2023]</a>	I - SDF	0.52	0.52	0.31	0.30
	DeepCSR (Occ.) <a href="#">Cruz et al. [2021]</a>	I - Occupancy	0.71	0.67	0.58	0.58
Dice (%) ↑	TopoFit <a href="#">Hoopes et al. [2022]</a>	T - Deformation			97.60	97.60
	<a href="#">Rickmann et al. [2022]</a>	T - Deformation	87.70	87.70	90.40	90.40
	Vox2Cortex <a href="#">Bongratz et al. [2022]</a>	T - Deformation	69.10	69.10	74.00	74.00
	Voxel2Mesh <a href="#">Wickramasinghe et al. [2020]</a>	T - Deformation	89.60	88.80	85.00	84.20
	CorticalFlow <a href="#">Lebrat et al. [2021]</a>	I - Neural ODE	97.70	97.60	96.20	96.20
	NMF <a href="#">Gupta [2020]</a>	I - Neural ODE	95.30	94.60	92.80	92.70
	DeepCSR <a href="#">Cruz et al. [2021]</a>	I - SDF	98.10	98.10	96.30	96.40
Chamfer (mm) ↓	Voxel2Mesh <a href="#">Wickramasinghe et al. [2020]</a>	T - Deformation	0.58	0.57		
	PialNN <a href="#">Ma et al. [2021]</a>	T - Deformation	0.68	0.65		
	<a href="#">Hu et al. [2021]</a>	G - GAN	0.96	0.96		
	<a href="#">Hu et al. [2024]</a>	G - GAN	0.44	0.45		
	<a href="#">Hu et al. [2022]</a>	G - VAE	0.68	0.69		
	TopNet <a href="#">Tchapmi et al. [2019]</a>	G - VAE	0.63	0.63		
	FoldingNet <a href="#">Yang et al. [2018]</a>	G - VAE	0.99	0.99		
	PointOutNet <a href="#">Zhou et al. [2019]</a>	G - VAE	0.55	0.55		
	CortexODE <a href="#">Ma et al. [2023]</a>	I - Neural ODE	0.45	0.46	0.44	0.44
	DeepCSR <a href="#">Cruz et al. [2021]</a>	I - SDF	0.99	1.01	0.98	1.00
	SurfNN <a href="#">Zheng et al. [2023]</a>	I - SDF	0.41	0.41	0.29	0.29
ASSD (mm) ↓	TopoFit <a href="#">Hoopes et al. [2022]</a>	T - Deformation	0.22	0.25	0.21	0.21
	Voxel2Mesh <a href="#">Wickramasinghe et al. [2020]</a>	T - Deformation	0.49	0.48	0.53	0.53
	Vox2Cortex <a href="#">Bongratz et al. [2022]</a>	T - Deformation	0.38	0.38	0.40	0.40
	PialNN <a href="#">Ma et al. [2021]</a>	T - Deformation	0.21	0.21	0.19	0.19
	V2C-Flow <a href="#">Bongratz et al. [2024]</a>	I - Neural ODE	0.18	0.17	0.18	0.18
	CorticalFlow <a href="#">Lebrat et al. [2021]</a>	I - Neural ODE	0.22	0.22	0.21	0.21
	CF++ <a href="#">Santa Cruz et al. [2022]</a>	I - Neural ODE	0.17	0.17	0.18	0.18
	DeepCSR <a href="#">Cruz et al. [2021]</a>	I - Neural ODE	0.45	0.42	0.42	0.42
	CortexODE <a href="#">Ma et al. [2023]</a>	I - Neural ODE	0.18	0.19	0.17	0.17

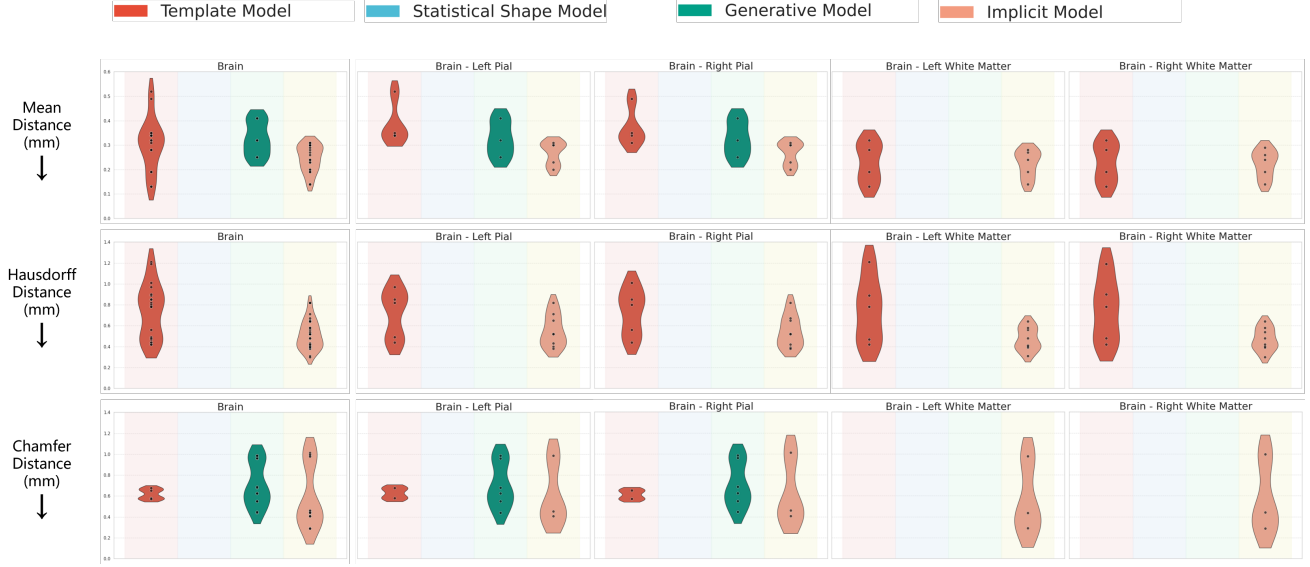


**Figure 20. Quantitative results comparison on the brain MR dataset.** Our data is from the same modality and the same anatomy, making it comparable across different studies according to clinical standards. The first column on the left displays reconstruction results on the brain MR dataset (whole structure). The columns to the right show reconstruction results for various brain substructures (left and right pial, left and right white matter). Different colours represent different model categories.  $\uparrow$  indicates that a higher value is better, while  $\downarrow$  indicates that a lower value is better. From the results, it can be seen that there is no absolute superiority or inferiority between the methods, but the overall robustness of each method can be observed in their distribution.

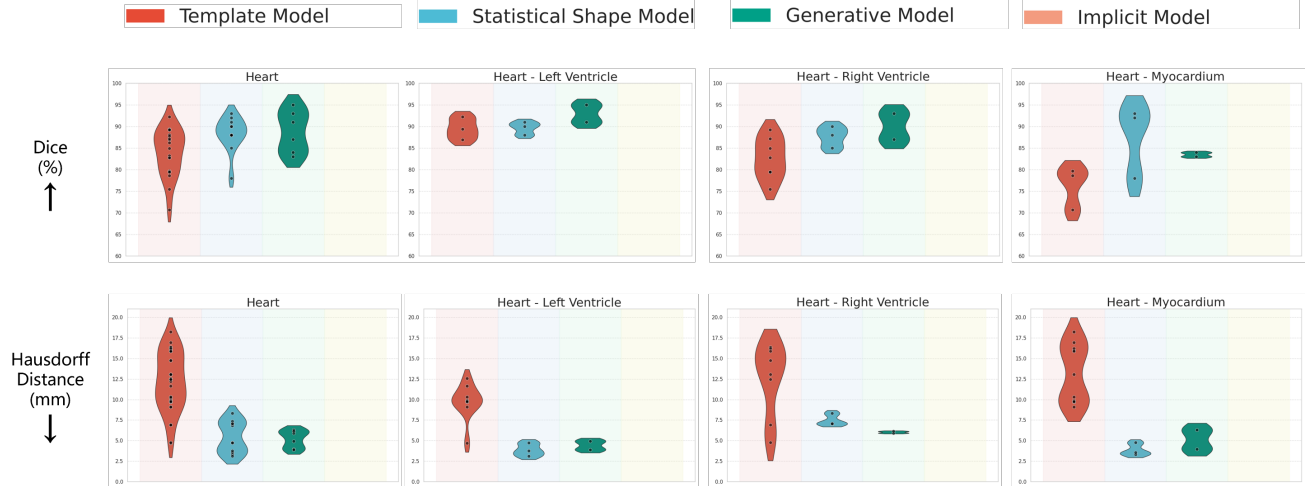


**Figure 21. Quantitative results comparison on the Cardiac MR Dataset.** The first column on the left displays reconstruction results on the cardiac MR dataset (whole heart, include substructures on the right). The columns to the right show reconstruction results for various heart substructures (left ventricle, right ventricle, and myocardium). Different colours represent different model categories.  $\uparrow$  indicates that a higher value is better, while  $\downarrow$  indicates that a lower value is better.



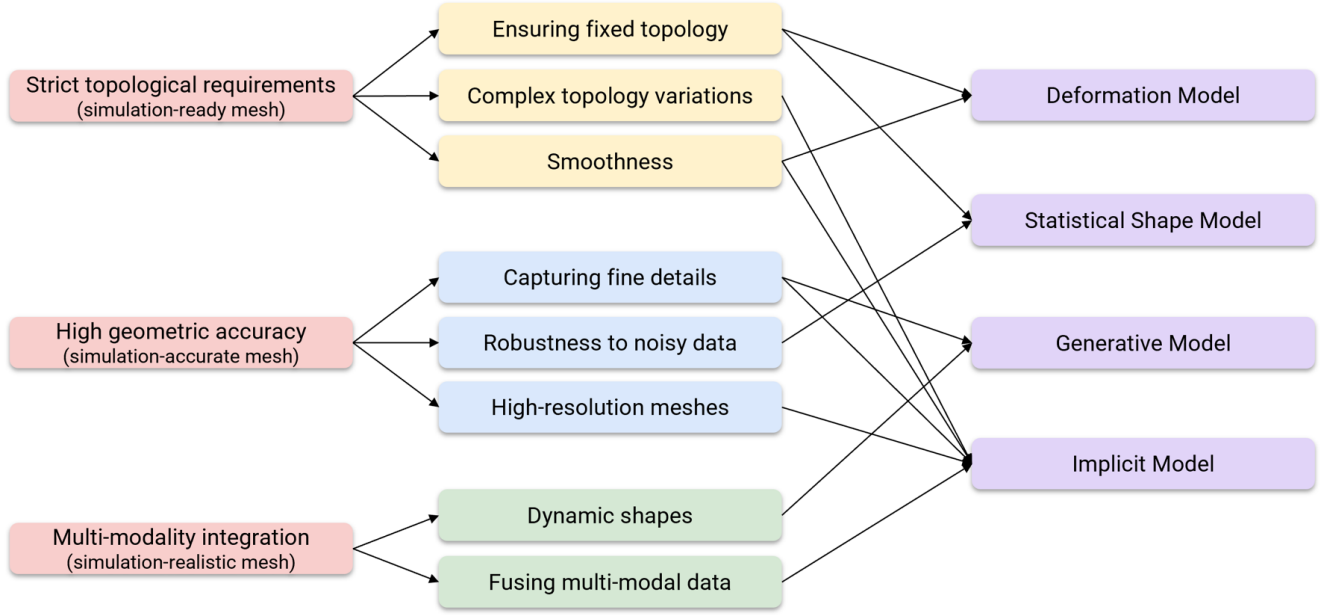


**Figure 22. Challenges of Medical Image-to-Mesh Reconstruction.**

**Table 10. Comparison of different models for medical image-to-mesh reconstruction.**

Model	Advantages	Disadvantages	Applicable Scenarios
Deformation Model	Controlled topology Easy to optimize	Strong dependence on templates Not suitable for complex topology	Fixed topology shape reconstruction (Example: generating normal cardiac meshes)
Statistical Shape Model	Strong shape priors Robust to noise	Strong dependence on training data Limited detail representation	Scenarios requiring statistical regularities (Example: reconstruction of typical cardiac anatomy)
Generative Model	Adaptable to diverse shapes Detailed representation	Complex training High data requirement	Personalized mesh generation (Example: pathological or abnormal shapes)
Implicit Model	Flexible topology High resolution	Complex training and optimization	Irregular surfaces or complex topologies (Example: modelling fine details around cardiac valves)

tion, outlining their respective advantages, disadvantages, and applicable scenarios. This structured overview provides valuable insights into the strengths and limitations of each approach, guiding the selection of appropriate methods based on specific reconstruction requirements.

The deformation model stands out for its ability to control topology, making it easy to optimize. This model is particularly well-suited for tasks that require fixed topology shape reconstruction, such as generating normal cardiac meshes. However, its strong dependence on templates and limited adaptability to complex topologies can restrict its application in more intricate anatomical structures. While it provides stable and controlled results, its inability to handle highly irregular surfaces may necessitate complementary methods for complex reconstructions.

The statistical shape model leverages strong shape priors, offering robustness to noise and ensuring consistency across different datasets. This makes it particularly useful for scenarios that demand statistical regularities, such as reconstructing typical cardiac anatomy. Nevertheless, the model's reliance on extensive training data and its limited

ability to represent fine details pose notable challenges. Despite these limitations, its ability to enforce anatomical constraints makes it an essential tool for applications that prioritize structural consistency over intricate detail.

Generative models provide a high degree of adaptability, capable of representing diverse shapes with detailed accuracy. This model excels in personalized mesh generation, particularly for pathological or abnormal shapes where standard templates may not suffice. The ability to synthesize complex geometries makes it highly valuable in cases requiring detailed, patient-specific reconstructions. However, generative models are often associated with complex training processes and significant data requirements, which can limit their accessibility and scalability in resource-constrained environments.

Implicit models offer unmatched flexibility in topology and enable high-resolution mesh reconstruction. They are particularly advantageous in handling irregular surfaces or complex topologies, such as modelling fine anatomical details around cardiac valves. Despite their potential to generate intricate and detailed meshes, implicit models come

with the challenge of complex training and optimization, which may increase computational costs and prolong development timelines. Nevertheless, their ability to capture fine-grained structures makes them indispensable in applications requiring precision and topological adaptability.

While deformation and statistical shape models offer reliability and ease of use for standard reconstructions, generative and implicit models provide the flexibility and detail required for more challenging and patient-specific scenarios. This comparative analysis highlights the complementary nature of these models, suggesting that hybrid approaches may often yield the most robust and comprehensive reconstruction outcomes.

## 12 Future Directions

Looking back at the reviewed methods, the development trend of medical image-to-mesh reconstruction has shown a clear technological evolution path: from statistical shape models to template models, then to generative models, and finally to implicit models. Among these, implicit models have demonstrated significant advantages in both fidelity and regularization. Currently, the implicit models used for medical image reconstruction primarily include SDF and NeuralODE approaches.

Meanwhile, in the fields of computer vision and computer graphics, several surface reconstruction algorithms that outperform SDF [Yariv et al. \[2021\]](#) have emerged. High-fidelity surface reconstruction using neural implicit reconstruction [Wang et al. \[2021, 2023a\]](#), [Liu et al. \[2023\]](#), [Yariv et al. \[2023\]](#) has become a hot research topic. Compared to SDF, Neural ODE and NeRF, new representation methods (such as Hash coding [Müller et al. \[2022\]](#), [Li et al. \[2023\]](#), Gaussian splatting [Kerbl et al. \[2023\]](#), [Gao et al. \[2025\]](#), [Guédon and Lepetit \[2024\]](#), [Huang et al. \[2024\]](#), [Yu et al. \[2024\]](#), [Chen et al. \[2024a\]](#), [Dai et al. \[2024\]](#), [Wang et al. \[2024\]](#), [Tang et al. \[2024\]](#)) provide better texture preservation.

Gaussian splatting technique has demonstrated breakthrough advantages in surface reconstruction. This approach achieves superior computational efficiency with training time reduced by more than 10 times [Lyu et al. \[2024\]](#) compared to existing neural implicit reconstruction methods. Through explicit 3D Gaussian point representation and surface alignment strategies, complex surface details can be accurately reconstructed. The flexible optimization framework allows simultaneous optimization of geometric structure and appearance features, achieving high-fidelity reconstruction. Furthermore, its use of sparse 3D Gaussian points representation significantly reduces memory overhead, while its end-to-end reconstruction capability avoids post-processing steps like depth fusion in traditional methods, thereby reducing error accumulation. These ad-

vantages make Gaussian splatting show tremendous potential in medical image reconstruction. In the future, combining this efficient neural surface reconstruction technology with the specific requirements of medical image processing is expected to bring major breakthroughs in medical image reconstruction quality. Particularly in clinical application scenarios that require a balance of reconstruction accuracy, computational efficiency, and real-time performance, the advantages of Gaussian splatting will become especially prominent.

## 13 Conclusion

This comprehensive survey has systematically examined deep learning-based medical image-to-mesh reconstruction methods, categorizing them into four main approaches: statistical shape models, template models, generative models, and implicit models. Furthermore, we have refined this classification into twelve subcategories based on their processing pipelines and feature representations, offering a structured and in-depth taxonomy of existing methodologies. Each approach presents distinct advantages and trade-offs, making them suitable for different medical imaging applications.

Deformation-based template models excel in preserving topological consistency and are well-suited for tasks requiring fixed mesh topology, such as cardiac mesh reconstruction. However, their dependency on predefined templates may limit their adaptability to complex anatomical variations. Statistical shape models leverage prior anatomical knowledge and demonstrate robustness in handling noisy data, making them particularly useful for standard anatomical reconstructions where statistical regularities are beneficial. Generative models introduce unprecedented flexibility in mesh synthesis, enabling personalized reconstructions that can accommodate pathological variations beyond standard anatomical templates. Implicit models offer superior adaptability in topology and allow for high-resolution reconstructions, making them particularly effective for complex anatomical structures with intricate geometric details.

Beyond method classification, this survey has also provided a structured summary of loss functions and evaluation metrics commonly used in image-to-mesh reconstruction. Additionally, we have conducted a meta-analysis of experimental results across different anatomical structures, offering insights into the relative performance of various method categories. Furthermore, we have systematically reviewed and curated publicly available datasets relevant to this field, covering multiple anatomical structures and imaging modalities. This dataset collection serves as a valuable resource for researchers working on medical image-to-mesh reconstruction and in-silico trial simulations.

Looking ahead, new foundational technologies are re-

shaping medical image-to-mesh reconstruction, enabling higher fidelity, efficiency, and adaptability in diverse clinical applications. Emerging representation techniques such as Gaussian splatting offer new possibilities for high-fidelity mesh reconstruction with improved efficiency and scalability. Additionally, generative models like conditional diffusion models have shown significant promise in generating anatomically accurate meshes by incorporating prior constraints and uncertainty quantification. Another key direction is multi-modal fusion, where integrating diverse imaging modalities with deep learning-based reconstruction pipelines can enhance robustness and anatomical consistency. The incorporation of large language models into multi-modal frameworks also presents an exciting frontier, enabling structured prior knowledge integration, automated annotation, and context-aware reconstruction guidance. Furthermore, volume mesh reconstruction is gaining attention, as it is essential for biomechanical simulations and computational modelling, which require volumetric representations beyond surface meshes. These advanced methodologies hold great potential for applications in surgical planning, disease diagnosis, and personalized treatment strategies, paving the way for the next generation of medical image-to-mesh reconstruction.

As deep learning architectures and computational capabilities continue to advance, the field of medical image-to-mesh reconstruction is evolving rapidly. The synthesis of different methodological approaches, combined with the increasing availability of high-quality medical imaging datasets, is expected to drive future innovations. With these advancements, we anticipate that medical image-to-mesh reconstruction will become an integral component of clinical workflows, bridging the gap between medical imaging and practical healthcare applications and ultimately contributing to improved patient care and clinical outcomes.

## 14 Acknowledgements

AFF acknowledges support from the Royal Academy of Engineering under the RAEng Chair in Emerging Technologies (INSILEX CiET191919), ERC Advanced Grant – UKRI Frontier Research Guarantee (INSILICO EPY030494/1), the UK Centre of Excellence on in-silico Regulatory Science and Innovation (UK CEiRSI) (10139527), the National Institute for Health and Care Research (NIHR) Manchester Biomedical Research Centre (BRC) (NIHR203308), the BHF Manchester Centre of Research Excellence (RE24130017), and the CRUK RadNet Manchester (C1994A28701).

## References

- Rahman Attar, Marco Pereañez, Christopher Bowles, Stefan K. Piechnik, Stefan Neubauer, Steffen E. Petersen, and Alejandro F. Frangi. 3D cardiac shape prediction with deep neural networks: Simultaneous use of images and patient metadata. In Dinggang Shen, Tianming Liu, Terry M. Peters, Lawrence H. Staib, Caroline Essert, Sean Zhou, Pew-Thian Yap, and Ali Khan, editors, *Medical Image Computing and Computer Assisted Intervention – MICCAI 2019*, pages 586–594, Cham, 2019a. Springer International Publishing. doi: 10.1007/978-3-030-32245-8\_65.
- Rahman Attar, Marco Pereañez, Ali Gooya, Xènia Albà, Le Zhang, Stefan K. Piechnik, Stefan Neubauer, Steffen E. Petersen, and Alejandro F. Frangi. High throughput computation of reference ranges of biventricular cardiac function on the UK Biobank population cohort. In Mihaela Pop, Maxime Sermesant, Jichao Zhao, Shuo Li, Kristin McLeod, Alistair Young, Kawal Rhode, and Tommaso Mansi, editors, *Statistical Atlases and Computational Models of the Heart. Atrial Segmentation and LV Quantification Challenges*, pages 114–121, Cham, 2019b. Springer International Publishing. doi: 10.1007/978-3-030-12029-0\_13.
- Pablo Azagra, Carlos Sostres, Ángel Ferrández, Luis Riazuelo, Clara Tomasini, O. León Barbed, Javier Morlana, David Recasens, Víctor M. Batlle, Juan J. Gómez-Rodríguez, Richard Elvira, Julia López, Cristina Oriol, Javier Civera, Juan D. Tardós, Ana C. Murillo, Angel Lanás, and José M. M. Montiel. Endomap: dataset of complete calibrated endoscopy procedures. *Scientific Data*, 10(1):671, 2023. doi: 10.1038/s41597-023-02564-7.
- Abu Zahid Bin Aziz, Jadie Adams, and Shireen Elhabian. Progressive DeepSSM: Training methodology for image-to-shape deep models. In Christian Wachinger, Beatriz Paniagua, Shireen Elhabian, Jianning Li, and Jan Egger, editors, *Shape in Medical Imaging*, pages 157–172, Cham, 2023. Springer Nature Switzerland. doi: 10.1007/978-3-031-46914-5\_13.
- Wenjia Bai, Wenzhe Shi, Antonio de Marvao, Timothy J.W. Dawes, Declan P. O’Regan, Stuart A. Cook, and Daniel Rueckert. A bi-ventricular cardiac atlas built from 1000+ high resolution MR images of healthy subjects and an analysis of shape and motion. *Medical Image Analysis*, 26(1):133–145, 2015. doi: 10.1016/j.media.2015.08.009.
- Guha Balakrishnan, Amy Zhao, Mert R. Sabuncu, John Guttag, and Adrian V. Dalca. VoxelMorph: A learning framework for deformable medical image registra-

- tion. *IEEE Transactions on Medical Imaging*, 38(8): 1788–1800, 2019. doi: 10.1109/TMI.2019.2897538.
- Abhirup Banerjee, Julià Camps, Ernesto Zacur, Christopher M. Andrews, Yoram Rudy, Robin P. Choudhury, Blanca Rodriguez, and Vicente Grau. A completely automated pipeline for 3D reconstruction of human heart from 2D cine magnetic resonance slices. *Philosophical Transactions of the Royal Society A: Mathematical, Physical and Engineering Sciences*, 379(2212): 20200257, 2021. doi: 10.1098/rsta.2020.0257.
- Abhirup Banerjee, Ernesto Zacur, Robin P. Choudhury, and Vicente Grau. Automated 3D whole-heart mesh reconstruction from 2D cine MR slices using statistical shape model. *Proceedings of the Annual International Conference of the IEEE Engineering in Medicine and Biology Society, EMBS*, 2022-July:1702–1706, 2022. doi: 10.1109/EMBC48229.2022.9871327.
- Jonathan T. Barron, Ben Mildenhall, Matthew Tancik, Peter Hedman, Ricardo Martin-Brualla, and Pratul P. Srinivasan. Mip-NeRF: A multiscale representation for anti-aliasing neural radiance fields. In *2021 IEEE/CVF International Conference on Computer Vision (ICCV)*, pages 5835–5844, 2021. doi: 10.1109/ICCV48922.2021.00580.
- Víctor M. Batlle, José M. M. Montiel, Pascal Fua, and Juan D. Tardós. LightNeuS: Neural surface reconstruction in endoscopy using illumination decline. In Hayit Greenspan, Anant Madabhushi, Parvin Mousavi, Septimiu Salcudean, James Duncan, Tanveer Syeda-Mahmood, and Russell Taylor, editors, *Medical Image Computing and Computer Assisted Intervention – MICCAI 2023*, pages 502–512, Cham, 2023. Springer Nature Switzerland. doi: 10.1007/978-3-031-43999-5\_48.
- Zachary MC Baum, Seyedeh Uzeir Saeed, Zhouping Min, Yipeng Hu, and Dean C Barratt. MR to ultrasound registration for prostate challenge - dataset. In *Medical Image Computing and Computer Assisted Intervention – MICCAI 2023*. Zenodo, 2023. doi: 10.5281/zenodo.7870105.
- Marcel Beetz, Abhirup Banerjee, and Vicente Grau. Biventricular surface reconstruction from cine mri contours using point completion networks. *Proceedings - International Symposium on Biomedical Imaging*, 2021-April: 105–109, 2021. doi: 10.1109/ISBI48211.2021.9434040.
- Marcel Beetz, Jorge Corral Acero, Abhirup Banerjee, Ingo Eitel, Ernesto Zacur, Torben Lange, Thomas Stiermaier, Ruben Evertz, Sören J. Backhaus, Holger Thiele, Alfonso Bueno-Orovio, Pablo Lamata, Andreas Schuster, and Vicente Grau. Mesh U-Nets for 3D cardiac deformation modeling. In *International Workshop on Statistical Atlases and Computational Models of the Heart*, pages 245–257. Springer, 2022a. doi: 10.1007/978-3-031-23443-9\_23.
- Marcel Beetz, Abhirup Banerjee, and Vicente Grau. Reconstructing 3D cardiac anatomies from misaligned multi-view magnetic resonance images with mesh deformation U-Nets. *Proceedings of Machine Learning Research*, 194:3–14, 2022b.
- Marcel Beetz, Abhirup Banerjee, and Vicente Grau. Point2Mesh-Net: Combining point cloud and mesh-based deep learning for cardiac shape reconstruction. In *Statistical Atlases and Computational Models of the Heart. Regular and CMRxMotion Challenge Papers: 13th International Workshop, STACOM 2022, Held in Conjunction with MICCAI 2022, Singapore, September 18, 2022, Revised Selected Papers*, pages 280–290, Berlin, Heidelberg, 2022c. Springer-Verlag. ISBN 978-3-031-23442-2. doi: 10.1007/978-3-031-23443-9\_26.
- Marcel Beetz, Abhirup Banerjee, Julius Ossenbeng-Engels, and Vicente Grau. Multi-class point cloud completion networks for 3D cardiac anatomy reconstruction from cine magnetic resonance images. *Medical Image Analysis*, 90:102975, 2023. doi: 10.1016/j.media.2023.102975.
- Marcel Beetz, Abhirup Banerjee, and Vicente Grau. Modeling 3D cardiac contraction and relaxation with point cloud deformation networks. *IEEE Journal of Biomedical and Health Informatics*, 28(8):4810–4819, 2024. doi: 10.1109/JBHI.2024.3389871.
- Olivier Bernard, Alain Lalande, Clement Zotti, Frederick Cervenansky, Xin Yang, Pheng-Ann Heng, Irem Cetin, Karim Lekadir, Oscar Camara, Miguel Angel Gonzalez Ballester, Gerard Sanroma, Sandy Napel, Steffen Petersen, Georgios Tziritas, Elias Grinias, Mahendra Khened, Varghese Alex Kollerathu, Ganapathy Krishnamurthi, Marc-Michel Rohé, Xavier Pennec, Maxime Sermesant, Fabian Isensee, Paul Jäger, Klaus H. Maier-Hein, Peter M. Full, Ivo Wolf, Sandy Engelhardt, Christian F. Baumgartner, Lisa M. Koch, Jelmer M. Wolterink, Ivana Išgum, Yeonggul Jang, Yoonmi Hong, Jay Patravali, Shubham Jain, Olivier Humbert, and Pierre-Marc Jodoin. Deep learning techniques for automatic MRI cardiac multi-structures segmentation and diagnosis: is the problem solved? *IEEE Transactions on Medical Imaging*, 37(11):2514–2525, 2018. doi: 10.1109/TMI.2018.2837502.
- Fausto Bernardini, Joshua Mittleman, Holly Rushmeier, Claudio Silva, and Gabriel Taubin. The ball-pivoting algorithm for surface reconstruction. *IEEE Transactions*

- on *Visualization and Computer Graphics*, 5(4):349–359, 1999. doi: 10.1109/2945.817351.
- Riddhish Bhalodia, Shireen Elhabian, Jadie Adams, Wenzheng Tao, Ladislav Kavan, and Ross Whitaker. DeepSSM: A blueprint for image-to-shape deep learning models. *Medical Image Analysis*, 91:103034, 2024. doi: 10.1016/j.media.2023.103034.
- Diane E. Bild, David A. Bluemke, Gregory L. Burke, Robert Detrano, Ana V. Diez Roux, Aaron R. Folsom, Philip Greenland, David R. Jacobs Jr., Richard Kronmal, Kiang Liu, Jennifer Clark Nelson, Daniel O’Leary, Mohammed F. Saad, Steven Shea, Moyses Szklo, and Russell P. Tracy. Multi-ethnic study of atherosclerosis: Objectives and design. *American Journal of Epidemiology*, 156(9):871–881, 2002. doi: 10.1093/aje/kwf113.
- Taylor L. Bobrow, Mayank Golhar, Rohan Vijayan, Venkata S. Akshintala, Juan R. Garcia, and Nicholas J. Durr. Colonoscopy 3D video dataset with paired depth from 2D-3D registration. *Medical Image Analysis*, 90:102956, 2023. doi: 10.1016/j.media.2023.102956.
- Fabian Bongratz, Anne-Marie Rickmann, Sebastian Pölsterl, and Christian Wachinger. Vox2Cortex: Fast explicit reconstruction of cortical surfaces from 3D MRI scans with geometric deep neural networks. In *2022 IEEE/CVF Conference on Computer Vision and Pattern Recognition (CVPR)*, pages 20741–20751, 2022. doi: 10.1109/CVPR52688.2022.02011.
- Fabian Bongratz, Anne-Marie Rickmann, and Christian Wachinger. Neural deformation fields for template-based reconstruction of cortical surfaces from MRI. *Medical Image Analysis*, 93:103093, 2024. doi: 10.1016/j.media.2024.103093.
- Kit Mills Bransby, Vincenzo Tufaro, Murat Cap, Greg Slabaugh, Christos Bourantas, and Qianni Zhang. 3D coronary vessel reconstruction from bi-plane angiography using graph convolutional networks. *Proceedings - International Symposium on Biomedical Imaging*, 2023. doi: 10.1109/ISBI53787.2023.10230372.
- Victor M. Campello, Polyxeni Gkontra, Cristian Izquierdo, Carlos Martin-Isla, Alireza Sojoudi, Peter M. Full, Klaus Maier-Hein, Yao Zhang, Zhiqiang He, Jun Ma, Mario Parreno, Alberto Albiol, Fanwei Kong, Shawn C. Shadden, Jorge Corral Acero, Vaanathi Sundaresan, Mina Saber, Mustafa Elattar, Hongwei Li, Bjoern Menze, Firas Khader, Christoph Haarbuerger, Cian M. Scannell, Mitko Veta, Adam Carscadden, Kumaradevan Punithakumar, Xiao Liu, Sotirios A. Tsaftaris, Xiaoqiong Huang, Xin Yang, Lei Li, Xiahai Zhuang, David Viladés, Martin L. Descalzo, Andrea Guala, Lucia La Mura, Matthias G. Friedrich, Ria Garg, Julie Lebel, Filipe Henriques, Mahir Karakas, Ersin Çavuş, Steffen E. Petersen, Sergio Escalera, Santi Segui, Jose F. Rodriguez-Palomares, and Karim Lekadir. Multi-centre, multi-vendor and multi-disease cardiac segmentation: The M&Ms challenge. *IEEE Transactions on Medical Imaging*, 40(12):3543–3554, 2021. doi: 10.1109/TMI.2021.3090082.
- Richard Castillo, Edward Castillo, Rudy Guerra, Valen E Johnson, Travis McPhail, Amit K Garg, and Thomas Guerrero. A framework for evaluation of deformable image registration spatial accuracy using large landmark point sets. *Physics in Medicine and Biology*, 54(7):1849–1870, 2009. doi: 10.1088/0031-9155/54/7/001.
- Juan J. Cerrolaza, Yuanwei Li, Carlo Biffi, Alberto Gomez, Matthew Sinclair, Jacqueline Matthew, Caronline Knight, Bernhard Kainz, and Daniel Rueckert. 3D fetal skull reconstruction from 2DUS via deep conditional generative networks. In Alejandro F. Frangi, Julia A. Schnabel, Christos Davatzikos, Carlos Alberola-López, and Gabor Fichtinger, editors, *Medical Image Computing and Computer Assisted Intervention – MICCAI 2018*, pages 383–391, Cham, 2018. Springer International Publishing. doi: 10.1007/978-3-030-00928-1\_44.
- Qi Chang, Zhennan Yan, Mu Zhou, Di Liu, Khalid Sawalha, Meng Ye, Qilong Zhangli, Mikael Kanski, Subhi Al’Aref, Leon Axel, and Dimitris Metaxas. Deep-Recon: Joint 2D cardiac segmentation and 3D volume reconstruction via a structure-specific generative method. In Linwei Wang, Qi Dou, P. Thomas Fletcher, Stefanie Speidel, and Shuo Li, editors, *Medical Image Computing and Computer Assisted Intervention – MICCAI 2022*, pages 567–577, Cham, 2022. Springer Nature Switzerland. doi: 10.1007/978-3-031-16440-8\_54.
- R. Qi Charles, Hao Su, Mo Kaichun, and Leonidas J. Guibas. Pointnet: Deep learning on point sets for 3D classification and segmentation. In *2017 IEEE Conference on Computer Vision and Pattern Recognition (CVPR)*, pages 77–85, 2017. doi: 10.1109/CVPR.2017.16.
- Danpeng Chen, Hai Li, Weicai Ye, Yifan Wang, Weijian Xie, Shangjin Zhai, Nan Wang, Haomin Liu, Hujun Bao, and Guofeng Zhang. PGSR: Planar-based Gaussian splatting for efficient and high-fidelity surface reconstruction. *arXiv preprint arXiv:2406.06521*, 2024a.
- Hongbo Chen, Logiraj Kumaralingam, Jiawen Li, Kumaradevan Punithakumar, Lawrence H. Le, and Rui Zheng. Neural implicit representation for three-dimensional ultrasound carotid surface reconstruction using unsigned



- distance function. *IEEE International Ultrasonics Symposium, IUS*, 2023. doi: 10.1109/IUS51837.2023.10307668.
- Hongbo Chen, Logiraj Kumaralingam, Shuhang Zhang, Sheng Song, Fayi Zhang, Haibin Zhang, Thanh-Tu Pham, Kumaradevan Punithakumar, Edmond H.M. Lou, Yuyao Zhang, Lawrence H. Le, and Rui Zheng. Neural implicit surface reconstruction of freehand 3D ultrasound volume with geometric constraints. *Medical Image Analysis*, 98:103305, 2024b. doi: 10.1016/j.media.2024.103305.
- Xiang Chen, Nishant Ravikumar, Yan Xia, Rahman Attar, Andres Diaz-Pinto, Stefan K Piechnik, Stefan Neubauer, Steffen E Petersen, and Alejandro F Frangi. Shape registration with learned deformations for 3D shape reconstruction from sparse and incomplete point clouds. *Medical Image Analysis*, 74:102228, 2021. doi: 10.1016/j.media.2021.102228.
- Haili Chui and Anand Rangarajan. A new point matching algorithm for non-rigid registration. *Computer Vision and Image Understanding*, 89(2-3):114-141, 2003. doi: 10.1016/S1077-3142(03)00009-2.
- Timothy F Cootes, Christopher J Taylor, David H Cooper, and Jim Graham. Active shape models-their training and application. *Computer Vision and Image Understanding*, 61(1):38-59, 1995. doi: 10.1006/cviu.1995.1004.
- Rodrigo Santa Cruz, Leo Lebrat, Pierrick Bourgeat, Clinton Fookes, Jurgen Fripp, and Olivier Salvado. DeepCSR: A 3D deep learning approach for cortical surface reconstruction. In *2021 IEEE Winter Conference on Applications of Computer Vision (WACV)*, pages 806-815, 2021. doi: 10.1109/WACV48630.2021.00085.
- Pinxuan Dai, Jiamin Xu, Wenxiang Xie, Xinguo Liu, Huamin Wang, and Weiwei Xu. High-quality surface reconstruction using gaussian surfels. In *ACM SIGGRAPH 2024 Conference Papers*, New York, NY, USA, 2024. Association for Computing Machinery. ISBN 9798400705250. doi: 10.1145/3641519.3657441.
- IXI Dataset. Ixi dataset - information extraction from images. <http://brain-development.org/ixi-dataset/>, 2021.
- Rahul S. Desikan, Florent Ségonne, Bruce Fischl, Brian T. Quinn, Bradford C. Dickerson, Deborah Blacker, Randy L. Buckner, Anders M. Dale, R. Paul Maguire, Bradley T. Hyman, Marilyn S. Albert, and Ronald J. Killiany. An automated labeling system for subdividing the human cerebral cortex on MRI scans into gyral based regions of interest. *NeuroImage*, 31(3):968-980, 2006. doi: 10.1016/j.neuroimage.2006.01.021.
- Haoqiang Fan, Hao Su, and Leonidas Guibas. A point set generation network for 3D object reconstruction from a single image. In *2017 IEEE Conference on Computer Vision and Pattern Recognition (CVPR)*, pages 2463-2471, 2017. doi: 10.1109/CVPR.2017.264.
- Mathieu Fernandes, Yann Gavet, and Jean-Charles Pinoli. Robust 3-D reconstruction of surfaces from image focus by local cross-sectional multivariate statistical analyses: Application to human ex vivo corneal endotheliums. *Medical Image Analysis*, 16(6):1293-1306, 2012. doi: 10.1016/j.media.2012.05.004.
- Bruce Fischl, David H. Salat, Evelina Busa, Marilyn Albert, Megan Dieterich, Christian Haselgrove, Andre Van Der Kouwe, Ron Killiany, David Kennedy, Shuna Klavenness, Albert Montillo, Nikos Makris, Bruce Rosen, and Anders M. Dale. Whole brain segmentation: Automated labeling of neuroanatomical structures in the human brain. *Neuron*, 33(3):341-355, 2002. doi: 10.1016/S0896-6273(02)00569-X.
- Carissa G. Fonseca, Michael Backhaus, David A. Bluemke, Randall D. Britten, Jae Do Chung, Brett R. Cowan, Ivo D. Dinov, J. Paul Finn, Peter J. Hunter, Alan H. Kadish, Daniel C. Lee, Joao A. C. Lima, Pau Medrano-Gracia, Kalyanam Shivkumar, Avan Suinesiaputra, Wenchao Tao, and Alistair A. Young. The cardiac atlas project-an imaging database for computational modeling and statistical atlases of the heart. *Bioinformatics*, 27(16):2288-2295, 2011. doi: 10.1093/bioinformatics/btr360.
- Alejandro F. Frangi, Wiro J. Niessen, Paul J. Nederkoorn, Jeannette Bakker, Willem P. Th. M. Mali, and Max A. Viergever. Quantitative analysis of vascular morphology from 3D MR angiograms: In vitro and in vivo results. *Magnetic Resonance in Medicine*, 45(2):311-322, 2001. doi: 10.1002/1522-2594(200102)45:2<311::AID-MRM1040>3.0.CO;2-7.
- Nicolás Gaggion, Benjamin A. Matheson, Yan Xia, Rodrigo Bonazzola, Nishant Ravikumar, Zeike A. Taylor, Diego H. Milone, Alejandro F. Frangi, and Enzo Ferrante. Multi-view hybrid graph convolutional network for volume-to-mesh reconstruction in cardiovascular MRI. *arXiv preprint arXiv:2311.13706*, 2024.
- Jian Gao, Chun Gu, Youtian Lin, Zhihao Li, Hao Zhu, Xun Cao, Li Zhang, and Yao Yao. Relightable 3D Gaussians: Realistic point cloud relighting with BRDF decomposition and ray tracing. In Aleš Leonardis, Elisa Ricci, Stefan Roth, Olga Russakovsky, Torsten Sattler, and Gül Varol, editors, *Computer Vision – ECCV 2024*, pages 73-89, Cham, 2025. Springer Nature Switzerland. doi: 10.1007/978-3-031-72995-9\_5.

- Haixiao Geng, Jingfan Fan, Shuo Yang, Sigeng Chen, Deqiang Xiao, Danni Ai, Tianyu Fu, Hong Song, Kai Yuan, Feng Duan, Yongtian Wang, and Jian Yang. DSC-Recon: Dual-stage complementary 4-D organ reconstruction from X-ray image sequence for intraoperative fusion. *IEEE Transactions on Medical Imaging*, 43(11): 3909–3923, 2024. doi: 10.1109/TMI.2024.3406876.
- Kathleen Gilbert, Charlène Mauger, Alistair A. Young, and Avan Suinesiaputra. Artificial intelligence in cardiac imaging with statistical atlases of cardiac anatomy. *Frontiers in Cardiovascular Medicine*, 7, 2020. doi: 10.3389/fcvm.2020.00102.
- Randy L. Gollub, Jody M. Shoemaker, Margaret D. King, Tonya White, Stefan Ehrlich, Scott R. Sponheim, Vincent P. Clark, Jessica A. Turner, Bryon A. Mueller, Vince Magnotta, Daniel O’Leary, Beng C. Ho, Stefan Brauns, Dara S. Manoach, Larry Seidman, Juan R. Bustillo, John Lauriello, Jeremy Bockholt, Kelvin O. Lim, Bruce R. Rosen, S. Charles Schulz, Vince D. Calhoun, and Nancy C. Andreasen. The MCIC collection: A shared repository of multi-modal, multi-site brain image data from a clinical investigation of schizophrenia. *Neuroinformatics*, 11(3):367–388, 2013. doi: 10.1007/s12021-013-9184-3.
- Sachin Govil, Brendan T. Crabb, Yu Deng, Laura Dal Toso, Esther Puyol-Antón, Kuberan Pushparajah, Sanjeet Hegde, James C. Perry, Jeffrey H. Omens, Albert Hsiao, Alistair A. Young, and Andrew D. McCulloch. A deep learning approach for fully automated cardiac shape modeling in tetralogy of Fallot. *Journal of Cardiovascular Magnetic Resonance*, 25(1), 2023. doi: 10.1186/s12968-023-00924-1.
- Antoine Guédon and Vincent Lepetit. SuGaR: Surface-aligned Gaussian splatting for efficient 3D mesh reconstruction and high-quality mesh rendering. In *2024 IEEE/CVF Conference on Computer Vision and Pattern Recognition (CVPR)*, pages 5354–5363, 2024. doi: 10.1109/CVPR52733.2024.00512.
- Kunal Gupta. *Neural mesh flow: 3D manifold mesh generation via diffeomorphic flows*. PhD thesis, University of California, San Diego, 2020.
- Gokce Guven, Hasan F. Ates, and H. Fatih Ugurdag. X2V: 3D organ volume reconstruction from a planar X-ray image with neural implicit methods. *IEEE Access*, 12:50898–50910, 2024. doi: 10.1109/ACCESS.2024.3385668.
- Lasse Hansen and Mattias P. Heinrich. GraphRegNet: Deep graph regularisation networks on sparse keypoints for dense registration of 3D lung CTs. *IEEE Transactions on Medical Imaging*, 40(9):2246–2257, 2021. doi: 10.1109/TMI.2021.3073986.
- S. M. Kamrul Hasan and Cristian A. Linte. CondenseUNet: A memory-efficient condensely-connected architecture for bi-ventricular blood pool and myocardium segmentation. volume 11315, 2020. doi: 10.1117/12.2550640.
- Xiaoxiao He, Chaowei Tan, Ligong Han, Bo Liu, Leon Axel, Kang Li, and Dimitris N. Metaxas. DMCVR: Morphology-guided diffusion model for 3D cardiac volume reconstruction. In Hayit Greenspan, Anant Madabhushi, Parvin Mousavi, Septimiu Salcudean, James Duncan, Tanveer Syeda-Mahmood, and Russell Taylor, editors, *Medical Image Computing and Computer Assisted Intervention – MICCAI 2023*, pages 132–142, Cham, 2023. Springer Nature Switzerland. doi: 10.1007/978-3-031-43990-2\_13.
- Tobias Heimann and Hans-Peter Meinzer. Statistical shape models for 3D medical image segmentation: a review. *Medical Image Analysis*, 13(4):543–563, 2009. doi: 10.1016/j.media.2009.05.004.
- Jonathan Ho, Ajay Jain, and Pieter Abbeel. Denoising diffusion probabilistic models. *Advances in Neural Information Processing Systems*, 33:6840–6851, 2020.
- Johannes Hofmanninger, Florian Prayer, Jeanny Pan, Sebastian Röhrich, Helmut Prosch, and Georg Langs. Automatic lung segmentation in routine imaging is primarily a data diversity problem, not a methodology problem. *European Radiology Experimental*, 4(1), 2020. doi: 10.1186/s41747-020-00173-2.
- Yoonmi Hong, Sahar Ahmad, Ye Wu, Siyuan Liu, and Pew-Thian Yap. Vox2Surf: Implicit surface reconstruction from volumetric data. In *Machine Learning in Medical Imaging: 12th International Workshop, MLMI 2021, Held in Conjunction with MICCAI 2021, Strasbourg, France, September 27, 2021, Proceedings*, pages 644–653, Berlin, Heidelberg, 2021. Springer-Verlag. ISBN 978-3-030-87588-6. doi: 10.1007/978-3-030-87589-3\_66.
- Andrew Hoopes, Juan Eugenio Iglesias, Bruce Fischl, Douglas Greve, and Adrian V. Dalca. TopoFit: Rapid reconstruction of topologically-correct cortical surfaces. *Proceedings of Machine Learning Research*, 172:508–520, 2022.
- Andrew G Howard, Menglong Zhu, Bo Chen, Dmitry Kalenichenko, Weijun Wang, Tobias Weyand, Marco Andreetto, and Hartwig Adam. MobileNets: Efficient convolutional neural networks for mobile vision applications. *arXiv preprint arXiv:1704.04861*, 2017.

- Bowen Hu, Baiying Lei, Yanyan Shen, Yong Liu, and Shuqiang Wang. A point cloud generative model via tree-structured graph convolutions for 3D brain shape reconstruction. In *Pattern Recognition and Computer Vision. PRCV 2021*, pages 263–274. Springer, 2021. doi: 10.1007/978-3-030-88007-1\_22.
- Bowen Hu, Yanyan Shen, Guocheng Wu, and Shuqiang Wang. SRT: Shape reconstruction transformer for 3D reconstruction of point cloud from 2D MRI. In *Proceedings of the 2022 14th International Conference on Machine Learning and Computing*, pages 507–511, New York, NY, USA, 2022. Association for Computing Machinery. ISBN 9781450395700. doi: 10.1145/3529836.3529902.
- Bowen Hu, Choujun Zhan, Buzhou Tang, Bingchuan Wang, Baiying Lei, and Shu-Qiang Wang. 3-D brain reconstruction by hierarchical shape-perception network from a single incomplete image. *IEEE Transactions on Neural Networks and Learning Systems*, 35(10):13271–13283, 2024. doi: 10.1109/TNNLS.2023.3266819.
- Binbin Huang, Zehao Yu, Anpei Chen, Andreas Geiger, and Shenghua Gao. 2D Gaussian splatting for geometrically accurate radiance fields. In *ACM SIGGRAPH 2024 Conference Papers*, New York, NY, USA, 2024. Association for Computing Machinery. ISBN 9798400705250. doi: 10.1145/3641519.3657428.
- Emer J. Hughes, Tobias Winchman, Francesco Padormo, Rui Teixeira, Julia Wurie, Maryanne Sharma, Matthew Fox, Jana Hutter, Lucilio Cordero-Grande, Anthony N. Price, Joanna Allsop, Jose Bueno-Conde, Nora Tusor, Tomoki Arichi, A. D. Edwards, Mary A. Rutherford, Serena J. Counsell, and Joseph V. Hajnal. A dedicated neonatal brain imaging system. *Magnetic Resonance in Medicine*, 78(2):794–804, 2017. doi: 10.1002/mrm.26462.
- Geoffrey D. Hugo, Elisabeth Weiss, William C. Sleeman, Salim Balik, Paul J. Keall, Jun Lu, and Jeffrey F. Williamson. A longitudinal four-dimensional computed tomography and cone beam computed tomography dataset for image-guided radiation therapy research in lung cancer. *Medical Physics*, 44(2):762–771, 2017. doi: 10.1002/mp.12059.
- Takeshi Iwatsubo. Japanese Alzheimer’s disease neuroimaging initiative: Present status and future. *Alzheimer’s and Dementia*, 6(3):297–299, 2010. doi: 10.1016/j.jalz.2010.03.011.
- Clifford R. Jack Jr., Matt A. Bernstein, Nick C. Fox, Paul Thompson, Gene Alexander, Danielle Harvey, Bret Borowski, Paula J. Britson, Jennifer L. Whitwell, Chadwick Ward, Anders M. Dale, Joel P. Felmlee, Jeffrey L. Gunter, Derek L.G. Hill, Ron Killiany, Norbert Schuff, Sabrina Fox-Bosetti, Chen Lin, Colin Studholme, Charles S. DeCarli, Gunnar Krueger, Heidi A. Ward, Gregory J. Metzger, Katherine T. Scott, Richard Mallozzi, Daniel Blezek, Joshua Levy, Josef P. Debbins, Adam S. Fleisher, Marilyn Albert, Robert Green, George Bartzokis, Gary Glover, John Mugler, and Michael W. Weiner. The Alzheimer’s disease neuroimaging initiative (ADNI): MRI methods. *Journal of Magnetic Resonance Imaging*, 27(4):685–691, 2008. doi: 10.1002/jmri.21049.
- Bing Jian and Baba C Vemuri. Robust point set registration using Gaussian mixture models. *IEEE Transactions on Pattern Analysis and Machine Intelligence*, 33(8):1633–1645, 2010. doi: 10.1109/TPAMI.2010.223.
- Thomas Julian, Nicholas Glasgow, Rubiya Syeed, and Panagiotis Zis. Alcohol-related peripheral neuropathy: a systematic review and meta-analysis. *Journal of Neurology*, 266(12):2907–2919, 2019. doi: 10.1007/s00415-018-9123-1.
- Rashed Karim, Lauren-Emma Blake, Jiro Inoue, Qian Tao, Shuman Jia, R. James Housden, Pranav Bhagirath, Jean-Luc Duval, Marta Varela, Jonathan Behar, Loïc Cadour, Rob J. van der Geest, Hubert Cochet, Maria Drangova, Maxime Sermesant, Reza Razavi, Oleg Aslanidi, Ronak Rajani, and Kawal Rhode. Algorithms for left atrial wall segmentation and thickness – evaluation on an open-source CT and MRI image database. *Medical Image Analysis*, 50:36–53, 2018. doi: 10.1016/j.media.2018.08.004.
- Amirhossein Kazerooni, Ehsan Khodapanah Aghdam, Moein Heidari, Reza Azad, Mohsen Fayyaz, Ilker Hacıhaliloglu, and Dorit Merhof. Diffusion models in medical imaging: A comprehensive survey. *Medical Image Analysis*, 88:102846, 2023. doi: 10.1016/j.media.2023.102846.
- Bernhard Kerbl, Georgios Kopanas, Thomas Leimkühler, and George Drettakis. 3D Gaussian splatting for real-time radiance field rendering. *ACM Transactions on Graphics (TOG)*, 42(4), 2023. doi: 10.1145/3592433.
- S.S. Khalafvand, J.D. Voorneveld, A. Muralidharan, F.J.H. Gijzen, J.G. Bosch, T. van Walsum, A. Haak, N. de Jong, and S. Kenjeres. Assessment of human left ventricle flow using statistical shape modelling and computational fluid dynamics. *Journal of Biomechanics*, 74:116–125, 2018. doi: 10.1016/j.jbiomech.2018.04.030.
- Diederik P. Kingma and Max Welling. Auto-encoding variational Bayes. In *2nd International Conference on Learn-*

- ing Representations, *ICLR 2014 - Conference Track Proceedings*, 2014.
- Kitware. Medical imaging and visualization datasets. <https://data.kitware.com>, 2024.
- Arno Klein and Jason Tourville. 101 labeled brain images and a consistent human cortical labeling protocol. *Frontiers in Neuroscience*, (DEC), 2012. doi: 10.3389/fnins.2012.00171.
- Roland Klingenberg, Dik Heg, Lorenz Räber, David Carballo, David Nanchen, Baris Gencer, Reto Auer, Milosz Jaguszewski, Barbara E. Stähli, Philipp Jakob, Christian Templin, Giulio G. Stefanini, Bernhard Meier, Pierre Vogt, Marco Roffi, Willibald Maier, Ulf Landmesser, Nicolas Rodondi, François Mach, Stephan Windecker, Peter Jüni, Thomas F. Lüscher, and Christian M. Matter. Safety profile of prasugrel and clopidogrel in patients with acute coronary syndromes in Switzerland. *Heart*, 101(11):854–863, 2015. doi: 10.1136/heartjnl-2014-306925.
- Oldřich Kodým, Jianning Li, Antonio Pepe, Christina Gsaxner, Sasank Chilamkurthy, Jan Egger, and Michal Španěl. SkullBreak/SkullFix – dataset for automatic cranial implant design and a benchmark for volumetric shape learning tasks. *Data in Brief*, 35:106902, 2021. doi: 10.1016/j.dib.2021.106902.
- Fanwei Kong and Shawn C. Shadden. Whole heart mesh generation for image-based computational simulations by learning free-from deformations. In Marleen de Bruijne, Philippe C. Cattin, Stéphane Cotin, Nicolas Padoy, Stefanie Speidel, Yefeng Zheng, and Caroline Essert, editors, *Medical Image Computing and Computer Assisted Intervention – MICCAI 2021*, pages 550–559, Cham, 2021. Springer International Publishing. doi: 10.1007/978-3-030-87202-1\_53.
- Fanwei Kong and Shawn C. Shadden. Learning whole heart mesh generation from patient images for computational simulations. *IEEE Transactions on Medical Imaging*, 42(2):533–545, 2023. doi: 10.1109/TMI.2022.3219284.
- Fanwei Kong, Nathan Wilson, and Shawn Shadden. A deep-learning approach for direct whole-heart mesh reconstruction. *Medical Image Analysis*, 74:102222, 2021. doi: 10.1016/j.media.2021.102222.
- Nina Krüger, Jan Brüning, Leonid Goubergrits, Matthias Ivantsits, Lars Walczak, Volkmar Falk, Henryk Dreger, Titus Kühne, and Anja Hennemuth. Deep learning-based pulmonary artery surface mesh generation. In Oscar Camara, Esther Puyol-Antón, Maxime Sermesant, Avan Suinesiaputra, Qian Tao, Chengyan Wang, and Alistair Young, editors, *Statistical Atlases and Computational Models of the Heart. Regular and CMRxRecon Challenge Papers*, pages 140–151, Cham, 2024. Springer Nature Switzerland. doi: 10.1007/978-3-031-52448-6\_14.
- B.A. Landman and S.K. Warfield. *MICCAI 2012 Workshop on Multi-Atlas Labeling*. CreateSpace Independent Publishing Platform, 2012. ISBN 9781479126187.
- Fabian Laumer, Mounir Amrani, Laura Manduchi, Ami Beuret, Lena Rubi, Alina Dubatovka, Christian M. Matter, and Joachim M. Buhmann. Weakly supervised inference of personalized heart meshes based on echocardiography videos. *Medical Image Analysis*, 83:102653, 2023. doi: 10.1016/j.media.2022.102653.
- Fabian Laumer, Lena Rubi, Michael A Matter, Stefano Buzo, Gabriel Fringeli, François Mach, Frank Ruschitzka, Joachim M Buhmann, and Christian M Matter. 2D echocardiography video to 3D heart shape reconstruction for clinical application. *Medical Image Analysis*, 101:103434, 2025. doi: 10.1016/j.media.2024.103434.
- Leo Lebrat, Rodrigo Santa Cruz, Frederic de Gournay, Darren Fu, Pierrick Bourgeat, Jurgen Frapp, Clinton Fookes, and Olivier Salvado. CorticalFlow: a diffeomorphic mesh transformer network for cortical surface reconstruction. *Advances in Neural Information Processing Systems*, 34:29491–29505, 2021.
- Gang Li, Li Wang, Feng Shi, John H. Gilmore, Weili Lin, and Dinggang Shen. Construction of 4D high-definition cortical surface atlases of infants: Methods and applications. *Medical Image Analysis*, 25(1):22–36, 2015. doi: 10.1016/j.media.2015.04.005.
- Jianning Li, Marcell Krall, Florian Trummer, Afaq Rafique Memon, Antonio Pepe, Christina Gsaxner, Yuan Jin, Xiaojun Chen, Hannes Deutschmann, Ulrike Zefferer, Ute Schäfer, Gord von Campe, and Jan Egger. MUG500+: Database of 500 high-resolution healthy human skulls and 29 craniotomy skulls and implants. *Data in Brief*, 39:107524, 2021. doi: 10.1016/j.dib.2021.107524.
- Zhaoshuo Li, Thomas Müller, Alex Evans, Russell H. Taylor, Mathias Unberath, Ming-Yu Liu, and Chen-Hsuan Lin. Neuralangelo: High-fidelity neural surface reconstruction. In *2023 IEEE/CVF Conference on Computer Vision and Pattern Recognition (CVPR)*, pages 8456–8465, 2023. doi: 10.1109/CVPR52729.2023.00817.
- Fengming Lin, Yan Xia, Shuang Song, Nishant Ravikumar, and Alejandro F. Frangi. High-throughput 3DRA segmentation of brain vasculature and aneurysms using deep learning. *Computer Methods and Programs in*

- Biomedicine*, 230:107355, 2023. doi: 10.1016/j.cmpb.2023.107355.
- Yuan Liu, Peng Wang, Cheng Lin, Xiaoxiao Long, Jiepeng Wang, Lingjie Liu, Taku Komura, and Wenping Wang. NeRO: Neural geometry and BRDF reconstruction of reflective objects from multiview images. *ACM Transactions on Graphics (TOG)*, 42(4), 2023. doi: 10.1145/3592134.
- William E. Lorensen and Harvey E. Cline. Marching cubes: A high resolution 3D surface construction algorithm. *SIGGRAPH Comput. Graph.*, 21(4):163–169, aug 1987. ISSN 0097-8930. doi: 10.1145/37402.37422.
- Yihao Luo, Dario Sesia, Fanwen Wang, Yinzhe Wu, Wenhao Ding, Jiahao Huang, Fadong Shi, Anoop Shah, Amit Kaural, Jamil Mayet, Guang Yang, and ChoonHwai Yap. Explicit differentiable slicing and global deformation for cardiac mesh reconstruction. *arXiv preprint arXiv:2409.02070*, 2024.
- Xiaoyang Lyu, Yang-Tian Sun, Yi-Hua Huang, Xiuzhe Wu, Ziyi Yang, Yilun Chen, Jiangmiao Pang, and Xiaojuan Qi. 3DGSr: Implicit surface reconstruction with 3D Gaussian splatting. *ACM Transactions on Graphics (TOG)*, 43(6), 2024. doi: 10.1145/3687952.
- Qiang Ma, Emma C. Robinson, Bernhard Kainz, Daniel Rueckert, and Amir Alansary. PIALNN: A fast deep learning framework for cortical pial surface reconstruction. In Ahmed Abdulkadir, Seyed Mostafa Kia, Mohamad Habes, Vinod Kumar, Jane Maryam Rondina, Chantal Tax, and Thomas Wolfers, editors, *Machine Learning in Clinical Neuroimaging*, pages 73–81, Cham, 2021. Springer International Publishing. doi: 10.1007/978-3-030-87586-2\_8.
- Qiang Ma, Liu Li, Emma C. Robinson, Bernhard Kainz, Daniel Rueckert, and Amir Alansary. CortexODE: Learning cortical surface reconstruction by neural ODEs. *IEEE Transactions on Medical Imaging*, 42(2):430–443, 2023. doi: 10.1109/TMI.2022.3206221.
- Julian Maclaren, Zhaoying Han, Sjoerd B Vos, Nancy Fischbein, and Roland Bammer. Reliability of brain volume measurements: A test-retest dataset. *Scientific Data*, 1: 140037, 2014. doi: 10.1038/sdata.2014.37.
- Michael MacRaid, Ali Sarrami-Foroushani, Shuang Song, Qiongyao Liu, Christopher Kelly, Nishant Ravikumar, Tufail Patankar, Toni Lassila, Zeike A Taylor, and Alejandro F Frangi. Off-label in-silico flow diverter performance assessment in posterior communicating artery aneurysms. *Journal of NeuroInterventional Surgery*, 2024. doi: 10.1136/jnis-2024-022000.
- Daniel S Marcus, Tracy H Wang, Jamie Parker, John G Csernansky, John C Morris, and Randy L Buckner. Open access series of imaging studies (OASIS): Cross-sectional MRI data in young, middle aged, nondemented, and demented older adults. *Journal of Cognitive Neuroscience*, 19(9):1498–1507, 2007. doi: 10.1162/jocn.2007.19.9.1498.
- Di Folco Maxime, Moceri Pamela, Clarysse Patrick, and Duchateau Nicolas. Characterizing interactions between cardiac shape and deformation by non-linear manifold learning. *Medical Image Analysis*, 75:102278, 2022. doi: 10.1016/j.media.2021.102278.
- Qingjie Meng, Wenjia Bai, Tianrui Liu, Declan P. O’Regan, and Daniel Rueckert. Mesh-based 3D motion tracking in cardiac MRI using deep learning. In Linwei Wang, Qi Dou, P. Thomas Fletcher, Stefanie Speidel, and Shuo Li, editors, *Medical Image Computing and Computer Assisted Intervention – MICCAI 2022*, pages 248–258, Cham, 2022a. Springer Nature Switzerland. doi: 10.1007/978-3-031-16446-0\_24.
- Qingjie Meng, Chen Qin, Wenjia Bai, Tianrui Liu, Antonio De Marvao, Declan P O’Regan, and Daniel Rueckert. MulViMotion: Shape-aware 3D myocardial motion tracking from multi-view cardiac MRI. *IEEE Transactions on Medical Imaging*, 41(8):1961–1974, 2022b. doi: 10.1109/TMI.2022.3154599.
- Qingjie Meng, Wenjia Bai, Declan P. O’Regan, and Daniel Rueckert. DeepMesh: Mesh-based cardiac motion tracking using deep learning. *IEEE Transactions on Medical Imaging*, 43(4):1489–1500, 2024. doi: 10.1109/TMI.2023.3340118.
- Ben Mildenhall, Pratul P Srinivasan, Matthew Tancik, Jonathan T Barron, Ravi Ramamoorthi, and Ren Ng. Nerf: Representing scenes as neural radiance fields for view synthesis. *Communications of the ACM*, 65(1):99–106, 2021. doi: 10.1145/3503250.
- Thomas Müller, Alex Evans, Christoph Schied, and Alexander Keller. Instant neural graphics primitives with a multiresolution hash encoding. *ACM transactions on graphics (TOG)*, 41(4), 2022. doi: 10.1145/3528223.3530127.
- Andriy Myronenko and Xubo Song. Point set registration: Coherent point drift. *IEEE Transactions on Pattern Analysis and Machine Intelligence*, 32(12):2262–2275, 2010. doi: 10.1109/TPAMI.2010.46.
- Megumi Nakao, Fei Tong, Mitsuhiro Nakamura, and Tetsuya Matsuda. Image-to-graph convolutional network for deformable shape reconstruction from a single projection image. In Marleen de Bruijne, Philippe C. Cattin,



- Stéphane Cotin, Nicolas Padoy, Stefanie Speidel, Yefeng Zheng, and Caroline Essert, editors, *Medical Image Computing and Computer Assisted Intervention – MICCAI 2021*, pages 259–268, Cham, 2021a. Springer International Publishing. doi: 10.1007/978-3-030-87202-1\_25.
- Megumi Nakao, Mitsuhiro Nakamura, and Tetsuya Matsuda. Image-to-graph convolutional network for 2D/3D deformable model registration of low-contrast organs. *IEEE Transactions on Medical Imaging*, 41(12):3747–3761, 2022. doi: 10.1109/TMI.2022.3194517.
- Megumil Nakao, Mitsuhiro Nakamura, Takashi Mizowaki, and Tetsuya Matsuda. Statistical deformation reconstruction using multi-organ shape features for pancreatic cancer localization. *Medical Image Analysis*, 67:101829, 2021b. doi: 10.1016/j.media.2020.101829.
- David Ouyang, Bryan He, Amirata Ghorbani, Neal Yuan, Joseph Ebinger, Curtis P. Langlotz, Paul A. Heidenreich, Robert A. Harrington, David H. Liang, Euan A. Ashley, and James Y. Zou. Video-based AI for beat-to-beat assessment of cardiac function. *Nature*, 580(7802):252–256, 2020. doi: 10.1038/s41586-020-2145-8.
- Caglar Ozturk, Daniel H. Pak, Luca Rosalia, Debkalpa Goswami, Mary E. Robakowski, Raymond McKay, Christopher T. Nguyen, James S. Duncan, and Ellen T. Roche. AI-powered multimodal modeling of personalized hemodynamics in aortic stenosis. *Advanced Science*, 12(5), 2025. doi: 10.1002/advs.202404755.
- Matthew J. Page, Joanne E McKenzie, Patrick M Bossuyt, Isabelle Boutron, Tammy C Hoffmann, Cynthia D Mulrow, Larissa Shamseer, Jennifer M Tetzlaff, Elie A Akl, Sue E Brennan, Roger Chou, Julie Glanville, Jeremy M Grimshaw, Asbjørn Hróbjartsson, Manoj M Lalu, Tianjing Li, Elizabeth W Loder, Evan Mayo-Wilson, Steve McDonald, Luke A McGuinness, Lesley A Stewart, James Thomas, Andrea C Tricco, Vivian A Welch, Penny Whiting, and David Moher. The PRISMA 2020 statement: An updated guideline for reporting systematic reviews. *The BMJ*, 372, 2021. doi: 10.1136/bmj.n71.
- Daniel H. Pak, Minliang Liu, Theodore Kim, Liang Liang, Andres Caballero, John Onofrey, Shawn S. Ahn, Yilin Xu, Raymond McKay, Wei Sun, Rudolph Gleason, and James S. Duncan. Patient-specific heart geometry modeling for solid biomechanics using deep learning. *IEEE Transactions on Medical Imaging*, 43(1):203–215, 2024. doi: 10.1109/TMI.2023.3294128.
- Aris T. Papageorgiou, Eric O. Ohuma, Douglas G. Altman, Tullia Todros, Leila Cheikh Ismail, Ann Lambert, Yasmin A. Jaffer, Enrico Bertino, Michael G. Gravett, Manorama Purwar, J Alison Noble, Ruyan Pang, Cesar G. Victora, Fernando C. Barros, Maria Carvalho, Laurent J. Salomon, Zulfiqar A. Bhutta, Stephen H. Kennedy, and Još Villar. International standards for fetal growth based on serial ultrasound measurements: The fetal growth longitudinal study of the INTERGROWTH-21st project. *The Lancet*, 384(9946):869–879, 2014. doi: 10.1016/S0140-6736(14)61490-2.
- Steffen E Petersen, Paul M Matthews, Jane M Francis, Matthew D Robson, Filip Zemrak, Redha Boubertakh, Alistair A Young, Sarah Hudson, Peter Weale, Steve Garratt, Rory Collins, Stefan Piechnik, and Stefan Neubauer. UK Biobank’s cardiovascular magnetic resonance protocol. *Journal of Cardiovascular Magnetic Resonance*, 18(1):227, 2016. doi: 10.1186/s12968-016-0227-4.
- Allan Pinkus. Approximation theory of the mlp model in neural networks. volume 8, pages 143–195. 1999. doi: 10.1017/S0962492900002919.
- Ashwin Raju, Shun Miao, Dakai Jin, Le Lu, Junzhou Huang, and Adam P. Harrison. Deep implicit statistical shape models for 3D medical image delineation. volume 36, pages 2135–2143, Jun. 2022. doi: 10.1609/aaai.v36i2.20110.
- Edoardo Remelli, Artem Lukoianov, Stephan Richter, Benoit Guillard, Timur Bagautdinov, Pierre Baque, and Pascal Fua. MeshSDF: Differentiable iso-surface extraction. *Advances in Neural Information Processing Systems*, 33:22468–22478, 2020.
- Anne-Marie Rickmann, Fabian Bongratz, Sebastian Pölsterl, Ignacio Sarasua, and Christian Wachinger. Joint reconstruction and parcellation of cortical surfaces. In Ahmed Abdulkadir, Deepti R. Bathula, Nicha C. Dvornek, Mohamad Habes, Seyed Mostafa Kia, Vinod Kumar, and Thomas Wolfers, editors, *Machine Learning in Clinical Neuroimaging*, pages 3–12, Cham, 2022. Springer Nature Switzerland. doi: 10.1007/978-3-031-17899-3\_1.
- Lukasz Romaszko, Agnieszka Borowska, Alan Lazarus, David Dalton, Colin Berry, Xiaoyu Luo, Dirk Husmeier, and Hao Gao. Neural network-based left ventricle geometry prediction from CMR images with application in biomechanics. *Artificial Intelligence in Medicine*, 119:102140, 2021. doi: 10.1016/j.artmed.2021.102140.
- Robin Rombach, Andreas Blattmann, Dominik Lorenz, Patrick Esser, and Björn Ommer. High-resolution image synthesis with latent diffusion models. In *Proceedings of the IEEE/CVF conference on computer vision and pattern recognition*, pages 10684–10695, 2022. doi: 10.1109/CVPR52688.2022.01042.

- Olaf Ronneberger, Philipp Fischer, and Thomas Brox. U-Net: Convolutional networks for biomedical image segmentation. In Nassir Navab, Joachim Hornegger, William M. Wells, and Alejandro F. Frangi, editors, *Medical Image Computing and Computer-Assisted Intervention – MICCAI 2015*, pages 234–241, Cham, 2015. Springer International Publishing. doi: 10.1007/978-3-319-24574-4\_28.
- Holger R Roth, Le Lu, Amal Farag, Hoo-Chang Shin, Jiamin Liu, Evrim B Turkbey, and Ronald M Summers. Data from pancreas-ct, 2016.
- D. Rueckert, L.I. Sonoda, C. Hayes, D.L.G. Hill, M.O. Leach, and D.J. Hawkes. Nonrigid registration using free-form deformations: Application to breast MR images. *IEEE Transactions on Medical Imaging*, 18(8): 712–721, 1999. doi: 10.1109/42.796284.
- Guillermo Ruiz, Eduard Ramon, Jaime García, Federico M. Sukno, and Miguel A. González Ballester. Weighted regularized statistical shape space projection for breast 3D model reconstruction. *Medical Image Analysis*, 47:164–179, 2018. doi: 10.1016/j.media.2018.04.007.
- Mehul P. Sampat, Zhou Wang, Shalini Gupta, Alan Conrad Bovik, and Mia K. Markey. Complex wavelet structural similarity: A new image similarity index. *IEEE Transactions on Image Processing*, 18(11):2385–2401, 2009. doi: 10.1109/TIP.2009.2025923.
- Rodrigo Santa Cruz, Léo Lebrat, Darren Fu, Pierrick Bourgeat, Jurgen Frapp, Clinton Fookes, and Olivier Salvado. CorticalFlow++: Boosting cortical surface reconstruction accuracy, regularity, and interoperability. In Linwei Wang, Qi Dou, P. Thomas Fletcher, Stefanie Speidel, and Shuo Li, editors, *Medical Image Computing and Computer Assisted Intervention – MICCAI 2022*, pages 496–505, Cham, 2022. Springer Nature Switzerland. doi: 10.1007/978-3-031-16443-9\_48.
- Ali Sarrami-Foroushani, Toni Lassila, Michael MacRaid, Joshua Asquith, Kit CB Roes, James V Byrne, and Alejandro F Frangi. In-silico trial of intracranial flow diverters replicates and expands insights from conventional clinical trials. *Nature communications*, 12(1):3861, 2021. doi: 10.1038/s41467-021-23998-w.
- Dinggang Shen, Guorong Wu, and Heung-Il Suk. Deep learning in medical image analysis. *Annual Review of Biomedical Engineering*, 19:221–248, 2017. doi: 10.1146/annurev-bioeng-071516-044442.
- Navid Shiee, Pierre-Louis Bazin, Jennifer L. Cuzzocreo, Chuyang Ye, Bhaskar Kishore, Aaron Carass, Peter A. Calabresi, Daniel S. Reich, Jerry L. Prince, and Dzung L. Pham. Reconstruction of the human cerebral cortex robust to white matter lesions: Method and validation. *Human Brain Mapping*, 35(7):3385–3401, 2014. doi: 10.1002/hbm.22409.
- Ryoya Shiode, Mototaka Kabashima, Yuta Hiasa, Kunihiro Oka, Tsuyoshi Murase, Yoshinobu Sato, and Yoshito Otake. 2D–3D reconstruction of distal forearm bone from actual x-ray images of the wrist using convolutional neural networks. *Scientific Reports*, 11(1):15249, 2021. doi: 10.1038/s41598-021-94634-2.
- Junji Shiraishi, Shigehiko Katsuragawa, Junpei Ikezoe, Tsuneo Matsumoto, Takeshi Kobayashi, Ken-Ichi Komatsu, Mitate Matsui, Hiroshi Fujita, Yoshie Koda, and Kunio Doi. Development of a digital image database for chest radiographs with and without a lung nodule: Receiver operating characteristic analysis of radiologists’ detection of pulmonary nodules. *American Journal of Roentgenology*, 174(1):71–74, 2000. doi: 10.2214/ajr.174.1.1740071.
- Greta Simionato, Konrad Hinkelmann, Revaz Chachanidze, Paola Bianchi, Elisa Fermo, Richard Van Wijk, Marc Leonetti, Christian Wagner, Lars Kaestner, and Stephan Quint. Red blood cell phenotyping from 3D confocal images using artificial neural networks. *PLoS Computational Biology*, 17(5), 2021. doi: 10.1371/journal.pcbi.1008934.
- Amber L. Simpson, Michela Antonelli, Spyridon Bakas, Michel Bilello, Keyvan Farahani, Bram van Ginneken, Annette Kopp-Schneider, Bennett A. Landman, Geert Litjens, Bjoern Menze, Olaf Ronneberger, Ronald M. Summers, Patrick Bilic, Patrick F. Christ, Richard K. G. Do, Marc Gollub, Jennifer Golia-Pernicka, Stephan H. Heckers, William R. Jarnagin, Maureen K. McHugo, Sandy Napel, Eugene Vorontsov, Lena Maier-Hein, and M. Jorge Cardoso. A large annotated medical image dataset for the development and evaluation of segmentation algorithms. *arXiv preprint arXiv:1902.09063*, 2019.
- Jiaming Song, Chenlin Meng, and Stefano Ermon. Denoising diffusion implicit models. *arXiv preprint arXiv:2010.02502*, 2020.
- Sheng Song, Yunqian Huang, Jiawen Li, Man Chen, and Rui Zheng. Development of implicit representation method for freehand 3D ultrasound image reconstruction of carotid vessel. *IEEE International Ultrasonics Symposium, IUS*, 2022. doi: 10.1109/IUS54386.2022.9958448.
- Avan Suinesiaputra, Pierre Ablin, Xenia Alba, Martino Alessandrini, Jack Allen, Wenjia Bai, Serkan Cimen, Peter Claes, Brett R. Cowan, Jan Dhooze, Nicolas Duchateau, Jan Ehrhardt, Alejandro F. Frangi, Ali

- Gooya, Vicente Grau, Karim Lekadir, Allen Lu, Anirban Mukhopadhyay, Ilkay Oksuz, Nripesh Parajuli, Xavier Pennec, Marco Pereanez, Catarina Pinto, Paolo Piras, Marc-Michel Rohe, Daniel Rueckert, Dennis Saring, Maxime Sermesant, Kaleem Siddiqi, Mahdi Tabassian, Luciano Teresi, Sotirios A. Tsaftaris, Matthias Wilms, Alistair A. Young, Xingyu Zhang, and Pau Medrano-Gracia. Statistical shape modeling of the left ventricle: Myocardial infarct classification challenge. *IEEE Journal of Biomedical and Health Informatics*, 22(2):503–515, 2018. doi: 10.1109/JBHI.2017.2652449.
- Shanlin Sun, Kun Han, Deying Kong, Hao Tang, Xiangyi Yan, and Xiaohui Xie. Topology-preserving shape reconstruction and registration via neural diffeomorphic flow. In *Proceedings of the IEEE Computer Society Conference on Computer Vision and Pattern Recognition*, volume 2022-June, pages 20813–20823, 2022. doi: 10.1109/CVPR52688.2022.02018.
- Mingxing Tan and Quoc Le. EfficientNet: Rethinking model scaling for convolutional neural networks. In Kamalika Chaudhuri and Ruslan Salakhutdinov, editors, *Proceedings of the 36th International Conference on Machine Learning*, volume 97 of *Proceedings of Machine Learning Research*, pages 6105–6114. PMLR, 09–15 Jun 2019.
- Jiaxiang Tang, Jiawei Ren, Hang Zhou, Ziwei Liu, and Gang Zeng. Dreamgaussian: generative Gaussian splatting for efficient 3D content creation. *12th International Conference on Learning Representations, ICLR 2024*, 2024.
- Songyuan Tang, Xu Yang, Peer Shajudeen, Candice Sears, Francesca Taraballi, Bradley Weiner, Ennio Tasciotti, Devon Dollahon, Hangu Park, and Raffaella Righetti. A CNN-based method to reconstruct 3-D spine surfaces from US images in vivo. *Medical Image Analysis*, 74: 102221, 2021. doi: 10.1016/j.media.2021.102221.
- Lyne P. Tchapmi, Vineet Kosaraju, Hamid Rezatofighi, Ian Reid, and Silvio Savarese. TopNet: Structural point cloud decoder. In *2019 IEEE/CVF Conference on Computer Vision and Pattern Recognition (CVPR)*, pages 383–392, 2019. doi: 10.1109/CVPR.2019.00047.
- Catalina Tobon-Gomez, Arjan J. Geers, Jochen Peters, Jürgen Weese, Karen Pinto, Rashed Karim, Mohammed Ammar, Abdelaziz Daoudi, Jan Margeta, Zulma Sandoval, Birgit Stender, Yefeng Zheng, Maria A. Zuluaga, Julian Betancur, Nicholas Ayache, Mohammed Amine Chikh, Jean-Louis Dillenseger, B. Michael Kelm, Saïd Mahmoudi, Sébastien Ourselin, Alexander Schlaefer, Tobias Schaeffter, Reza Razavi, and Kawal S. Rhode. Benchmark for algorithms segmenting the left atrium from 3D CT and MRI datasets. *IEEE Transactions on Medical Imaging*, 34(7):1460–1473, 2015. doi: 10.1109/TMI.2015.2398818.
- Fei Tong, Megumi Nakao, Shuqiong Wu, Mitsuhiro Nakamura, and Tetsuya Matsuda. X-ray2Shape: Reconstruction of 3D liver shape from a single 2D projection image. In *Proceedings of the Annual International Conference of the IEEE Engineering in Medicine and Biology Society (EMBC)*, volume 2020-July, pages 1608–1611, 2020. doi: 10.1109/EMBC44109.2020.9176655.
- Roger Trullo, Caroline Petitjean, Bernard Dubray, and Su Ruan. Multiorgan segmentation using distance-aware adversarial networks. *Journal of Medical Imaging*, 6(1): 014001, 2019. doi: 10.1117/1.JMI.6.1.014001.
- Mathias Unberath, Andreas Maier, Dominik Fleischmann, Joachim Hornegger, and Rebecca Fahrig. Open-source 4D statistical shape model of the heart for x-ray projection imaging. In *2015 IEEE 12th International Symposium on Biomedical Imaging (ISBI)*, pages 739–742, 2015. doi: 10.1109/ISBI.2015.7163978.
- Roshan Reddy Upendra, S.M. Kamrul Hasan, Richard Simon, Brian Jamison Wentz, Suzanne M. Shontz, Michael S. Sacks, and Cristian A. Linte. Motion extraction of the right ventricle from 4D cardiac cine MRI using a deep learning-based deformable registration framework. *Proceedings of the Annual International Conference of the IEEE Engineering in Medicine and Biology Society, EMBS*, pages 3795–3799, 2021a. doi: 10.1109/EMBC46164.2021.9630586.
- Roshan Reddy Upendra, Brian Jamison Wentz, Richard Simon, Suzanne M Shontz, and Cristian A Linte. CNN-based cardiac motion extraction to generate deformable geometric left ventricle myocardial models from cine MRI. In *International Conference on Functional Imaging and Modeling of the Heart*, pages 253–263. Springer, 2021b. doi: 10.1007/978-3-030-78710-3\_25.
- Aaron van den Oord, Oriol Vinyals, and Koray Kavukcuoglu. Neural discrete representation learning. *Advances in Neural Information Processing Systems*, 30, 2017.
- David C. Van Essen, Stephen M. Smith, Deanna M. Barch, Timothy E.J. Behrens, Essa Yacoub, and Kamil Ugurbil. The WU-Minn human connectome project: An overview. *NeuroImage*, 80:62–79, 2013. doi: 10.1016/j.neuroimage.2013.05.041.
- Rudolf LM van Herten, Ioannis Lagogiannis, Jelmer M Wolterink, Steffen Bruns, Eva R Meulendijks, Damini

- Dey, Joris R de Groot, José P Henriques, R Nils Planken, Simone Saitta, et al. World of forms: Deformable geometric templates for one-shot surface meshing in coronary ct angiography. *Medical Image Analysis*, page 103582, 2025.
- Yordanka Velikova, Mohammad Farid Azampour, Walter Simson, Marco Esposito, and Nassir Navab. Implicit neural representations for breathing-compensated volume reconstruction in robotic ultrasound. In *2024 IEEE International Conference on Robotics and Automation (ICRA)*, pages 1316–1322. IEEE, 2024. doi: 10.1109/ICRA57147.2024.10611443.
- Tom Vercauteren, Xavier Pennec, Aymeric Perchant, and Nicholas Ayache. Non-parametric diffeomorphic image registration with the demons algorithm. In Nicholas Ayache, Sébastien Ourselin, and Anthony Maeder, editors, *Medical Image Computing and Computer-Assisted Intervention – MICCAI 2007*, pages 319–326, Berlin, Heidelberg, 2007. Springer Berlin Heidelberg. doi: 10.1007/978-3-540-75759-7\_39.
- Dominik J. E. Waibel, Ernst Röell, Bastian Rieck, Raja Giryes, and Carsten Marr. A diffusion model predicts 3D shapes from 2D microscopy images. In *2023 IEEE 20th International Symposium on Biomedical Imaging (ISBI)*, pages 1–5, 2023. doi: 10.1109/ISBI53787.2023.10230752.
- Dominik J.E. Waibel, Niklas Kiermeyer, Scott Atwell, Ario Sadafi, Matthias Meier, and Carsten Marr. SHAPR predicts 3D cell shapes from 2D microscopic images. *iScience*, 25(11), 2022. doi: 10.1016/j.isci.2022.105298.
- Brian P. Walcott, Christopher J. Stapleton, Omar Choudhri, and Aman B. Patel. Flow diversion for the treatment of intracranial aneurysms. *JAMA Neurology*, 73(8):1002–1008, 2016. doi: 10.1001/jamaneurol.2016.0609.
- Jiepeng Wang, Yuan Liu, Peng Wang, Cheng Lin, Junhui Hou, Xin Li, Taku Komura, and Wenping Wang. Gaussurf: Geometry-guided 3D Gaussian splatting for surface reconstruction. *arXiv preprint arXiv:2411.19454*, 2024.
- Nanyang Wang, Yinda Zhang, Zhuwen Li, Yanwei Fu, Hang Yu, Wei Liu, Xiangyang Xue, and Yu-Gang Jiang. Pixel2Mesh: 3D mesh model generation via image guided deformation. *IEEE Transactions on Pattern Analysis and Machine Intelligence*, 43(10):3600–3613, 2020a. doi: 10.1109/TPAMI.2020.2984232.
- Peng Wang, Lingjie Liu, Yuan Liu, Christian Theobalt, Taku Komura, and Wenping Wang. NeuS: Learning neural implicit surfaces by volume rendering for multi-view reconstruction. *Advances in Neural Information Processing Systems*, 32:27171–27183, 2021.
- Yifan Wang, Zichun Zhong, and Jing Hua. DeepOrgan-Net: On-the-fly reconstruction and visualization of 3D / 4D lung models from single-view projections by deep deformation network. *IEEE Transactions on Visualization and Computer Graphics*, 26(1):960–970, 2020b. doi: 10.1109/TVCG.2019.2934369.
- Yiming Wang, Qin Han, Marc Habermann, Kostas Daniilidis, Christian Theobalt, and Lingjie Liu. NeuS2: Fast learning of neural implicit surfaces for multi-view reconstruction. In *2023 IEEE/CVF International Conference on Computer Vision (ICCV)*, pages 3272–3283, 2023a. doi: 10.1109/ICCV51070.2023.00305.
- Zijie Wang, Megumi Nakao, Mitsuhiro Nakamura, and Tetsuya Matsuda. Shape reconstruction for undetectable regions of abdominal organs based on a graph convolutional network. *Expert Systems with Applications*, 230: 120593, 2023b. doi: 10.1016/j.eswa.2023.120593.
- Udaranga Wickramasinghe, Edoardo Remelli, Graham Knott, and Pascal Fua. Voxel2Mesh: 3D mesh model generation from volumetric data. In Anne L. Martel, Purang Abolmaesumi, Danail Stoyanov, Diana Mateus, Maria A. Zuluaga, S. Kevin Zhou, Daniel Racoceanu, and Leo Joskowicz, editors, *Medical Image Computing and Computer Assisted Intervention – MICCAI 2020*, pages 299–308, Cham, 2020. Springer International Publishing. doi: 10.1007/978-3-030-59719-1\_30.
- Marek Wodzinski, Kamil Kwarciak, Mateusz Daniol, and Daria Hemmerling. Improving deep learning-based automatic cranial defect reconstruction by heavy data augmentation: From image registration to latent diffusion models. *Computers in Biology and Medicine*, 182:109129, 2024. doi: 10.1016/j.combiomed.2024.109129.
- Jelmer M. Wolterink, Tim Leiner, Bob D. de Vos, Jean-Louis Coatrieux, B. Michael Kelm, Satoshi Kondo, Rodrigo A. Salgado, Rahil Shahzad, Huazhong Shu, Miranda Snoeren, Richard A. P. Takx, Lucas J. van Vliet, Theo van Walsum, Tineke P. Willems, Guanyu Yang, Yefeng Zheng, Max A. Viergever, and Ivana Išgum. An evaluation of automatic coronary artery calcium scoring methods with cardiac CT using the orCaScore framework. *Medical Physics*, 43(5):2361–2373, 2016. doi: 10.1118/1.4945696.
- Yan Xia, Xiang Chen, Nishant Ravikumar, Christopher Kelly, Rahman Attar, Nay Aung, Stefan Neubauer, Stefan E. Petersen, and Alejandro F. Frangi. Automatic 3D+t four-chamber CMR quantification of the UK biobank: integrating imaging and non-imaging data priors at scale. *Medical Image Analysis*, 80:102498, 2022. doi: 10.1016/j.media.2022.102498.

- Yu-Tao Xiong, Wei Zeng, Lei Xu, Ji-Xiang Guo, Chang Liu, Jun-Tian Chen, Xin-Ya Du, and Wei Tang. Virtual reconstruction of midfacial bone defect based on generative adversarial network. *Head and Face Medicine*, 18 (1), 2022. doi: 10.1186/s13005-022-00325-2.
- Hao Xu, Ernesto Zacur, Jurgen E. Schneider, and Vicente Grau. Ventricle surface reconstruction from cardiac MR slices using deep learning. In Yves Coudière, Valéry Ozenne, Edward Vigmond, and Nejib Zemzemi, editors, *Functional Imaging and Modeling of the Heart*, pages 342–351, Cham, 2019. Springer International Publishing. doi: 10.1007/978-3-030-21949-9\_37.
- Hong Xu and Shireen Y. Elhabian. Image2SSM: Reimagining statistical shape models from images with radial basis functions. In Hayit Greenspan, Anant Madabhushi, Parvin Mousavi, Septimiu Salcudean, James Duncan, Tanveer Syeda-Mahmood, and Russell Taylor, editors, *Medical Image Computing and Computer Assisted Intervention – MICCAI 2023*, pages 508–517, Cham, 2023. Springer Nature Switzerland. doi: 10.1007/978-3-031-43907-0\_49.
- Ching-Juei Yang, Cheng-Li Lin, Chien-Kuo Wang, Jing-Yao Wang, Chih-Chia Chen, Fong-Chin Su, Yin-Ju Lee, Chun-Chung Lui, Lee-Ren Yeh, and Yu-Hua Dean Fang. Generative adversarial network (GAN) for automatic reconstruction of the 3D spine structure by using simulated bi-planar x-ray images. *Diagnostics*, 12(5), 2022. doi: 10.3390/diagnostics12051121.
- Yaoqing Yang, Chen Feng, Yiru Shen, and Dong Tian. FoldingNet: Point cloud auto-encoder via deep grid deformation. In *2018 IEEE/CVF Conference on Computer Vision and Pattern Recognition (CVPR)*, pages 206–215, 2018. doi: 10.1109/CVPR.2018.00029.
- Ziv Yaniv, Bradley C Lowekamp, Hans J Johnson, and Richard Beare. SimpleITK image-analysis notebooks: a collaborative environment for education and reproducible research. *Journal of Digital Imaging*, 31(3):290–303, 2018. doi: 10.1007/s10278-017-0037-8.
- Lior Yariv, Jiatao Gu, Yoni Kasten, and Yaron Lipman. Volume rendering of neural implicit surfaces. *Advances in Neural Information Processing Systems*, 6:4805–4815, 2021.
- Lior Yariv, Peter Hedman, Christian Reiser, Dor Verbin, Pratul P. Srinivasan, Richard Szeliski, Jonathan T. Barron, and Ben Mildenhall. BakedSDF: Meshing neural SDFs for real-time view synthesis. In *ACM SIGGRAPH 2023 Conference Proceedings*, New York, NY, USA, 2023. Association for Computing Machinery. ISBN 9798400701597. doi: 10.1145/3588432.3591536.
- Meng Ye, Dong Yang, Mikael Kanski, Leon Axel, and Dimitris Metaxas. Neural deformable models for 3D bi-ventricular heart shape reconstruction and modeling from 2D sparse cardiac magnetic resonance imaging. *Proceedings of the IEEE International Conference on Computer Vision*, pages 14201–14210, 2023. doi: 10.1109/ICCV51070.2023.01310.
- Pak-Hei Yeung, Linde S. Hesse, Moska Aliasi, Monique C. Haak, Weidi Xie, and Ana I.L. Namburete. Sensorless volumetric reconstruction of fetal brain freehand ultrasound scans with deep implicit representation. *Medical Image Analysis*, 94:103147, 2024. doi: 10.1016/j.media.2024.103147.
- Lequan Yu, Xianzhi Li, Chi-Wing Fu, Daniel Cohen-Or, and Pheng-Ann Heng. PU-Net: Point cloud upsampling network. In *2018 IEEE/CVF Conference on Computer Vision and Pattern Recognition*, pages 2790–2799, 2018. doi: 10.1109/CVPR.2018.00295.
- Zehao Yu, Torsten Sattler, and Andreas Geiger. Gaussian opacity fields: Efficient adaptive surface reconstruction in unbounded scenes. *ACM Transactions on Graphics (TOG)*, 43(6), 2024. doi: 10.1145/3687937.
- Xiaohan Yuan, Cong Liu, and Yangang Wang. 4D myocardium reconstruction with decoupled motion and shape model. *Proceedings of the IEEE International Conference on Computer Vision*, pages 21195–21205, 2023. doi: 10.1109/ICCV51070.2023.01943.
- Debbie Zhao, Edward Ferdian, Gonzalo D. Maso Talou, Gina M. Quill, Kathleen Gilbert, Vicky Y. Wang, Thiranjia P. Babarenda Gamage, João Pedrosa, Jan D’hooge, Timothy M. Sutton, Boris S. Lowe, Malcolm E. Legget, Peter N. Ruygrok, Robert N. Doughty, Oscar Camara, Alistair A. Young, and Martyn P. Nash. MITEA: A dataset for machine learning segmentation of the left ventricle in 3D echocardiography using subject-specific labels from cardiac magnetic resonance imaging. *Frontiers in Cardiovascular Medicine*, 9, 2023a. doi: 10.3389/fcvm.2022.1016703.
- Fenqiang Zhao, Zhengwang Wu, Li Wang, Weili Lin, John H. Gilmore, Shunren Xia, Dinggang Shen, and Gang Li. Spherical deformable U-Net: Application to cortical surface parcellation and development prediction. *IEEE Transactions on Medical Imaging*, 40(4):1217–1228, 2021. doi: 10.1109/TMI.2021.3050072.
- Jingliang Zhao, Jie Zhao, Shumao Pang, and Qianjin Feng. Segmentation of the true lumen of aorta dissection via morphology-constrained stepwise deep mesh regression. *IEEE Transactions on Medical Imaging*, 41(7):1826–1836, 2022. doi: 10.1109/TMI.2022.3150005.



Junjie Zhao, Siyuan Liu, Sahar Ahmad, and Pew-Thian Yap. MeshDeform: Surface reconstruction of subcortical structures via human brain MRI. In Alejandro Frangi, Marleen de Bruijne, Demian Wassermann, and Nassir Navab, editors, *Information Processing in Medical Imaging*, pages 536–547, Cham, 2023b. Springer Nature Switzerland. doi: 10.1007/978-3-031-34048-2\_41.

Hao Zheng, Hongming Li, and Yong Fan. SurfNN: Joint reconstruction of multiple cortical surfaces from magnetic resonance images. In *Proceedings - International Symposium on Biomedical Imaging*, 2023. doi: 10.1109/ISBI53787.2023.10230488.

Xiao-Yun Zhou, Zhao-Yang Wang, Peichao Li, Jian-Qing Zheng, and Guang-Zhong Yang. One-stage shape instantiation from a single 2D image to 3D point cloud. In Dinggang Shen, Tianming Liu, Terry M. Peters, Lawrence H. Staib, Caroline Essert, Sean Zhou, Pew-Thian Yap, and Ali Khan, editors, *Medical Image Computing and Computer Assisted Intervention – MICCAI 2019*, pages 30–38, Cham, 2019. Springer International Publishing. doi: 10.1007/978-3-030-32251-9\_4.

Xiahai Zhuang and Juan Shen. Multi-scale patch and multi-modality atlases for whole heart segmentation of MRI. *Medical Image Analysis*, 31:77–87, 2016. doi: 10.1016/j.media.2016.02.006.